ISTANBUL TECHNICAL UNIVERSITY ★ EURASIA INSTITUTE OF EARTH SCIENCES

MONITORING OF SURFACE DEFORMATION IN NORTHWEST TURKEY FROM HIGH RESOLUTION INSAR: FOCUS ON TECTONIC ASEISMIC SLIP AND SUBSIDENCE

Ph.D. THESIS

Gökhan ASLAN

Solid Earth Sciences

Geodynamics

APRIL 2019

ISTANBUL TECHNICAL UNIVERSITY ★ EURASIA INSTITUTE OF EARTH SCIENCES

**MONITORING OF SURFACE DEFORMATION IN NORTHWEST TURKEY
FROM HIGH RESOLUTION INSAR: FOCUS ON TECTONIC ASEISMIC SLIP
AND SUBSIDENCE**

Ph.D. THESIS

Gökhan ASLAN
(602142001)

Solid Earth Sciences

Geodynamics

Thesis Advisor: Prof. Dr. Ziyadin Çakir

APRIL 2019

İSTANBUL TEKNİK ÜNİVERSİTESİ ★ AVRASYA YER BiLiMLERİ ENSTİTÜSÜ

TÜRKIYE'NİN KUZEY-BATI BÖLGESİNDEKİ YÜZEY DEFORMASYONLARININ YÜKSEK ÇÖZÜNÜRLÜKLÜ İNSAR VERİLERİ YARDIMI İLE GÖZLENMESİ: ASİSMİK SLİP VE ÇÖKÜNTÜ OLGULARI

DOKTORA TEZİ

Gökhan ASLAN
(602142001)

Katı Yer Bilimleri Anabilim Dalı

Jeodinamik Programı

Tez Danışmanı: Prof. Dr. Ziyadin Çakir

NİSAN 2019

Gökhan ASLAN, a Ph.D. student of ITU Eurasia Institute of Earth Sciences student ID 602142001, successfully defended the dissertation entitled "MONITORING OF SURFACE DEFORMATION IN NORTHWEST TURKEY FROM HIGH RESOLUTION INSAR: FOCUS ON TECTONIC ASEISMIC SLIP AND SUBSIDENCE", which he prepared after fulfilling the requirements specified in the associated legislations, before the jury whose signatures are below.

Thesis Advisor :   **Prof. Dr. Ziyadin CAKIR**   ....
Istanbul Technical University

Jury Members :   **Dr. Cécile LASSERRE**   ....
CNRS, Université Lyon1

    Prof. Dr. Michel BOUCHON   ....
CNRS, Université Grenoble Alpes

    Prof. Dr. Semih ERGINTAV   ....
Bogazici University

    Assoc. Prof. Dr. Sinan OZEREN   ....
Istanbul Technical University

Date of Submission : 18 March 2019
Date of Defense : 30 April 2019

To my parents,

FOREWORD

First and foremost, I deeply thank my parents, Ibrahim and Tülay for giving me liberty to choose what I desired. I am also grateful to my siblings Eyüphan and Nazire for their timely encouragement and emotional support along the way. My PhD journey would not have been possible without the support of my family.

I would like to express my sincere gratitude to my thesis and research advisors Ziyadin Çakir, Cécile Lasserre, François Renard and Semih Ergintav for their great support that helped me become an independent researcher. They always motivated me when I had struggling times and their ideas, attention to details and teaching helped me to improve my research immensely and to learn lots of academic concepts in my PhD journey. At many stages in the course of this research, the critical discussions I had with them led me to develop a critical sense of thinking and encouraged me for thinking big.

March 2019   Gökhan ASLAN

TABLE OF CONTENTS

ABBREVIATIONS

AIC	**:** Akaike Information Criterian
ERS	**:** European Remote-Sensing Satellite
ESA	**:** European Space Agency
DEM	**:** Digital Elevation Model
DORIS	**:** Delft Object-oriented Radar Interferometric Software
GMTSAR	**:** Generic Mapping Tools Synthetic Aperture Radar
GMT	**:** Generic Mapping Tools
GPS	**:** Global Positioning System
GNSS	**:** Global Navigation Satellite System
GSNL	**:** Geohazard Supersites and Natural Laboratories
InSAR	**:** Interferometric Synthetic Aperture Radar
ITMP	**:** Istanbul Transport Master Plan
JGR	**:** Journal of Geophysical Research
LIDAR	**:** Light Detection And Ranging
LOS	**:** Line of Sight
MIT	**:** Massachusetts Institute of Technology
MCMC	**:** Markov chain Monte Carlo
MTA	**:** Turkey General Directorate of Mineral Research and Exploitation
NAF	**:** North Anatolian Fault
PS	**:** Persistent Scatterer
PS-InSAR	**:** Persistent Scatterer Interferometric Synthetic Aperture Radar
PSI	**:** Persistent Scatterer Interferometry
SAR	**:** Synthetic Aperture Radar
TRAIN	**:** Toolbox for Reducing Atmospheric InSAR Noise
TSX	**:** TerraSAR-X
TUIK	**:** Turkish Statistical Institute
SBAS	**:** Small Baseline
StaMPS	**:** Stanford Method for Persistent Scatterers
SLC	**:** Single Look Complex
SRTM	**:** Shuttle Radar Topographic Mission
VHR	**:** Very High Resolution

SYMBOLS

a	: Constant velocity of adjustment
b	: Thickness of the aquifer
d_{asc}	: Satellite LOS velocity in ascending mode
d_{dsc}	: Satellite LOS velocity in descending mode
d_{ver}	: Vertical displacement
d_{hor}	: Horizontal displacement
d_{σ_e}	: Change in the effective pressure in the aquifer
D_{Amp}	: Amplitude Dispersion Index
D_1	: The depth of seismogenic zone (locking depth)
D_2	: Shallow creep depth between the surface to depth D_2
g	: Gravitational constant
H	: Elastic locking depth
m_{Amp}	: Mean of amplitude
n	: Noise
ν	: Interseismic velocity at shallow depth (seismogenic zone)
ν_0	: Deep steady slip rate (tectonic loading rate)
V_t	: Total volume of aquifer
x	: Distance from the fault trace
α	: Aquifer compressibility index
α_{asc}	: Heading angle in ascending mode
α_{dsc}	: Heading angle in descending mode
σ_{Amp}	: Standard deviation of amplitude
$\dot{\varepsilon}$	: Shear strain at the free surface
θ_{asc}	: Local incidence angle in ascending mode
θ_{dsc}	: Local incidence angle in descending mode
Δ_φ	: Phase difference
$\Delta_{\varphi_{displ}}$	: Surface displacement phase component
$\Delta_{\varphi_{atm}}$	: Atmospheric delay phase component
$\Delta_{\varphi_{topo}}$	: Topographic phase component
$\Delta_{\varphi_{orb}}$	: Orbital phase contribution
ΔAIC	: AIC difference between two models

LIST OF TABLES

LIST OF FIGURES

MONITORING OF SURFACE DEFORMATION IN NORTHWEST TURKEY FROM HIGH-RESOLUTION INSAR: FOCUS ON TECTONIC ASEISMIC SLIP AND SUBSIDENCE

SUMMARY

Geohazards, such as earthquakes, land subsidence and uplift, ground settlement, landslides and volcanoes cause static and/or dynamic surface deformation and pose major threat to human life and structures. Especially in earthquake-prone areas, understanding the spatial and temporal evolution of surface displacement and the underlying mechanisms responsible for these displacements is of great importance for geohazard mitigation.

The Anatolian plate is bounded by the right-lateral North Anatolian Fault (NAF) and the left-lateral East-Anatolian Fault to the north and east-southeast of Turkey, respectively. It is moving westward due to the convergence of the Arabian and Eurasian plates and the slab subduction at the Hellenic Trench. The 1600-km-long NAF is a major continental strike-slip fault, known as one of the most prominent active faults in the eastern Mediterranean region, with an average slip rate of 24±2 mm/yr. This right-lateral fault ruptured between 1939 and 1999 in a sequence of eight M>7 earthquakes, with a westward migration that started near Erzincan in the east and reached the western shore of Marmara Sea in the west. This migration has been explained by the Coulomb stress transfer during and between successive earthquakes along fault strike. Between the western end of this sequence, and the eastern end of the 1912 earthquake to the east of the Marmara sea, a ~70 km-long section of the NAF defines a major seismic gap very close to the megacity of Istanbul. Assessment of seismic hazard in the Marmara sea region suggests that a large and destructive earthquake (M>7) may occur with a probability of 35-70% in the next 30 years on this fault section, 20 km south of Istanbul. Refined assessment of seismic hazard, from precise measurements of tectonic ground deformations in particular, is therefore profoundly important for prevention of any widespread damage and destruction in the region. This region is also affected by an important population growth and industrial and land exploitation development, implying other types of hazards.

The aim of this thesis is therefore centered on the detection and monitoring of surface deformation in northwest Turkey induced by a variety of natural (such as tectonic activity, slow moving-landslides, etc.) and anthropogenic (ground water extraction, construction activities, etc.) hazards and on the analysis of the related deformation mechanisms and their environmental consequences. In this work, I computed Interferometric Synthetic Aperture Radar (InSAR) time series to examine ground deformation evolution for three different case studies associated to different geophysical phenomena and underlying processes. The focus of this thesis is two-fold : (1) to reveal and monitor the spatio-temporal characteristics of aseismic slip along the August 17, 1999 M_w 7.4 Izmit earthquake rupture, and discuss its potential

relationship with lithology and geology (2) to investigate ground subsidence in urban or human-exploited areas induced by various factors, and discuss the relative roles of tectonics, lithology and anthropogenic activities in such ground motion.

In the first case-study, I combined InSAR measurements, based on X-band TerraSAR-X and C-band Sentinel-1 A-B radar images acquired over the period 2011-2017, with near field GPS measurements, performed every 6 months from 2014 to 2016, as well as creep meter measurements to examine the surface velocity field around the NAF after the 1999 Izmit earthquake. In this study, the Stanford Method for Persistent Scatterers InSAR package (StaMPS) was employed to process series of Sentinel 1 A-B (acquired along ascending and descending orbits) and TerraSAR-X (ascending orbits) radar images. The InSAR horizontal mean velocity fields reveal that the creep rate on the central segment of the 1999 Izmit fault rupture continues to decay, more than 19 years after the earthquake, in overall agreement with models of postseismic afterslip rate decaying logarithmically with time. Along the fault section that experienced a supershear velocity rupture during the Izmit earthquake, creep continues with a rate up to ~ 8 mm/yr. A significant transient event with accelerating creep is detected in December 2016 on the Sentinel-1 time series, consistent with creepmeter measurements, near the maximum creep rate location. It is associated with a total surface slip of 10 mm released in one month only. Complementary analyses of the vertical velocity fields show a persistent subsidence on the hanging wall block of the Golcuk normal fault that also ruptured during the Izmit earthquake. Our results demonstrate that afterslip processes along the North Anatolian Fault east-southeast of Istanbul are more complex than previously proposed as they vary spatio-temporally along the fault.

The second case study deals with the identification and measurement of secular ground deformation in Istanbul from a long-term InSAR time-series spanning almost 25 years of satellite radar observations (1992-2017). This InSAR time series was computed from radar images of multiple satellites (ERS-1, ERS-2, Envisat, Sentinel-1 A, B) in order to investigate the spatial extent and rate of ground subsidence in the megacity of Istanbul. By combining the various multi-track InSAR datasets (291 images in total) and analysing persistent scatterers (Ps-InSAR), we present mean line of sight velocity maps fields and project them into ground surface velocity maps in selected areas of Istanbul. Various sites along the terrestrial and coastal regions of Istanbul are found to be undergoing vertical ground subsidence at varying rates from ~5 mm/yr to ~15 mm/yr. The results reveal that the most distinctive subsidence patterns are associated with both anthropogenic factors and relatively weak lithologies along the Haramirede valley in particular, where the observed subsidence is up to ~10 mm/yr. We show that subsidence has been occurring along the Ayamama river at a rate of up to ~10 mm/yr since 1992, and has also been slowing down over time following the restoration of the river and stream system. We also identify subsidence at a rate of ~8 mm/yr along the coastal region of Istanbul which we associate with land reclamation, as well as a very localised subsidence at a rate of ~15 mm/yr starting in 2016 around one of the highest skyscrapers of Istanbul, that was built in 2010.

In the third case study, InSAR time-series analysis is calculated for quantifying the subsidence of the Bursa Plain (southern Marmara region of Turkey), which has been interpreted as resulting from tectonic motions in the region. In this study, the StaMPS is employed to process series of Sentinel 1 A-B radar images acquired between 2014 and 2017 along both ascending and descending orbits. The vertical velocity field

obtained after decomposition of line-of-sight velocity fields on the two tracks reveals that the Bursa plain is subsiding at rates up to 25 mm/yr. The most prominent subsidence signal in the basin forms an east-west elongated ellipse of deformation in the east, and is bounded by a Quaternary alluvial plain undergoing average vertical subsidence at ~10 mm/yr. Another localized subsidence signal is located 5 km north of the city, following the Bursa alluvial fan, and is subsiding at velocities up to 25 mm/yr. The comparison between temporal variations of the subsiding surface displacements and variations of the water pressure head in the aquifer allows estimation of the compressibility of the aquifer, α. It falls in the range of $0.5 \times 10^{-6} - 2 \times 10^{-6}$ Pa^{-1}, which corresponds to typical values for clay and sand sediments. We find a clear correlation between subsidence patterns and the lithology, suggesting a strong lithological control over the observed subsidence. In addition, the maximum rate of ground subsidence occurs where agricultural activity relies on groundwater exploitation. The InSAR time series within the observation period is well correlated with changes in the depth of the ground water. These observations indicate that the recent acceleration of subsidence is mainly due to anthropogenic activities rather than tectonic motion.

Finally, this dissertation emphasizes the potentialities of the methodology of InSAR time-series analysis to efficiently map millimetre-scale deformation for different geophysical phenomena along the selected region in northwest Turkey. To better understand the mechanism of crustal deformation and differentiate slow surface deformations driven by human and regular tectonic activities, further work, complementary to InSAR, would be required to enable the monitoring and forecasting of region-wide geohazards.

TÜRKİYE'NİN KUZEY-BATI BÖLGESİNDEKİ YÜZEY DEFORMASYONLARININ YÜKSEK ÇÖZÜNÜRLÜKLÜ İNSAR VERİLERİ YARDIMI İLE GÖZLENMESİ: ASİSMİK SLİP VE ÇÖKÜNTÜ OLGULARI

ÖZET

Deprem, toprak kayması, zemin kabarması, volkanlar ve otumalar, yer yüzeyinde statik ve/veya dinamik yüzey hareketlerine sebep olmakta ve bu insan hayatı ve yapılar üzerinde ciddi tehdit oluşturmaktadır. Özellikle, deprem tehlikesinin yüksek olduğu bölgelerde, bu gibi yüzey deformasyonlarının altında yatan jeofiziksel olguların konumsal ve zamansal ölçekte gelişiminin anlaşılması, afet zararlarının azaltılması açısından büyük önem taşımaktadır.

Anadolu Plakası, kuzeyden sağ yanal atımlı Kuzey Anadolu Fayı (KAF) ve güney-doğuda sol yanal atımlı Doğu Anadolu Fayı (DAF) ile çevrelenmiş olup, Arap levhasının Avrasya levhasına doğru yaklaşması ve de Helen yayının çekilmesi sonucu batıya doğru hareket etmektedir. 1600 km uzunluğundaki Kuzey Anadolu Fayı, yıllık 24±2 mm'lik bir kayma hızına sahip kıtasal yanal atımlı bir fay olup, doğu Akdeniz bölgesindeki en aktif faylardan biri olarak bilinmektedir. KAF, 1939 ve 1999 yılları arasında büyüklüğü 7 den büyük olan batı-yönlü 8 adet deprem dizisi ile kırılmaya uğramıştır. Bu deprem dizisi, 1939 yılında doğuda Erzincan Depremi ile başlamış ve batıda 1999 yılında İzmit Depremi ile Marmara denizinin bati ucuna ulaşmıştır. NAF boyunca gözlenen ve art arda meydana gelen batı yönlü bu deprem göçü, Coulomb gerilme transferi ile açıklanmaktadır. Mevcut durumda, bu deprem dizilerinin batı ucu Marmara Denizi'nin doğusuna dayanmaktadır ve Marmara denizi içinden geçen kırılmayı bekleyen segment bölgede son derece ciddi bir sismik boşluk olarak tanımlanmakta ve İstanbul metropol şehrine ve civardaki diğer yerleşim yerlerine yakınlığı dolayısı ile büyük bir risk oluturmaktadır. Marmara Bölgesi'ndeki sismik risk analizleri, önümüzdeki 30 yıl içerisinde bölgede büyük ve yıkıcı (M>7) deprem olma olasılığını %35-70 arasında olarak tespit etmiştir. Bu yüzden detaylı sismik tehlike analizleri ve bölgedeki yüzey deformasyonlarının yüksek hassasiyet ve sıklıkta ölçülmesi, bölgede meydana gelmesi beklenen deprem kaynaklı büyük bir afetin önlenmesi ve azaltılmasında hayati bir öneme sahiptir.

Bu etkenler göz önünde bulundurulduğunda, yukarıda değinilen sebeplerle bu tez çalışması, Marmara Bölgesi'ndeki antropojenik (insan kökenli – yer altı suyu kullanımı, yeralti ve yer üstü yapıları vs.) ve doğal etkenlerden (tektonik hareketler vs.) kaynaklanan, küçük ölçekli yer hareketlerinin tespiti ve gözlenmesinin yanında bu deformasyon mekanizmasının analizine odaklanmaktadır. Bu tez çalışmasında Sentetik Açıklıklı Radar İnterferometresi (InSAR) zaman serileri tekniği kullanılarak farklı jeofiziksel olgulardan kaynaklanan yüzey deformasyonlarının zamansal ve konumsal gelişimi ve bu yüzey deformasyonlarının altında yatan mekanizma analiz edilmiştir. Bu tez çalışmasının iki temel odağı vardır: (1) 17 Ağustos, 1999 İzmit Depremi kırığı boyunca asismik kaymanın (krip) zamansal ve konumsal dağılımı ve litolojik ve jeolojik etkenlerin bu dağılım üzerindeki etkisinin analiz edilmesi; (2)

kentsel bölgelerde çeşitli faktörlerden kaynaklı yüzey oturmalarının tektonik kaynaklı olup olmadığının incelenmesi.

Bu tezin ilk vaka çalışmasında, 1999 İzmit Depremi'den 19 yıl sonra fay çevresi yüzey deformasyonlarının tespit edilmesi amacıyla, 2011-2017 yılları arasında (X-band) TerraSAR-X ve (C-band) Sentinel 1 A-B radar görüntülerinden StaMPS yöntemi ile elde edilen InSAR zaman serileri ve 2014-2016 yılları arasında her altı ayda bir fay civarında tatbik edilen GPS kampanya ölçümleri, krip metre verileri ile entegre edilmiştir. Elde edilen hız alanları incelendiğinde, 1999 İzmit kırığının merkez segmentinde gözlenen asismik kaymanın, depremden 19 yıl sonra da postsismik afterslip modeli ile uyum içerisinde logaritmik olarak azalarak devam devam ettiği görülmüştür. 1999 depreminde *"Supershear"* hızı ile kırılan segment boyunca gözlenen krip hızı ~ 8 mm/yıl civarındadır. Sentinel-1 verilerinden elde edilen zaman serileri analiz edildiğinde, 2016 yılı Aralık ayında, krip hızında ani bir artış tespit edilmiştir. Bu artış yüzeyde ~ 10 mm'lik bir kaymanın 1 aylık bir süre içerisinde gerçekleştiğini göstermiştir. Elde edilen düşey yönlü hız alanlarında yapılan analizlerde, deprem sırasında kırılan Gölcük normal fayının tavan bloğunda belirgin bir oturma sinyali gözlenmiştir. Bu sonuçlar göstermektedir ki, İstanbul'un güney batı bölgesinde NAF boyunca gözlenen after slip kayma süreci düşünüldüğünden daha bir komplex yapıda olup, fay boyunca zamansal ve konumsal ölçekte farklılık göstermektedir.

İkinci vaka çalışmasında, uzun dönem (1992-2017) InSAR zaman serileri kullanılarak İstanbul şehri ve çevresindeki yerel deformasyon ve yer değiştirme miktarlarının tespiti ve izlenmesi hedeflenmiştir. Bu çalışmada, farklı radar uydu sensörlerinden (ERS-1, ERS-2, Envisat, Sentinel 1 A-B) elde edilen yaklaşık 25 yıllık zaman serisi kullanılarak bölgedeki oturma sinyallerinin hızı ve bunların zamansal ve konumsal kapsamı analiz edilmiştir. Her bir veri setinden elde edilen hız alanları karşılaştırılarak, detaylı analiz edilmek üzere belirli bölgeler seçilmiştir. Karasal ve kıyısal alan boyunca tespit edilen bu bölgelerde oturma hızları 5 ± 1.2 mm/yıl ile 15 ± 2.1 mm/yıl arasında değişlik göstermektedir. Seçilen bu bölgeler arasında konumsal kapsam ve hız olarak en belirgin oturma sinyali 10 ± 2.0 mm/yıl hızı hem antropojenik hem de litolojik faktörlerin rol oynadığı Haramidere vadisi boyunca gözlenmiştir. Ayamama vadisi boyunca 1992 yılından bu yana gözlenen oturma sinyali 10 ± 1.8 mm/yıl değerinde olup, dere yatağın rehabilitasyonu sonucu oturma miktarında belirgin azalma tespit edilmiştir. İstanbul'un kıyı alanlarında dolgu yapılan bölgelerindeki oturma miktarları ise yıllık 8 ± 1.2 mm olduğu gözlenmiştir. Ayrıca, 2010 yılında inşa edilen İstanbul'un en yüksek binası çevresinde 15 ± 2.3 mm/yıl hızında son derece lokal bir oturma gösterdiği görülmüştür.

Son olarak bölüm 6'da ele aldığımız vaka çalışmasında, Marmara'nın güneyinde yer alan ve bölgedeki tektonik aktiviteden kaynaklandığı öne sürülen, Bursa Havzası'ndaki yer hareketleri InSAR zaman serisi yöntemi ile analiz edilmiştir. Bu çalışmada da, diğer iki çalışma gibi 2014-2017 zaman aralığını kapsayan kuzey yönlü (ascending) ve güney yönlü (descending) Sentinel 1 A-B radar verileri StaMPS yöntemi ile analiz edilerek havzadaki deformasyonun zaman serisi elde edilmiştir. Her içi çerçevenin dekompozisyonu sonucu elde edilen düşey yönlü hız alanı, Bursa havzasının yılda 25 mm hızla çöktüğünü göstermektedir. Kuatarner alüvyal ova ile sınırlanan Bursa havzasındaki en belirgin oturma sinyali, ortalama 10 mm/yıl hızında

olup, kuzey-güney yönlü elips formuna sahiptir. Bursa şehir merkezinin 5km kuzeyinde kalan bir diğer oturma sinyali ise 25 mm/yıl hızına sahip olup ve oldukça bir diğer lokal bir alanı kapsamaktadır. Yüzey deformasyon verilerinin zaman değişimi ile bölgedeki yeraltı su seviyesindeki zamansal değişim karşılaştırılarak, akiferin sıkışabilirlik (α) özelliğini kestirmek mümkündür. Bursa havzası için hesaplanan bu değer $0.5 \times 10^{-6} - 2 \times 10^{-6}$ Pa^{-1} arasında olup, kil ve kum boyutunda sediman malzemesinden oluşan kayaçlar için beklenen sıkışabilirlik değerleri arasındadır. Bursa havzası boyunca gözlenen oturma sinyalinin konumsal bazda litoloji ile uyum içerisinde olduğu görülmüştür. Bu durum, oturmanın litolojik kontrollü olduğunu göstermektedir. Bunun yanında, oturma hızının maksimum olduğu bölgenin, yoğun yer altı su kullanımına dayanan tarımsal aktivite ile örtüşmesi, havzadaki su seviyesindeki değişimin, yüzeydeki deformasyon oluşumuna katkı sağladığını göstermektedir. Kaldı ki, InSAR zaman serisi ile su seviyesindeki değişimin benzer eğilim göstermesi bunu açıkça ortaya koymaktadır. Sonuç olarak bu çalışma göstermektedir ki, Bursa havzasında gözlenen çökme tektonik kaynaklı olmayıp, daha çok antropojenik kaynaklı bir vakadır.

Bu tez çalışması, Türkiye'nin kuzey-batı bölgesinde belirli bölgeler içerisinde , farklı jeofiziksel olgulardan kaynaklanan milimetre mertebesindeki yüzey deformasyonu çalışmalarında InSAR zaman serisi katkısını vurgulamaktadır. Bölgesel jeotehlike analizlerinin hazırlanmasında, kabuk deformasyonu mekanizmasının daha iyi anlaşılması ve küçük ölçekli yüzey deformasyonlarının tektonik kaynaklı olup olmadığının belirlenmesi için InSAR çalışmalarına ek olarak daha fazla yeni araç ve teknik kullanılması gerekmektedir.

MESURE ET SUIVI SPATIO-TEMPOREL DES DEPLACEMENTS DE SURFACE DANS LE NORD-OUEST DE LA TURQUIE, PAR INTERFEROMETRIE RADAR À HAUTE RÉSOLUTION: GLISSEMENT ASISMIQUE ET SUBSIDENCE

RÉSUMÉ

Les risques naturels, incluant tremblements de terre, déformations volcaniques, glissements de terrain, subsidence et soulèvement du sol, peuvent entraîner des déformations statiques et/ou dynamiques de la surface de la Terre et constituent une menace majeure pour la vie humaine et les structures. En particulier dans les zones sujettes aux tremblements de terre, Le suivi de l'évolution spatiale et temporelle des déplacements du sol et la compréhension des mécanismes sous-jacents, en particulier dans les zones soumises aux séismes, sont d'une grande importance dans l'estimation des aléas géologiques et la réduction des risques.

En Turquie, la plaque Anatolie est délimitée respectivement par la faille décrochante dextre nord-anatolienne (NAF), au nord, et par la faille décrochante sénestre est-anatolienne, à l'est-sud-est. Par rapport à la plaque Eurasie, elle se déplace vers l'ouest en raison de la convergence des plaques Arabie et Eurasie, et de la subduction le long de la fosse hellénique. La NAF, longue de 1600 km, est l'une des principales failles actives de la région est de la Méditerranée, avec une vitesse de glissement moyenne de 24 ± 2 mm / an. Cette faille a rompu entre 1939 et 1999 en une séquence de huit séismes de M> 7, avec une migration vers l'ouest qui a débuté près d'Erzincan à l'est et a atteint la rive est de la mer de Marmara à l'ouest. Cette migration a été expliquée par des transferts de contrainte de Coulomb pendant et entre les tremblements de terre successifs le long de la faille. Entre l'extrémité ouest de cette séquence et l'extrémité est du tremblement de terre de 1912 à l'ouest de la mer de Marmara, une section d'environ 70 km de la NAF définit une lacune sismique à proximité de la mégapole d'Istanbul. L'évaluation de l'alea sismique dans cette région de la mer de Marmara suggère que sur cette lacune, un séisme important et destructeur (M> 7) pourrait survenir, avec une probabilité de 35 à 70% au cours des 30 prochaines années, à seulement 20 km au sud d'Istanbul. Une évaluation plus fine de l'alea, en particulier à partir de mesures précises des déformations du sol d'origine tectonique, revêt donc une importance capitale pour la prévention de tout dommage et destruction dans la région. Cette région est également touchée par une croissance démographique importante et par le développement de l'exploitation industrielle et foncière, impliquant d'autres types de risques.
Le but de cette thèse est donc centré sur la détection et la surveillance de la déformation de surface dans le nord-ouest de la Turquie, induite par une variété de phénomènes naturels (telles que l'activité tectonique, les glissements de terrain lents, etc.) et anthropiques (extraction des eaux souterraines, activités de construction, etc.), et sur l'analyse des mécanismes de déformation associés et de leurs conséquences pour l'environnement. Ce travail est basé sur le calcul de séries temporelles de

déplacement du sol par interférométrie radar à synthèse d'ouverture (InSAR) afin d'analyser l'évolution des déplacements du sol, pour trois cas d'études associés à différents phénomènes géophysiques et processus sous-jacents. L'objectif de cette thèse est double : (1) révéler et quantifier les caractéristiques spatio-temporelles du glissement asismique le long de la rupture du séisme d'Izmit du 17 août 1999, et discuter de leur relation potentielle avec les propriétés de la faille (lithologie, géologie); (2) étudier la subsidence du sol dans des zones urbaines ou des zones exploitées par l'homme, induite par divers facteurs, et discuter des rôles relatifs de la tectonique, de la lithologie et des activités anthropiques dans ce mouvement du sol.

Dans la première étude de cas, j'ai combiné des mesures InSAR, à partir d'images radar TerraSAR-X (bande X) et Sentinel-1 AB (bande C) acquises sur la période 2011-2017, à des mesures GPS en champ proche, effectuées tous les six mois à partir de 2014 jusqu'en 2016, ainsi qu'à des mesures de creepmeter, pour analyser le champ de vitesse en surface autour de la NAF, après le tremblement de terre d'Izmit de 1999. Dans cette étude, la méthode de Stanford pour les réflecteurs persistents (StaMPS) a été utilisée pour traiter des séries d'images radar Sentinel 1 A (acquises le long d'orbites ascendantes et descendantes) et TerraSAR-X (orbites ascendantes). Les champs de vitesse moyenne horizontale InSAR révèlent que le taux de fluage (« creep ») sur le segment central de la rupture d'Izmit continue de décroître, plus de 19 ans après le séisme, ce qui concorde globalement avec les modèles de décroissance logarithmique des glissements post-sismiques de type « afterslip ». Le long de la section de la faille rompue à une vitesse « supershear » lors du séisme d'Izmit, le fluage se poursuit à une vitesse pouvant atteindre 8 mm / an. Un événement transitoire significatif, avec un fluage en accélération, est également détecté en décembre 2016 sur la série temporelle Sentinel-1, en accord avec les mesures d'un creepmeter installé près de la zone où la vitesse de fluage est maximum. Il est associé à un déplacement de surface total de 10 mm accumulé en un mois seulement. Des analyses complémentaires des champs de vitesses verticales montrent une subsidence persistante au pied de la faille normale de Golcuk, également rompue lors du séisme d'Izmit. Nos résultats démontrent que les processus de relaxation post-sismique le long de la faille nord-anatolienne, à l'est-sud-est d'Istanbul, sont plus complexes que proposé précédemment, avec des variations spatio-temporelles le long de la faille.

La deuxième cas d'étude porte sur l'identification et la mesure de la déformation du sol long-terme à Istanbul à partir d'une série InSAR couvrant près de 25 ans d'observations radar par satellite (1992-2017). Cette série temporelle InSAR a été calculée à partir d'images radar de plusieurs satellites (ERS-1, ERS-2, Envisat, Sentinel-1 A, B) afin d'étudier l'étendue spatiale et le taux de subsidence du sol dans la mégapole d'Istanbul. En combinant les différents jeux de données InSAR multi-traces (291 images au total) et en analysant les réflecteurs persistants (Ps-InSAR), nous présentons des champs de vitesse moyenne en ligne de visée, projetées ensuite en cartes de vitesse de la surface du sol dans des zones cibles d'Istanbul. Elles montrent différents sites situés le long des régions terrestres et côtières d'Istanbul qui subsident à des vitesses variant entre 5 mm / an et 15 mm / an environ. Les zones de subsidence les plus significatives sont associées à la fois à des facteurs anthropiques et à des lithologies relativement « faibles » le long de la vallée de Haramirede en particulier, où la subsidence observée peut atteindre ~ 10 mm / an. Le long du fleuve Ayamama, nous montrons que la vitesse de subsidence peut aller jusqu'à 10 mm / an depuis 1992, et qu'elle a également ralenti avec le temps à la suite de la restauration du système fluvial. Nous identifions également une subsidence à un taux d'environ 8

mm / an le long de la région côtière d'Istanbul, que nous associons à la remise en état des terres, ainsi qu'un affaissement très localisé à un taux d'environ 15 mm / an à partir de 2016 autour d'un des gratte-ciel les plus élevés d'Istanbul, construit en 2010. Dans le troisième cas d'étude, une série InSAR est calculée pour quantifier la subsidence de la plaine de Bursa (sud de la région de Marmara en Turquie), auparavant interprétée comme d'origine tectonique. Dans cette étude, StaMPS est utilisé pour traiter des séries d'images radar Sentinel 1 A-B acquises entre 2014 et 2017 le long d'orbites ascendantes et descendantse. Le champ de vitesse verticale obtenu après décomposition des champs de vitesse en ligne de visée sur deux traces complémentaires révèle que la plaine de Bursa s'affaisse à des vitesses allant jusqu'à 25 mm / an. A l'est, le signal de subsidence le plus important dans le bassin forme une ellipse allongée est-ouest et est limité par une plaine alluviale Quaternaire subsidant à environ 10 mm / an. Un autre signal de subsidence localisé est situé à 5 km au nord de la ville, le long du cône alluvial de Bursa, avec des vitesses allant jusqu'à 25 mm / an. La comparaison entre les variations temporelles des déplacements en surface et les variations de la pression de l'eau dans l'aquifère permet d'estimer la compressibilité de l'aquifère, α. Il se situe dans la gamme de $0.5 \times 10^{-6} - 2 \times 10^{-6}$ Pa^{-1}, ce qui correspond aux valeurs typiques des sédiments argileux et sableux. Nous trouvons une corrélation claire entre les zones de subsidence et la lithologie, ce qui suggére un contrôle lithologique fort sur la subsidence observée. De plus, les taux maximum de subsidence correspondent aux zones où l'activité agricole repose sur l'exploitation des eaux souterraines. La série de déplacements InSAR au cours de la période d'observation est bien corrélée aux changements de profondeur de la nappe phréatique. Ces observations indiquent que l'accélération récente de la subsidence est principalement due aux activités anthropiques plutôt qu'aux mouvements tectoniques.

Pour finir, cette thèse souligne donc la capacité de la méthodologie InSAR pour cartographier et quantifier finement des vitesses de déplacement de l'ordre du mm/an associées à différents phénomènes géophysiques, dans quelques zones cibles du nord-ouest de la Turquie. Pour mieux comprendre les mécanisme de déformation de la croûte terrestre et différencier les déformations de surface lentes induites par les activités tectoniques ou humaines, d'autres travaux, complémentaires à InSAR, seraient nécessaires pour permettre la surveillance et la prévention des risques géologiques régionaux.

1. INTRODUCTION

A better understanding of the complex behaviour of active faults represents a crucial challenge to assess geohazards. Detection and measurement of ground deformation along earthquake prone zones is of great importance for determining the possible future damage and taking developing precautions to avoid or minimize the risks for human life and structures. Ground deformations induced by a variety of natural phenomena (such as earthquakes, landslides and volcanic eruptions etc.) and human-driven activities (e.g., ground-water extraction, excavation, tunnelling etc.) have a wide range and vary in space and time. For example, tectonically-driven ground displacements vary from millimeters to meters occurring in seconds to years, at small scale as at global scale. They are related to plate tectonics and the earthquake cycle (Thatcher, 2006, first concept proposed by Reid, 1910). On the other hand, land subsidence as well is one of the most diverse forms of ground deformation processes, that vary from local collapses to regional-scale subsidence. Depending on the origin of the subsidence, vertical displacements may also be associated with horizontal ones that may cause serious damaging effects and structural instability. Considering all these aspects, observation of crustal deformation using satellite geodesy (InSAR and GPS) is profoundly important to advance the understanding of the control parameters of these ground deformations and to assess geohazard with the goal of environmental protection and population safety. In order to reduce such hazards, to take their evolution under control, accurate and continuous measurements of the surface deformation need to be provided to public administrations.

The employment of satellite based geodetic measurement technique for geological hazard assessment has dramatically increased during the last two decades in a range of different ways. In this way, remote sensing data have an immense area of utilisation in the different phases of the disaster management cycle (Joyce, et al., 2009). In particular, it can contribute to a rather long-term hazard assessment or in some cases to rapid evaluation of the likely risk of an event occurring, or to the post event damage mapping. Especially, the recent developments in satellite technology

and growing demand over time have accelerated the generation of rapid, dense and accurate information related to the earth surface deformation. High-quality optical and SAR images are two most common data sets being used for this purpose presently. In this dissertation, high temporal resolution radar images data sets are applied to different case studies of ground deformation induced by tectonic, lithology and anthropogenic activities that can be detected using Interferometric Synthetic Aperture Radar (InSAR) methods in northwest Turkey.

After the launch of ERS-1 satellite in 1991, the InSAR technique was first applied to map the coseismic surface displacement caused by the 1992 Landers earthquake (Massonnet et al., 1993). Since then, it has become a widely used surface displacement-mapping tool, with significant improvements to measure smaller and slower displacements. The most advantageous side of using InSAR technique is that the displacement of the millions of points over a large (100x100 km) surface area of the Earth can be determined with a high accuracy at a low cost without performing any ground-truth survey in the field. In the past two decades, the InSAR data provided results for a wide spectrum of applications such as continental earthquakes (e.g. Cakir et al., 2003; Sudhaus and Jónsson, 2011), post-seismic deformation (e.g. Ryder et al., 2007; Biggs et al., 2009, Cakir et al., 2012), interseismic deformation (e.g. Cavalié et al., 2008; Wang et al., 2009, Cakir et al., 2014), aseismic slip (e.g. Cakir et al., 2005, 2012; Champenois et al., 2012) and subsidence (e.g.Temtime et al., 2018) have been reported in numerous studies.

Our aim here is to analyse the temporal and spatial characteristics of surface deformations in Northwest Turkey by integrating InSAR and GNSS measurements, geological and hydrogeological data as well as ground-truth observations such as creep meter data, to discuss various geophysical processes and their driving mechanisms. The surface deformation that we monitored in northwest Turkey in a general framework of geohazard assessement and mitigation has been discussed comprehensively in three independent publications.

1.1 Contributions

The intention of this study is two-fold: (1) to highlight the potential of high-resolution InSAR data to refine the spatial distribution of shallow creep along the 1999 Izmit rupture, characterize its temporal behaviour and interplay with fault

geometry and lithology; and (2) to monitor the areas affected by land subsidence and quantify the temporal and spatial evolution of these subsidence signals, in order to determine the vulnerable part of the cities that are prone to geohazards and discuss their controlling factors (tectonics and lithology in particular). Below is the summary of the main contributions of this work:

1. We demonstrate here the potential of high-resolution InSAR data to refine along-strike variations of creep and characterize its spatio-temporal behaviour along the 1999 Izmit rupture.

2. Spatio-temporal characterization of creep is essential and will contribute to seismic-hazard assessment maps along the Izmit rupture and its vicinity.

3. We find that the nature of afterslip along the North Anatolian Fault east-southeast of Istanbul is more complex than previously proposed, revealing the existence of transient accelerating creep events.

4. We identify several sites along the coastal and terrestrial regions of Istanbul that underwent significant vertical and horizontal ground deformation at varying rates by using unique twenty-five years of satellite radar observations. In this sense, given the high vulnerability of the mega-city of Istanbul to natural disasters, such as earthquakes, landslides, or floods, due to heavy and unplanned urbanization practices, we believe that our research will provide insights and directions for hazard mitigation to the Public Administrations.

5. We identify the subsidence mechanism of the Bursa Plain (southern Marmara region of Turkey), by integrating InSAR time-series and geological and hydrogeological data, which is related to anthropogenic activities (water extraction) rather than tectonics.

1.2 Thesis Roadmap

Chapter 2 provides a brief, non-exhaustive overview of the literature related to the earthquake cycle, aseismic slip and the question of how creeping faults contribute to seismic hazard. We also briefly outline the seismo-tectonic setting of the Anatolian Plate and the creeping segments along the North Anatolian Fault, including insights provided by geodetic observations (GPS, InSAR). We outline the motivation behind this study that basically lays in geohazards evaluation and mitigation.

Chapter 3 presents the InSAR methodology and in particular the Persistent Scatterer approach used in this study to generate interferograms and displacement time series.

Chapter 4 to 6 are written as independent studies based on three articles that have been published in peer-reviewed journals. These three independent manuscripts work into a coherent argument in the context of this dissertation. The author of the present thesis is the first author of these three publications and was the main contributor to the work.

Chapter 4 is entitled *"Shallow creep along the 1999 Izmit earthquake's rupture (Turkey) from high temporal resolution InSAR data (2011-2017)"*. I analyse the spatiotemporal evolution of surface displacement along the central section of the 1999 Izmit earthquake with an unprecedented temporal resolution, using 307 SAR images acquired between 2011 and 2017, combined with GPS campaign and creep meter measurements. I use simple elastic dislocation model to estimate the relevant parameters of the Izmit fault and creeping characteristics along the rupture. I discuss the lithological origin and tectonic implications of this observation. This chapter is the backbone and in support of my 1st thesis objective as presented above. The work in this section is published in the Journal of Geophysical Research (JGR), Solid Earth as Aslan et al. (2019).

Chapter 5 is entitled *"Analysis of Secular Ground Motions in Istanbul from a Long-Term InSAR Time-Series (1992-2017)"*. In this chapter, I present the surface displacements driven by different factors during twenty-five years using 291 C-band SAR images by combining multi track/sensor InSAR datasets. We provide insights into the potential hazard induced by local soil conditions and anthropogenic effects. We identify several distinctive subsidence patterns and their spatio-temporal characteristics during the last two decades. The work is published in Remote Sensing Journal as Aslan et al., (2018).

Chapter 6 is entitled *"Investigating subsidence in the Bursa Plain, Turkey, using Ascending and Descending Sentinel-1 Satellite Data"*. I describe new results and interpretation on the subsidence of Bursa Plain in southern Marmara region of Turkey from Sentinel 1-A/B images collected between 2014-2017, which had been previously proposed to result from tectonic motions in the region. We detect ground subsidence at rates ranging from 5 to 25 mm/yr in an area of 200 km2 and propose

that it is due to groundwater extraction, not tectonic motions. The work in this chapter in published in Remote Sensing Journal as Aslan et al., (2019).

Chapter 7 summarizes some conclusions and recommendations for future work in the region.

Appendix A shows the GPS horizontal velocity used in Chapter 4. **Appendix B** shows results of atmospheric phase delays removal for each frame used in Chapter 4. **Appendix C** describes the uncertainties on horizontal and vertical velocities obtained from InSAR data inversion in Chapter 4. **Appendix D** shows the probability distributions obtained from Monte Carlo Markov Chain exploration of the model parameters.

2. BRIEF REVIEW OF LITERATURE

2.1 The Earthquake Cycle

Earth deformation driven by plate-tectonic movements is a multi-phase process and occurs in a large spectrum of timescales ranging from seconds (dynamic/seismic deformation) to millions of years (tectonic deformation) (e.g. Avouac, 2015 Rosenau, 2017). However, characterizing the nature of a complete earthquake deformation cycle is not straightforward due to the long recurrence intervals of the large earthquakes (Meade et al., 2013). In view of such a long-term timescale, historical and instrumental records only provide a snapshot of the present-day deformation field in a specific period. Contemporary geodetic observations time spans (GNSS and InSAR) typically range from days to 30 years that are encompassing only a tiny fraction of the deformation cycle. That is why such a short time span of modern geodetic deformation monitoring necessitates comparative studies at different stages of the deformation cycle, and requires complementary studies at different time scales from Quaternary tectonics. It remains a major challenge to obtain a complete overview of the earthquake cycle on a given fault system.

Reid's elastic rebound model (Reid 1910) is known as the first and simplest explanation for how accumulated elastic strain energy is released during earthquakes, and was derived from displacement observations before and after the 1906 San Fransisco earthquake. The idea is based on cyclic accumulation and release of elastic strain along an active fault, using accurate surveys in the vicinity of the San Andreas fault. According to Reid's theory (Figure 2.1), the earthquake deformation cycle can be divided into two periods: the period of slow accumulation of elastic strain during the intervening period referred to as *interseismic phase*, followed by a sudden rupture known as *coseismic phase.* A third phase of the earthquake cycle, referred to as *post-seismic phase,* was discovered in the early 1950s in Japan (Okuda, 1950, Okada, 1953) and refers to slip that occurs days to decades after an earthquake.
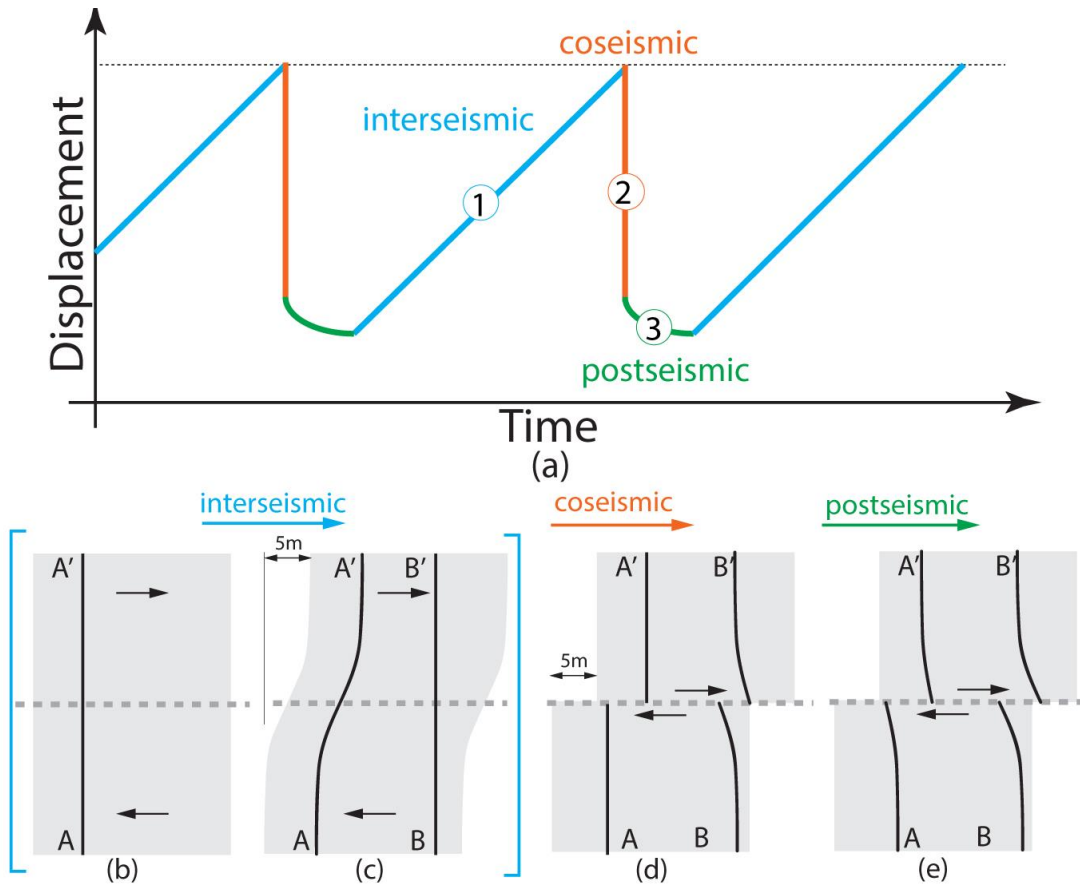
Figure 2.1: Sketch of the deformation cycle and survey markers at three different phases of the earthquake cycle (modified from Wright, 2002). (**a**) Theoretical geodetic time series (**b**) Marker is a straight line A-A' across the fault, in the instant after the last earthquake. **c**) Displacement and distortion of profile A-A' due to interseismic strain accumulation 250 year later. Straight profile B-B' is an observed profile immediately before the earthquake in (**c**) with an offset of 5 m at the fault. **d**) 10s of seconds after this earthquake, AA' markers has been displaced 5m near the fault and is no longer distorted. BB' is aligned in the far field and offset/distorted in the near field. e) Surface markers continue to deflect due to strain readjustment during the postseismic phase.

2.1.1 Interseismic period

As seen in Figure 2.1, between two successive earthquakes (coseismic phases in orange) that correspond to instantaneous offsets, two distinct periods exist: 1) the postseismic phase that shows a transient mechanical response of the lithosphere and 2) the interseismic phase that refers to the secular and steady deformation recorded later in a seismic cycle. In reality, individualizing the interseismic accumulation strain phase may be more complex due to delayed post-seismic deformation (Hetland et al., 2010, Trubienko et al., 2013) and other slow, transient slip events (Radiguet et al., 2012).

During the interseismic period,.expected surface displacement rates are small, on the order of millimeters per year. Therefore, geodetic measurements of crustal movements during the interseismic period require long time series in order to better quantify strain accumulation along the fault.

As mentionned above, the interseismic deformation was first observed by Reid (1910) using repeated geodetic-survey measurements from the angular separation of permanent survey markers in a trilateration network. Later, this conventional method was replaced by laser ranging method in early sixties (e.g. Savage and Prescott, 1978), with new GNSS measurements in early eighties (e.g. for the North Anatolian fault Straub et al., 1997; Reilenger et al., 2006), and finally InSAR in early nineties (e.g. Massonnet et al., 1993). Both GNSS and InSAR now provide precise measurements of crustal interseismic velocities with uncertainties on the order of (sub)-millimeters per year.

We know that the Earth's upper crust behaves as brittle material that accommodates stress accumulation leading to the earthquake, whereas the underlying lower crust and mantle creep continuously or transiently due to tectonic loading (Figure 2.2.a). In a homogeneous elastic half-space, the steady state interseismic displacement rate across a strike-slip fault is classically modelled using elastic screw dislocation model (Weertmann and Weertman, 1964; Savage and Burford 1973). The model assumes pure strike slip on a vertical fault. In this model, velocity does not dependend on the shear modulus and the fault perpendicular interseismic velocity (v) is given by

$$v = v_0 \pi^{-1} tan^{-1}(x/H) \qquad (2.1)$$

where x is the distance from the fault trace, H is the elastic locking depth which is considered as the same as the seismogenic depth (Wright et al., 2013) and v_0 is the deep steady slip rate (e.g. Savage and Burford, 1973). The velocity profile across the fault zone is characterized by a smooth transition. In this model, the fault is treated as a buried, infinitely deep and planar surface. The upper brittle crust (i.e. coseismic layer) corresponds to the locked part of the dislocation from surface down to depth 'H' and the down-dip extension of the fault zone is freely slipping at an average rate of v_0 that corresponds to the tectonic loading rate.

The strain around a fault is caused by the opposite sense of motions of blocks/plates when it is locked/stuck due to friction on the fault surface. In earthquake

terminology, the ***strain*** is the measure of deformation (change in length) representing the displacements between two moving blocks relative to a reference length along the fault. Therefore, considering the elastic properties of the rocks in the upper crust, strain is a measure of stored energy and characterizes the deformation under stress. For a given fault-perpendicular velocity field, the shear strain $\dot{\varepsilon}$ at the free surface is derived from equation 2.1 given by

$$\dot{\varepsilon} = \frac{v_0}{2H\pi}\left(\frac{1}{1+\left(\frac{x}{H}\right)^2}\right) \tag{2.2}$$

Figure 2.2 shows forward calculations of interseismic fault perpendicular velocities and the corresponding strain rates for different values of slip rate and locking depth. For a constant slip rate (Figure 2.2 -b and -c), higher locking depth means broader deformation zone and lower strain rate at the fault. On the other hand, for a constant locking depth (Figure 2.2 –d and –e), an increase in the slip rate results in larger strain rates at the fault.
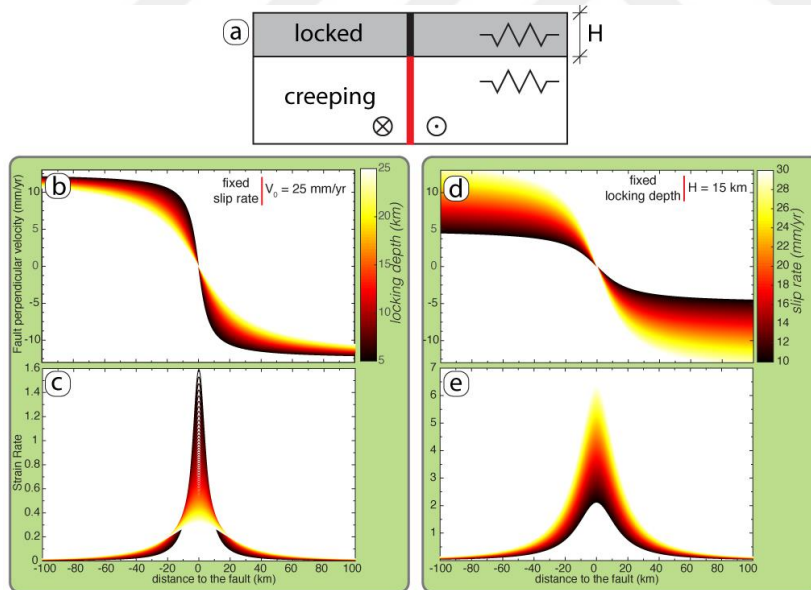
Figure 2.2: Forward calculations of interseismic fault perpendicular velocity (top) and strain rates (bottom) using the screw dislocation model (Savage and Burford, 1973). (**a**) Vertical cross section of simple layered elastic block model. The vertical dark black line in the upper gray layer is elastic and seismogenic part of the fault zone. The red line shows the freely slipping part in the lower part of the fault. (**b**) and (**c**) are the results for a fixed slip rate (25 mm/yr) and varying locking depths. (**d**) and (**e**) are the results for ta fixed locking depth (15 km) and varying slip rates.

2.2.1 Aseismic creep and seismic potential

In classical view of earthquake faulting, active faults release abruptly years of accumulated strain (Davison, 1901; Reid, 1910, 1911). Within this perspective, the fault is considered mainly locked during the intervening period. On the other hand, some other faults slip (creep) continuously or transiently at slow rates with or without producing any destructive earthquakes (e.g. Tratchet, 1979; Burfold & Harsh, 1980). These steady or transient slip (creep) behaviours are occurring within or around the seismogenic zone along the faults which then may store little to no strain energy (Hussain et al 2016). Better understanding the mechanism of aseismic creep is important because it can influence the size and timing of large earthquakes. The studies over the last decades using classical alignment arrays, creep meters, GPS and InSAR observations have showed the aforementioned fault-creep activities at varying depths and rates in the seismogenic crust. Creeping faults also generate earthquakes but usually less frequently and/or of smaller size than the fully locked fault segments (Schmidt et al., 2005; Jolivet et al., 2013; Kaneko et al., 2013; Cetin et al., 2014; Maurer & Johnson, 2014). Therefore, determining the relative budget of seismic and aseismic slips, as well as their spatiotemporal interactions and relationship with fault properties, is crucial for determining the seismic potential of active faults (Bürgmann et al., 2000, Bürgmann & Thatcher, 2013; Avouac 2015; Harris 2017, Bürgmann, 2018). Aseismic slip can occur with various temporal behaviours: it can be *steady* (e.g. Fialko, 2006; Motagh et al., 2007), as observed during the interseismic period, or *transient* (e.g. Hayes et al., 2014), either triggered by a major earthquake and decaying with time (postseismic relaxation known as afterslip, e.g. Lienkaemper et al., 2001) or *spontaneously* generated by processes still poorly understood (Jolivet et al., 2015; Rousset et al., 2016). Frictional properties, fault geometry and lithology, as well as pore fluid pressure variations were proposed to explain creep behaviour (Avouac, 2015; Burgman, 2018). For example, the presence of clay-rich gouges and high fluid pressure appear as key factors to generate creep (Carpenter et al., 2011, Kaduri et al., 2017).

Observations of aseismically slipping faults thus stimulate critical questions about creep relevance for seismic hazard assessment (Harris et al., 2016). From a mechanical point of view, creeping behaviour of a fault is an important mechanism that plays a role in the releasing of elastic strain energy in the fault. Aseismic slip

may thus be considered as a reducing factor of the seismic moment (energy) of future earthquakes. However, several case studies show that aseismic slip may also trigger earthquakes (e.g. Radiguet et al., 2018).

Figure 2.3 shows the forward calculations of interseismic fault-perpendicular velocity and strain rate profiles of a shallow creeping fault for different creeping rates. The fault-perpendicular velocity profile shows two different types of deformation signals: (1) a long-wavelength signal related to the deep tectonic loading rate, and (2) a velocity discontinuity caused by surface creep at the fault. The higher rate and depth of creep and lower strain rate concentrated close to the fault explain the direct relationship between the fault energy released by seismic (earthquakes) and aseismic (creep) processes at the fault.

Recent development and widespread use of advanced spaceborne techniques, particularly InSAR, have revealed that steady or transient surface creep behaviour along major continental faults is more common than previously thought. A recent review by Harris (2017) discusses the earthquake potential of creeping continental faults using worldwide data. Reported cases in the literature include the Hayward fault (Savage and Lisowski, 1993; Schmidt et al., 2005), the Superstition Hills fault (Bilham, 1989; Wei et al., 2009) and the Central San Andreas fault in California (DeMichele et al., 2011, Jolivet et al., 2015b, Khoshmanesh and Shirzaei 2018), the Longitudinal Valley fault in Taiwan (Champenois et al., 2012; Thomas et al., 2014), the Ismetpasa segment of North Anatolian Fault in Turkey (Ambraseys, 1970; Cakir et al., 2005; Kaneko et al., 2013; Cetin et al., 2014; Bilham et al., 2016; Rousset et al., 2016), the Izmit segment of the North Anatolian Fault (Cakir et al., 2012; Ergintav et al., 2014; Hussain et al., 2016), the Haiyuan fault in China (Jolivet et al., 2012, 2013, 2015a), the El-Pilar fault in Venezuela (Jouanne et al., 2011, Pousse-Beltran et al., 2016), and the Chaman fault in Pakistan (Fattahi & Amelung, 2016). These studies show that the spatial patterns (distribution along strike and depth, magnitude) and temporal behavior of creep (steady versus sporadic [creep bursts] creep) vary significantly. These variations may be exploited to develop a better understanding of aseismic slip processes and their relationships with seismic hazard (Avouac et al., 2015).
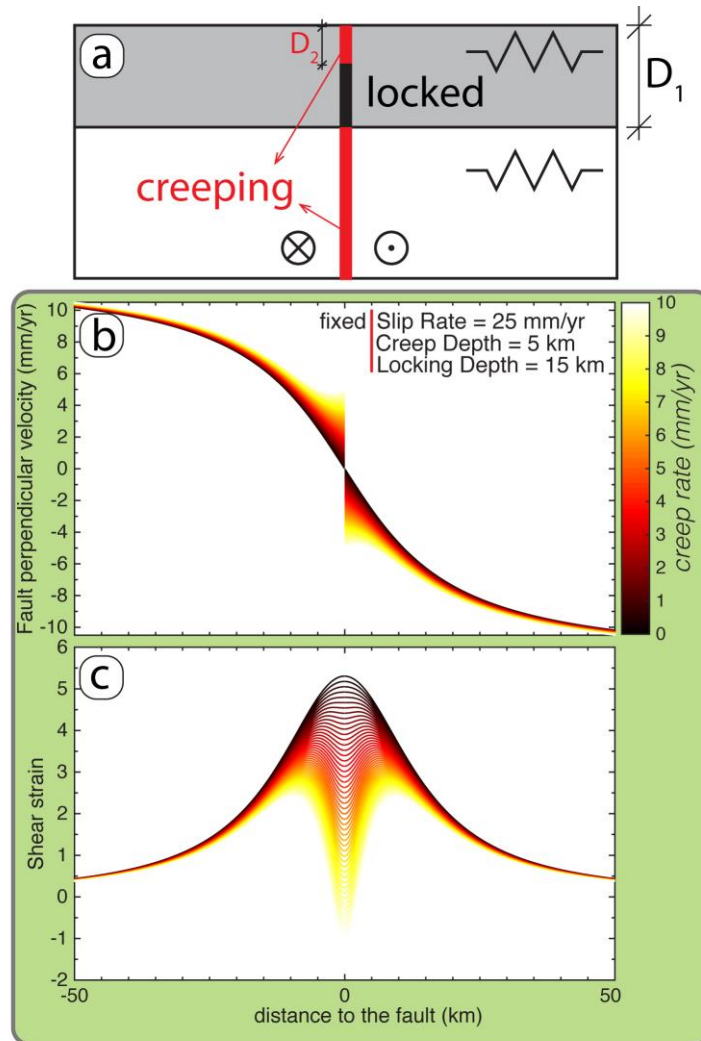
Figure 2.3: Profiles of interseismic velocity and strain rate across a strike slip fault using the combination of screw dislocation model (Savage and Burford, 1973) with opposite sense of motion and .Heavyside function (**a**) Vertical cross section of simple layered elastic block model. The vertical dark black line in the upper gray layer is elastic and seismogenic part of the fault zone. The red line shows the freely slipping part in the lower and upper part of the fault. In this configuration, creep occurs from surface down to a shallow depth D_2. (**b**) and (**c**) are the results for a fixed slip rate (25 mm/yr), creep depth (5 km) and locking depth (15 km) for the fault-perpendicular velocity and strain rate, respectively, with a varying creep rate. Note how strain rate becomes very localized at the fault for increasing creep rate.

2.3 The North Anatolian Fault (NAF)

The Anatolian plate is bounded by the right-lateral North Anatolian Fault and the left lateral East-Anatolian Fault to the north and east-southeast of Turkey, respectively. This plate is moving westward due to the convergence of the Arabian and Eurasian

plates and slab suction from the Hellenic trench (Reilinger et al., 2006). The 1600-km-long North Anatolian Fault is a major intracontinental strike-slip fault and known as one of the most tectonically active faults in the eastern Mediterranean region, with an average slip rate of 24±2 mm/yr (Reilinger et al., 2006). This right-lateral fault has ruptured between 1939 and 1999 in a sequence of eight M>7 earthquakes, with a westward migration that started near the Karliova triple junction in the east and reached the Sea of Marmara in the west. This migration has been explained by the Coulomb stress transfer during and in between the successive earthquakes along strike (Stein et al., 1997). Assessment of seismic hazard in the Marmara region suggests that a large and earthquake (M>7) may occur with a probability of >50% in the next 30 years under the Sea of Marmara, 20 km south of Istanbul (Parsons et al., 2004; Armijo et al., 2005).
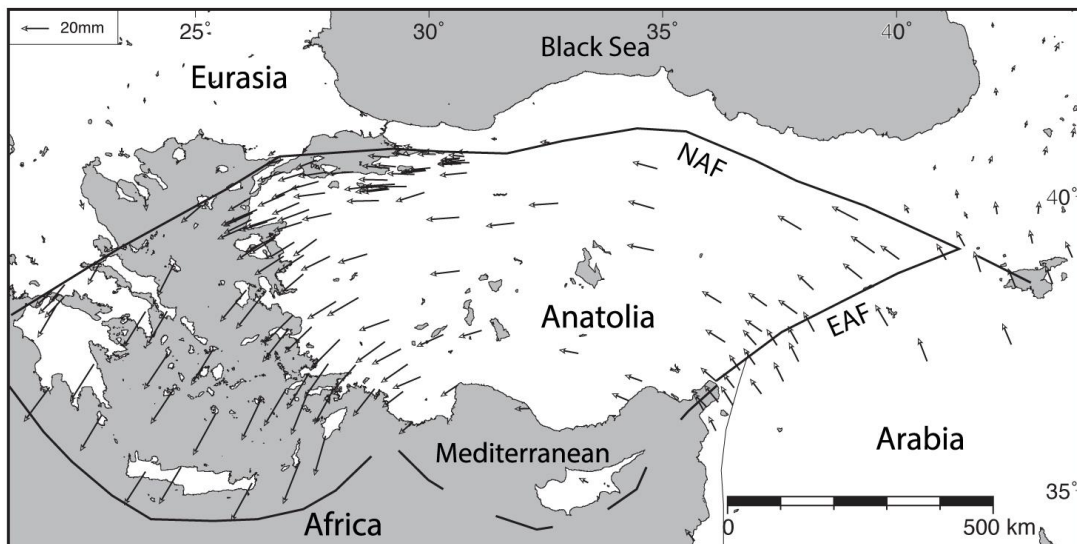
Figure 2.4: Anatolia plate's relative motion with GPS horizontal vectors in Eurasia fixed reference frame (Reilinger et al., 2006).

2.3.1 Postseismic creep along the North Anatolian Fault

The Ismetpasa and Izmit segments of the North Anatolian Fault are the two sections on land that exhibit shallow aseismic creep in the uppermost few km of the upper crust. Creep is also inferred below the Marmara Sea from the study of microseismicity and geodesy (Ergintav et al., 2014; Schmittbuhl et al., 2016a and 2016b; Klein et al., 2017) and recent sea-floor observations have shown the existence of transient creep events (De Michele et al., 2017; Martínez-Garzón et al., 2019). Based on the observations of the slow displacement of a wall at the train station of

Ismetpasa in the period 1957-1969, and railway maintenance reports, the fault creeping behaviour of the NAF at Ismetpasa was first documented by Ambraseys (1970), a decade after the first observation of this phenomenon on the San Andreas Fault (Steinbrugge et al, 1960). Various measurements afterward (GPS, InSAR, Light Detection and Ranging -LIDAR-, creep meter, field observations) allowed to better characterize the spatio-temporal properties of creep along the Ismetpasa fault section (Aytun, 1982; Eren 1984; Deniz et al., 1993; Cakir et al., 2005; Ozener et al., 2012; Kaneko et al., 2013; Cetin et al., 2014; Rousset et al., 2016; Bilham et al., 2016; Kaduri et al., 2017). The creep rate is decaying with time following the 1944 rupture (Cetin et al., 2014), so that creep has been interpreted as postseismic relaxation (Cakir et al., 2005). Gouges formed within the fault zone rocks contain low friction minerals that could explain the creeping behaviour of the fault (Kaduri et al., 2017) and microstructures of deformation show the existence of both creep and brittle deformation mechanisms in the fault zone (Kaduri et al., 2018).
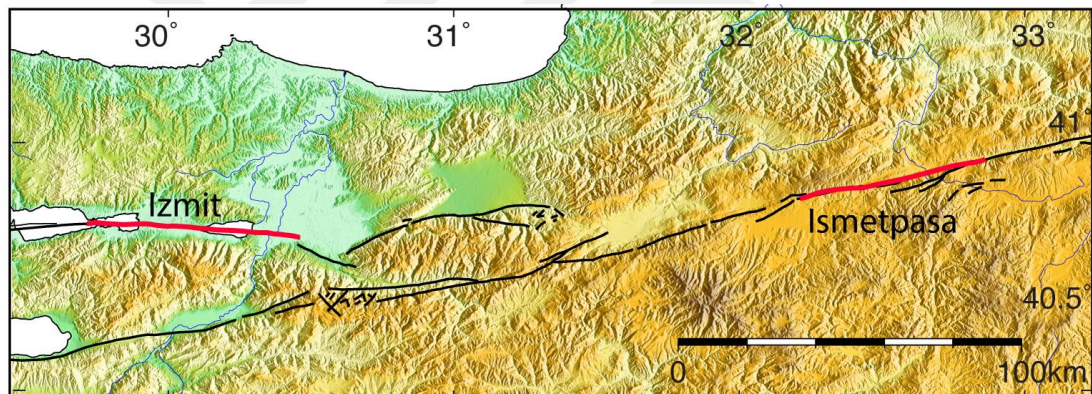
Figure 2.5 : Creeping segments of the North Anatolian Fault. The active faults (Emre et al., 2013) and creeping segments are drawn with thin black and bold red lines, respectively.

The Izmit creeping section of the North Anatolian Fault was the locus of the M_w 7.4 Izmit earthquake on 17 August 1999. This earthquake ruptured 145 km of the western section of this fault, along five segments separated by releasing step-overs. The rupture extended from Düzce in the east to the submarine segment of the Hersek delta in the Marmara Sea in the west (Barka et al., 2002; Figure 1). The 1999 Izmit rupture propagated at a supershear rupture velocity (5 km/s) over a large part of the fault zone (Bouchon et al., 2001). This earthquake was followed by the M_w 7.2 Düzce earthquake 86 days after, which ruptured a 45 km-long segment of the North Anatolian Fault (Cakir et al., 2003a; Konca et al., 2010). The Izmit earthquake

modified the stress distribution on this fault and played an important role in the occurrence of the Düzce event by promoting stress change and postseismic deformation transients (Hubert-Ferrari et al. 2000; Cakir et al., 2003b).

First observation of creep along the central segment of the Izmit rupture was documented by Cakir et al. (2012), using GPS and a Persistent Scatterer Interferometry (PSI) analysis of 24 ERS SAR images, acquired between 1992 and 1999, and 36 Envisat SAR images, acquired between 2003 and 2009. These authors investigated pre- and post-earthquake surface deformation along the supershear segment of the Izmit rupture and concluded that, as no creep was measured before the 1999 Izmit earthquake, the surface creep is related to postseismic afterslip, with a rate of 8-10 mm/yr. Using GPS data and additional Envisat images acquired between 2003 and 2012, from both ascending and descending orbits that allowed to better separate the horizontal and vertical components of creep, Hussain et al. (2016) reported that aseismic slip was confined to shallow depths (<10 km) and confirmed its decaying creep rate through time. Their results showed that creep extends spatially from the Gulf of Izmit in the west to the east of Sapanca Lake in the east, with an average horizontal, fault parallel slip rate of 6 mm/yr and a maximum rate of 11±2 mm/yr, which is nearly %40 of the annual tectonic loading rate (Reilenger et al., 2006, Hussain et al., 2018). Such slip deficit implies that elastic strain is still being accumulated on the fault along the Izmit section. Different models have been proposed to explain such postseismic deformation after the 1999 Izmit earthquake. Postseismic slip partly consists of afterslip on the fault plane and could be controlled by the frictional properties of the fault zone after a stress perturbation (Marone, 1998). Using a three-dimensional viscoelastic finite element method, Hearn et al., (2009) and Wang et al., (2009) proposed that the postseismic deformations in the region of the 1999 Izmit and Düzce events were the result of a combination of shallow afterslip and viscoelastic relaxation of lower crust and/or upper mantle.

The most recent radar satellite constellations, with greater spatial and temporal resolution, offer the opportunity to refine the measurement of aseismic slip phenomena and to further understand the underlying processes. As mentioned before, one goal of my thesis was to show the contribution of high-resolution TerraSAR-X and Sentinel-1 InSAR data sets to better characterize in space and time the aseismic slip along the Izmit section of the North Anatolian Fault.

2.4 Ground Subsidence

Ground subsidence is lowering of surface elevation. It represents widespread problems in urban areas built on thick, unconsolidated loose soil layers consisting of clay, silt and peat formations (Zeitoun et al, 2013; Changxing et al., 2007; Evinemi et al., 2016). Ground subsidence can severely and adversely impact the surface structures and infrastructure due to differential settlement of the ground elevation, ground slope and through the development of surface cracks (Fergason et al., 2015). Observation of subsidence is important for understanding the underlying geological phenomena or human-induced causes. Therefore, ground deformation measurements can provide very critical information for the protection of people's safety and property and for the prevention of geohazards.

Subsidence has been correlated to strata lithology, formation and structure (Wang et al., 2013; Tornqvistetal, 2008; van Asselen et al., 2011; Higgins et al., 2014). However, excessive groundwater pumping is by far the largest cause of subsidence. Dewatering of loose soil layers or highly porous rocks in which the water provides structural support produces volumetric contraction and hence surface subsidence.

Since the 1960s, a considerable amount of literature has been published on land subsidence using various methods of investigations, including conventional practices and advanced ground sensing systems. Data acquisition techniques depend on the spatial extent of the anticipated deformation and results were interpreted to characterize deformation mechanism and their environmental consequences (Dang et al., 2014). These conventional techniques include optical levelling surveys (Bitelli et al., 2000), GPS surveys (Sato et al., 2003; Gourmelen et al., 2007), groundwater monitoring (Taylor and Alley 2002) and tape-extensometers (Ireland et al., 1984; Poland, 1984; Evseev et al., 2018). Advanced techniques include airborne and space based observations such as InSAR (Hoffman et al., 2001; Rucker et al., 2013) and LiDAR (Froese and Mei, 2008), which can provide high-resolution imagery of the subsiding signal.

Following the development of new satellite technologies and advanced processing techniques, InSAR has been successfully used to investigate deformation resulting from subsidence due to withdrawal of groundwater or other fluids (Béjar-Pizarro et al., 2017; Massonnet et al., 1997; Fielding et al., 1998; Wright et al., 1999; Crosetto

et al., 2018), soil consolidation (Kim et al., 2010; Aslan et al., 2018), subsurface mining or collapse of old mines (Carnec et al., 2000; Abdikan et al., 2014), thawing subsidence (Rykhus et al., 2008), tectonic activity (Temtime et al., 2018), and soluble earth materials (Baer et al., 2018). Besides, InSAR has also been used to infer aquifer hydraulic properties such as compressibility and storage coefficient as well as the mechanics of aquifer system (Galloway et al., 1998; Béjar-Pizarro et al., 2017; Hoffmann et al., 2001; Tomás et al., 2009; Calderhead et al., 2011; Ezquerro et al., 2014).

We demonstrate here (Chapter 5 and 6) the contribution of Synthetic Aperture Radar (InSAR) time series analyses to better characterize the ground subsidence particularly in urban areas in northwest Turkey.

3. METHODOLOGY

3.1 Introduction

In this section, we outline the methodology of Interferometric Synthetic Aperture Radar (InSAR) processing and in particular the GMTSAR software and Persistent Scatterer approach used in this study to generate Interferograms and displacement time series.

InSAR data are widely being used in two main fields of applications: a) generation of Digital Elevation Models (DEM), and b) spatio-temporal detection and monitoring of surface deformation induced by various factors by combining a network of multiple interferograms over a region. It is the latter on which we will focus here. Modern spaceborne radar technology is a unique tool that provides great perspective for monitoring the spatiotemporal evolution of different surface deformations. The Synthetic Aperture Radar is a coherent active microwave imaging technique which operates in various bands of microwave frequencies (X-, L-, S-, P- and C-band) (Elachi, 1988; Curlander and McDonough, 199; Bamler and Hartl, 1998) (Table 3.1), It detects backscattered responses from the terrain and objects on it of an electromagnetic signal emitted by its own artificially-generated energy sources during day and night and nearly all weather conditions. New very high resolution (VHR) (down to to 1 m) X-band satellite missions (TerraSAR-X, Tandem-X, COSMO-Skymed) offer new possibilities for monitoring surface elements with an unprecedented level of spatial and temporal resolution, and accuracy thanks to high revisit frequency that were previously unavailable.

Table 3.1 : Microwave radar frequencies and their wavelengths.

Band	Frequency (GHz)	Wavelenght (cm)
P	<0.3	100
L	1-2	15-30
S	2-4	7.5-15
C	4-8	3.75-7.5
X	8-12	2.5-3.75

The conventional InSAR is able to map ground displacement due to many geophysical processes but mapping subtle and slowly evolving deformation processes such as aseismic surface slip requires more sophisticated processing approaches than the classical differential InSAR method which is often hindered by signal decorrelation and atmospheric errors. Advanced processing techniques increase the density of ground measurement and its robustness, reduce the associated errors due to atmospheric effects, Digital Elevation Model (DEM) errors, and orbital inaccuracies (Hooper et al., 2007) by using multiple SAR images of the same region (Ferretti et al., 2000, 2001). Unlike conventional InSAR method, the advanced techniques generate time series of surface displacement for every given ground targets using multi-temporal stacks of SAR data when these targets have constant echo over time. A velocity map shows the ground movement for each pixel averaged over the observation period whereas the time series analysis depicts the history of the surface position for each pixel at each acquisition time. In geophysics, scientists are interested in phenomena that results in surface changes for example earthquakes, landslides, volcanic activities and subsidence. That is why the time-series InSAR products are very useful for monitoring the geophysical processes.

3.2 Principles of InSAR

In theory, the phase component of a single SAR image collected with a single antenna is not meaningful and of no practical use (random noise). In order to perform any type of interferometric processing we need at least two independent SAR images (interferometric pair) acquired from slightly different viewing angles over the same region at different times. In its most basic form, standard InSAR processing is based on calculating the phase difference of the two acquired phase images ($\Delta\varphi$) of the reflected signals, which is known as radar *interferometry*, and the image form of $\Delta\varphi$ calculated for each resolution element (pixel) of the surface is called *interferogram* (Zebker et al., 1994). Typically, in InSAR terminology, the first SAR image is referred to as *master* and second image is labelled *slave* image. Prior to interferogram computation, the pixels in slave image are required to be aligned with that of the master to sub-pixel accuracy (e.g. Brown 1992; Hanssen, 2001). This alignment is being realized by coarse- and fine-coregistration with cross correlation in pixel and sub-pixel levels respectively.

In the following sections I briefly discuss the different phase contributions and the ways in which they can be estimated.

3.2.1 Contributors to signal phase

The computed differential interferometric phase $(\Delta\varphi)$, contains the surface displacement phase component $(\Delta\varphi_{displ})$ due to movement of the pixel in the satellite line-of-sight direction and a sum of "unwanted" (i.e. considered as noise for our geophysical applications) phase terms arising from several contributions :

- topographic phase component $(\Delta\varphi_{topo})$ arising from the different points of view of the master and slave images on the terrain and inaccurate DEM information,

- atmospheric phase contribution $(\Delta\varphi_{atm})$ due to variations of wave propagation conditions (change in the atmospheric properties – pressure temperature, humidity - and ionospheric dielectric constant),

- orbital phase contribution $(\Delta\varphi_{orb})$ due to inaccurate orbital information, and

- the noise (n) term arising from the variability in scattering features of the pixel, thermal noise and coregistration errors.

The interferometric phase can thus be expressed as

$$\Delta\varphi = (\Delta\varphi_{displ} + \Delta\varphi_{topo} + \Delta\varphi_{orb} + \Delta\varphi_{atm} + n) \qquad \textbf{(3.1)}$$

Apart from these phase contributions, another phase contribution may stem from the presence of phase unwrapping errors due to incorrect estimate of modulo 2π radians patterns (wrapped data).

To extract the true phase difference induced by the surface displacement, the phase contribution from flat earth and surface elevation (topographic and orbital components) needs to be accounted for by using precise orbits and a digital elevation model (DEM) of the area (Hanssen, 2001). In this study, the topographic phase contribution in the interferograms is removed using the SRTM 90-m posting DEM data (Farr et al., 2007). To correct the interferometric phase $(\Delta\phi)$ from the atmospheric component for all interferograms generated in this dissertation, the atmospheric phase delays were estimated using the ERA-Interim global atmospheric model (Dee et al., 2011). We used the TRAIN (Toolbox for Reducing Atmospheric

InSAR Noise) software toolbox (Bekaert et al., 2015) for estimating the radar delay by interpolating the atmospheric variables to the InSAR pixel locations for each SAR acquisitions.

3.3 Overcoming Limitations due to Decorrelation Noise

The reliability and accuracy of an interferogram obtained by SAR processing is limited by the problem of decorrelation on interferometric coherence (i.e., similarity between the acquisitions). The decorrelation can be temporal decorrelation which arises from changes on surface scatterer properties due to long period cover (such as vegetation growth, soil moisture, glacier motion, etc.) and increase with time between master and slave acquisitions. It can also be spatial decorrelation due to long baselines (distance between two antennas). Quantitative coherence information is very important for the performance of SAR processing. This decorrelation limitation arising from different sources (as well as other limitations due to random atmospheric delays for example) can be overcome by using new state-of-the-art InSAR time series methods combining information from multiple SAR acquisitions instead of just two images. Currently, there are two families of time-series InSAR technique incorporating information from multiple SAR acquisitions – Persistent Scatterer (**PS**) (e.g. Ferretti et al., 2001, Perissin and Ferretti, 2007, Hooper et al., 2007) and Small Baseline Subset (**SBAS**) (e.g. Berardino et al., 2002, Lanari et al., 2004, Biggs et al., 2007, Hooper, 2008) methods or a combination of both (Hooper, 2008) that identify areas where ground surface is least affected by spatial and temporal decorrelation.

3.4 Persistent Scatterer Method (PS)

As discussed above, the PS approach is based on the use of co-registered long series stack of SAR images (the larger the number of SAR data, the more precise and robust the results are) to generate differential interferograms with respect to one common master. It exploits the radar return signal backscattered from phase stable targets that function as corner reflectors due to their coherent phase center. It is developed to overcome some of the limitations of conventional InSAR decorrelation problems that give rise to disconnected areas in the interferograms in space and time (Hooper, 2006) and makes the geodetic interpretation difficult. Unlike the Small

Baseline method, the single-master interferogram method uses all possible interferometric combinations regardless of their spatial and temporal baselines values and temporal differences by optimizing the each resolution call containing single point scatterer. On the other hand, small baseline method is another InSAR stacking method that relies on appropriate combinations of SAR image pairs characterized by a small orbital separation (baseline) and with no selection of specific scatterers. PS-InSAR method is able to generate the average velocity and time series of displacements by measuring the displacements obtained with the set of interferograms.

As of today, there are various methods for identifying the PS pixels in interferograms (e.g. Ferretti et al. 2001; Crosetto et al., 2003, Adam et al., 2005 etc.). In this dissertation, we used the Permanent Scatterers Interferometry Synthetic Aperture Radar (PS-InSAR) technique to compute the displacement time series of each stable Permanent Scatterer pixel (PS) in the study area, based on a single master network in the Stanford Method for Persistent Scatterers (StaMPS) (Hooper, 2008; Hooper et al., 2012) package, that takes advantage of the spatial correlation between pixels. StaMPS uses only the selected pixels that show stable phase and amplitude noise characteristic in time to compute average velocities and time series. This method is considered to be a modified version of PS algorithm and is applicable in areas undergoing non-steady deformation, such as aseismic slip, without using prior knowledge of the temporal deformation model.
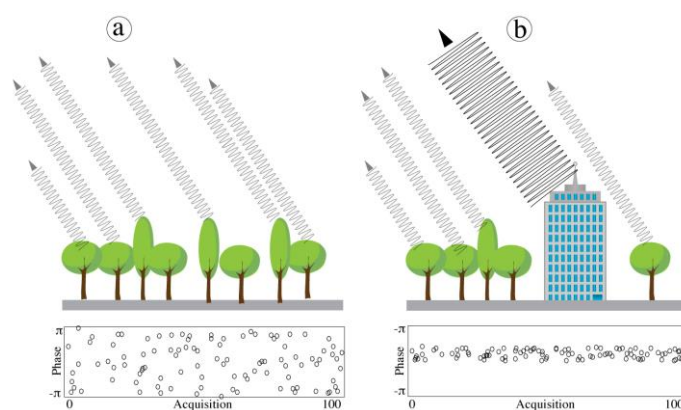
Figure 3.1 : Schematic diagram illustrating the difference of the phase simulation for 100 acquisition iterations for (**a**) a pixel with distributed scatterers showing dispersed signal values, and (**b**) a pixel with a dominant Persistent Scatterer pixel with small phase variations (modified from Hooper et al. (2007)).

The cartoons in Figure 3.1 represent the scatterers contributing to the phase of one pixel in an image. In case of non-stationary resolution elements such as vegetated or cultivated areas where scatterers "move" with respect to each other between satellite passes, the phase sum changes (Figure 3.1-a). In contrast, if the scatterers are dominated by a stable large reflector called a persistent scatterer (can be either manmade or natural features such as buildings, rock outcrop, towers etc.), it results in a stable phase over time (Figure 3.1-b).

I am giving in the next sections a detailed description of the procedures used in each step of the interferogram formation and the StaMPS PSI approach employed in this dissertation.

3.4.1 Procedures: from SLC to geocoded interferograms

For processing interferograms, we used the open-source radar interferometry software, Generic Mapping Tools Synthetic Aperture Radar (GMTSAR) developed by Sandwell et al. (2011a,b) that is based on Generic Mapping Tools (GMT; Wessel et al., 1998). Forming an interferogram using two Single Look Complex (SLC) images involves three basic steps using GMTSAR's main processors: 1) a preprocessor to convert each satellite data type and orbital information into a generic format; 2) an InSAR processor to focus, co-register images, remove topographic phase, and form the complex interferogram; 3) post processor based on GMT, to filter the interferogram and construct interferometric phase, amplitude, coherence and phase gradient. Unlike many other InSAR systems such as ROI_PAC, GAMMA and DORIS, GMTSAR relies on sub meter orbital accuracy, which greatly simplifies the SAR processing algorithms.

The focused SAR image contains backscatter amplitude (intensity) and phase (range) information for each pixel. This is the complex image. The amplitude component is the strength of backscattered radar signal from each resolution element that contains uncertainties that stem from terrain scattering features such as surface roughness, soil moisture and dielectric constant. The phase is the fraction of the full wave that represents the precise distance between satellite and target on the ground. Multiplying the first image by the complex conjugate of the second image forms the complex interferogram. The first step is coregistration of slave and master images in sub-pixel accuracy. In GMTSAR, this is done by 2 dimensional cross correlation

method of multiple small sub-patches taken from slave and master acquisitions (*xcorr.c* in GMTSAR). Then GMTSAR uses 6-parameter (3 along range and 3 along azimuth) affine transformation to align the images using the robust 2-D fit to the offset data (*esarp.c* in GMTSAR). After this step, the *phasediff.c* program computes the phase difference of the images by removing the effect of curved earth and baseline dependent topographic phase contribution prior to cross multiplication. The output file contains the real and imaginary components of a complex interferogram. After all the position and phase corrections are applied, a spatial low-pass filter (*filter/snaphu*) is applied in order to enhance the results of real and imaginary components of the interferogram and compute standard products of amplitude, phase and coherence. GMTSAR's unwrapping processor is based on snaphu (*snaphu.c*) unwrapping algorithm. Detailed description method of SNAPHU unwrapping method can be found in Hooper (2010).

The final step in the processing is to geocode all of the final products by transforming from radar (range and azimuth) coordinate system to geographical coordinate system (longitude and latitude).

3.4.2 Procedures: from Interferograms to PS time-series

The idetification of the PS pixels for the time series analysis is performed using single-look coherent interferograms. Following interferogram processing, we use the Permanent Scatterers Interferometry Synthetic Aperture Radar technique to compute the displacement time series at each PS in the study area using a *single master network* with StaMPS (Hooper, 2008; Hooper et al., 2012). StaMPS is a Matlab-based open source software that has been developed partially at Stanford University, the University of Iceland and Delft University of Technology. This PS-InSAR technique is an advanced method used to monitor surface deformation caused by tectonic or anthropogenic activities. The PSI method allows monitoring subtle and slow deformation signal, mitigating errors due to atmosphere, digital elevation model and orbital inaccuracies using spatial and temporal filtering. Unlike the amplitude based approach proposed by Ferretti et. al. (2001), StaMPS does not assume any priori hypothetical model of the deformation. StaMPS uses both amplitude and phase information to identify PS points. As the first step of pre-processing, the input dataset is converted into a format readable by StaMPS and an area of interest is chosen, that

must be included in all slave images. In an initial step, the selection of PS points is performed based on their noise characteristics, using an amplitude dispersion analysis. The amplitude dispersion criterion is defined by: $D_{Amp} = \left(\sigma_{Amp}/m_{Amp}\right)$ where σ_{Amp} and m_{Amp} are the standard and mean deviation of the amplitude in time, respectively (Ferretti et al., 2001). In the present studies, we selected a threshold value of 0.42 for D_{Amp} that minimizes the random amplitude variability and eliminates highly decorrelated pixels in some areas covered with vegetation, agricultural fields or snow. Once coherent PS points have been selected based on this amplitude analysis, the PS selection is refined by phase analysis in a series of iterations, which allows the detection of stable pixels even with low amplitude. The next steps of the StaMPS processing includes correction of the residual topographic component and 3D unwrapping of the PS phase both in time and space.

Unwrapped interferograms after PS selection are corrected from stratified tropospheric delays using the freely available Toolbox for Reducing Atmospheric InSAR Noise (TRAIN, Bekaert et al., 2015), based on the ERA-Interim (ERA-I) global atmospheric model. Corrected interferograms are then used to compute mean velocity fields in StaMPSv maps in study areas.

4. SHALLOW CREEP ALONG THE 1999 IZMIT EARTHQUAKE RUPTURE (TURKEY) FROM GPS AND HIGH TEMPORAL RESOLUTION INSAR DATA

4.1 Introduction

Earthquakes are the phenomena that caused by rapid release of elastic strain energy by a sudden slip events propagate along a fault. Estimation of the energy released by elastic strain for the future possible events are complicated by the occurrence of asesismic creep. A better understanding of seismic and aseismic slip behaviors of active faults is a crucial challenge for reliable assessment of seismic hazard (Avouac, 2015) as aseismically slipping part of the fault reduces the seismic moment that capable to produce earthquake. While most active faults are interseismically locked within the resolution of geodetic measurements and release abruptly the strain that has accumulated over long time, some other faults in particular locations slip continuously or transiently with an absence of destructive earthquakes (e.g. Thatcher, 1979; Burford & Harsh, 1980). Aseismic slip occurring within or around the seismogenic zone along continental faults is usually referred to as creep and it is an important indicator of the shear stress. Determining the lateral variation and temporal characteristic (steady-state or transient) of aseismic creep is highly important for understanding the mechanism of fault behavior (Galehouse, 1997; Lienkaemper et al., 1997, 2001). In this regard, knowing how slip and creep rates vary spatiotemporally has profound implications for seismic hazard assessment (Carpenter et al., 2011).

Studies based on Interferometric Synthetic-Aperture Radar (InSAR) and Global Positioning System (GPS) satellite observations until 2012 have shown that the central segment of the August 17, 1999 Mw 7.4 Izmit earthquake on the North Anatolian Fault began slipping aseismically following the event. In the present study, we combine new InSAR time series, based on TerraSAR-X and Sentinel 1A/B radar images acquired over the period 2011-2017, with near field GPS measurement campaigns performed every 6 months from 2014 to 2016.

4.2 GPS Data and Processing

To complement InSAR Sentinel-1 data in modelling the most recent creep rate along the Izmit section of the North Anatolian Fault, we used GPS data that we acquired from 2014 to 2016 during five campaigns (one every six months) along near field zone. Figure 2 shows the corresponding GPS velocity field for the study area. Details on GPS sites, velocities and associated uncertainties are provided in Appendix A. GPS data were processed using the GAMIT/GLOBK (V10.6) software developed by MIT (King and Bock, 2004; Herring et al. 2015), following the processing strategy in Ergintav et al. (2009).
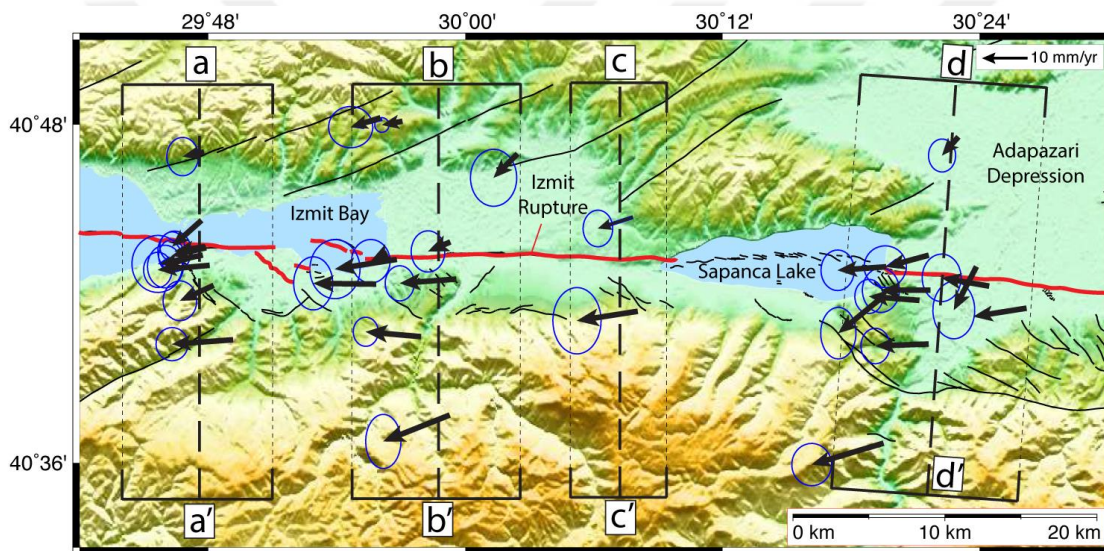
Figure 4.1 : GPS velocities and 95 % confidence ellipses for the period 2014-2016 plotted in Eurasia fixed reference frame (defined as in Reilinger et al., 2006). GPS profiles aa', bb', cc', dd' are projected onto InSAR profiles shown in Figures 4.8 and 4.12 for joint GPS/InSAR inversion.

4.3 InSAR Data and Methodology

4.3.1 Multi-sensor insar time-series

To monitor the surface creep behavior along the Izmit rupture in the period 2011-2017, we processed radar images from two different satellites and three different viewing geometries. In order to observe the deformation pattern at high spatial resolution, we used one X-band dataset of 32 TerraSAR-X images, acquired in StripMap mode along ascending orbit (track 24) between 2011 and 2015. TerraSAR-

28

X data sets were obtained through the GSNL Marmara Region Permanent Supersite (available at http://geo-gsnl.org/supersites/permanent-supersites/marmara-region-supersite/). We also used three C-band datasets with 275 images in total, from three tracks of the Sentinel 1A/B satellites operated by the European Space Agency (ESA), acquired along descending and ascending orbits (Tracks 58 [Asc], 160 [Asc], 138 [Dsc], Figures 1 and 3). Data span the period from October 2014 until July 2017. The 25 km-long Izmit-Sapanca Lake segment of the 1999 Izmit rupture is entirely covered by all tracks (Figure 4.2). The temporal resolution of the Sentinel 1 dataset increased from 12 days until October 2016 to 6 days after it, after the launch (April 2016) and starting of operational phase of Sentinel 1B (Figure 4.3).
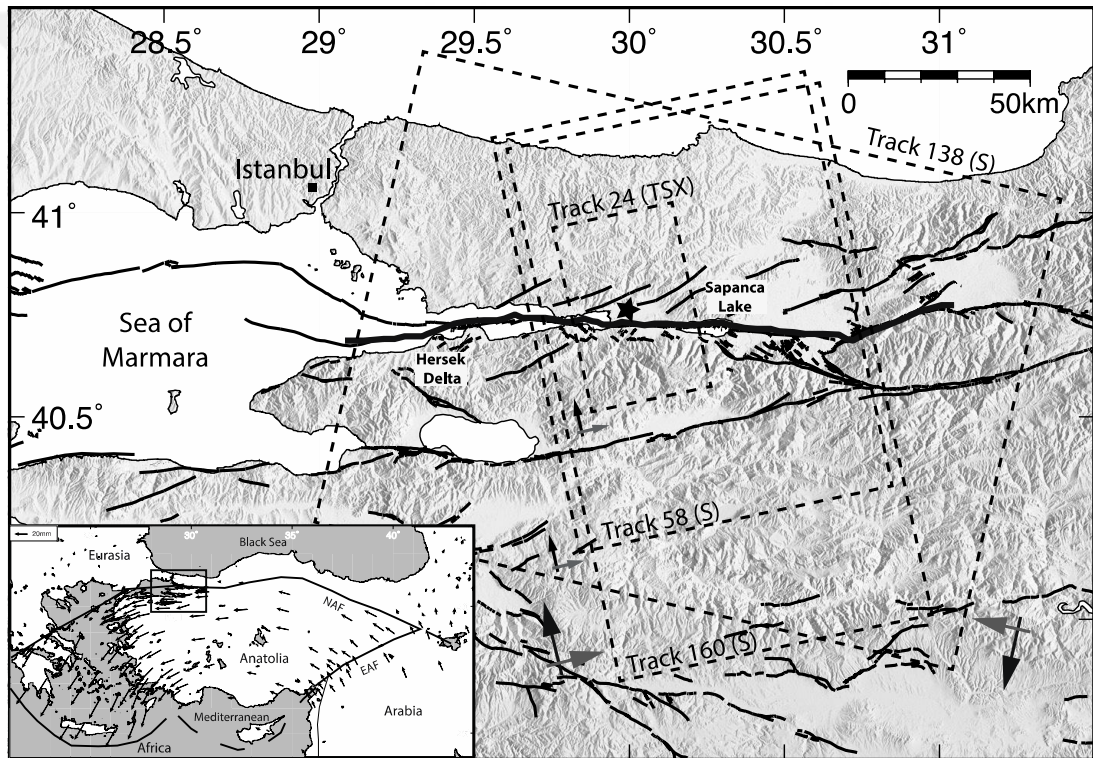
Figure 4.2 : Tectonic setting and InSAR data coverage. Inset map shows relative plate motions, with GPS vectors in an Eurasia fixed reference frame (Reilinger et al., 2006). The study area along the North Anatolian Fault is indicated with a black rectangle. Dashed rectangles in main figure outline the location of processed radar images, with track numbers indicated (S: Sentinel 1A/B, TSX: TerraSAR-X). Gray and black arrows show line-of-sight and flight directions of the satellites, respectively. Shaded topography is from Shuttle Radar Topography Mission. The 17 August 1999 Izmit surface rupture trace (Barka et al., 2002) and other active faults (Emre et al, 2013) are drawn with bold **black** and thin black lines, respectively. The black star indicates the epicenter of the Izmit earthquake.

Table 4.1 : Characteristics of each processed track.

Track	Sensor	Geometry	Time Interval	Interferograms Used
T24	TerraSAR-X	Ascending	2011-2015	31
T58	Sentinel	Ascending	2014-2017	100
T160	Sentinel	Ascending	2014-2017	88
T138	Sentinel	Descending	2014-2017	84
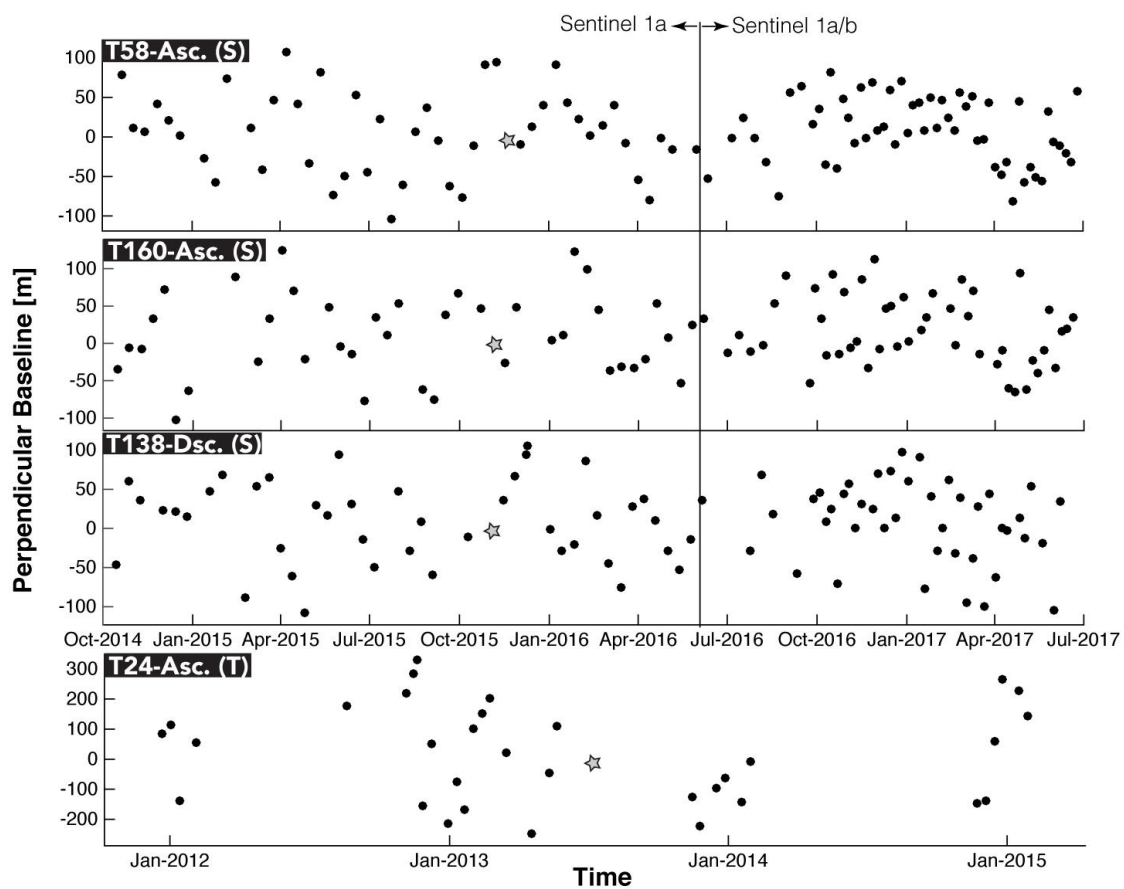
Figure 4.3 : Plot of baseline versus time of synthetic aperture radar (SAR) images for different tracks and satellites (S: Sentinel-1, T: TerraSAR-X), used to compute displacement fields and time series. Black dots indicate SAR images and gray stars indicate the master image chosen for time series analyses.

4.3.2 PS-InSAR Processing

TerraSAR-X (TSX) interferograms were constructed using the DORIS software developed by The Delft Institute of Earth Observation and Space Systems at Delft University of Technology (Kampes et al., 2005). Sentinel-1 interferograms were processed with GMTSAR software (Sandwell et al., 2011). In both cases, we used the Shuttle Radar Topography Mission (SRTM) 3-arcsecond (~90-m spatial resolution) digital elevation model for correcting topographic contributions to the radar phase. The choice of the master images for each track has been made so as to minimize the spatial and temporal baselines. For the sake of consistency between the three Sentinel-1 tracks, the master image is chosen in November 2015 for all tracks. For the TSX track, it is chosen in July 2014 (Figure 4.3).

Following interferogram processing, we used the Permanent Scatterers Interferometry Synthetic Aperture Radar (PS-InSAR) technique to compute the displacement time series of each stable Permanent Scatterer pixel (PS) in the study area, based on a single master network and the Stanford Method for Persistent Scatterers (StaMPS) (Hooper, 2008; Hooper et al., 2012). This PS-InSAR technique is an advanced method used to monitor surface deformation caused by tectonic or anthropogenic activities. It exploits the radar return signal reflected from persistent scatterers (phase-stable targets) such as rooftops, large rock outcrops, bridges, or motorways (Ferretti et al., 2001). It allows monitoring subtle and slow deformation signal, mitigating errors due to atmosphere, digital elevation model and orbital inaccuracies using spatial and temporal filtering. StaMPS uses both amplitude and phase information to identify PS points. In an initial step, the selection of PS points is performed based on their noise characteristics, using an amplitude analysis. The amplitude dispersion criterion is defined by : $D_{Amp} = (\sigma_{Amp}/m_{Amp})$ where σ_{Amp} and m_{Amp} are the standard and mean deviation of the amplitude in time, respectively (Ferretti et al., 2001). In the present study, we selected a threshold value of 0.42 for D_{Amp}, which minimizes the random amplitude variability and eliminates highly decorrelated pixels in some areas covered with vegetation, agricultural fields or snow. Once coherent PS points have been selected based on this amplitude analysis, the PS selection is refined by phase analysis in a series of iterations, which allows the detection of stable pixels even with low amplitude. The next steps of the StaMPS

processing include correction of the residual topographic component and 3D unwrapping of the PS phase both spatially and temporally.

Unwrapped interferograms after PS selection were corrected from stratified tropospheric delays using the freely available Toolbox for Reducing Atmospheric InSAR Noise (TRAIN, Bekaert et al., 2015), based on the ERA-Interim (ERA-I) global atmospheric model. Corrected interferograms were then used to compute mean velocity fields in StaMPS. The effect of such corrections is shown on the Figure S1 in the Supporting information.

Finally, we transformed the mean velocity fields of each track into an Eurasia-fixed GPS reference frame, following the procedure described by Hussain et al. (2016), using the GPS velocities around the 1999 Izmit rupture published by Reilinger et al. (2006). These GPS velocities are derived from pre-1999 earthquake observations (i.e. they do not include coseismic or postseismic deformation).

4.4 Results

4.4.1 Mean Line-of-Sight Velocity Fields

Figures 4.4 and 4.5 show the mean line-of-sight velocity fields calculated from PS-InSAR time series analysis along the Izmit earthquake rupture with negative velocities (cold colors) representing motion of the ground toward the satellite and positive velocities (warm colors) motion away from the satellite. The change of motion direction across the NAF is attested by the warm/cold color contrast across the fault. Considering the different geometries of data acquisition (i.e., ascending or descending), it is consistent with a right-lateral slip displacement on the fault, due to the westward movement of the Anatolian plate relative to the Eurasian plate.

All line-of-sight velocity maps show a very sharp velocity gradient along the central section of the Izmit rupture, in particular between the Izmit Bay and the Sapanca Lake (Figures 4.4, 4.5 and 4.6), which constitutes evidence for shallow creep (Bürgmann et al., 2002; Cakir et al., 2012). East of Sapanca Lake, the creep signal seems to disappear, which differs from previous InSAR results derived from other data sets spanning older periods (prior 2011) (e.g. Hussain et al. 2016). Negative velocities (cold colors) represent motion of the ground toward the satellite and positive velocities (warm colors) represent motion away from the satellite. Dashed-

line red boxes indicate the coverage of close-up views of average line-of-sight (LOS) velocity fields shown in Figure 4.6. Plain-line red boxes highlight the region selected for decomposing horizontal and vertical velocity fields along the fault in Figure 4.9 - a and 4.9-b. Black lines indicate active faults in the region (Emre et al., 2013).

The velocity gradient across the fault is sharp and similar in shape in all fault-perpendicular line-of-sight velocity profiles from different, independent tracks and viewing geometries (Figure 4.7). The sign difference for ascending and descending tracks is as expected, and related to the projection of the right-lateral motion on two opposite line-of-sights. The creep rate near the surface is proportional to the amount of the line-of-sight velocity offset across the fault measured on these fault-perpendicular profiles. The creep rates estimated for the three Sentinel tracks (T138, T58, T160) that span the same time period and TerraSAR-X track (T24) are consistent with each other and are around 5 mm/yr. In the next sections, we further explore the spatial variations of the creep rate along fault (sections 4.4.2 to 4.4.4) and its potential time evolution (section 4.6), through a time series analysis of surface deformation using all tracks.
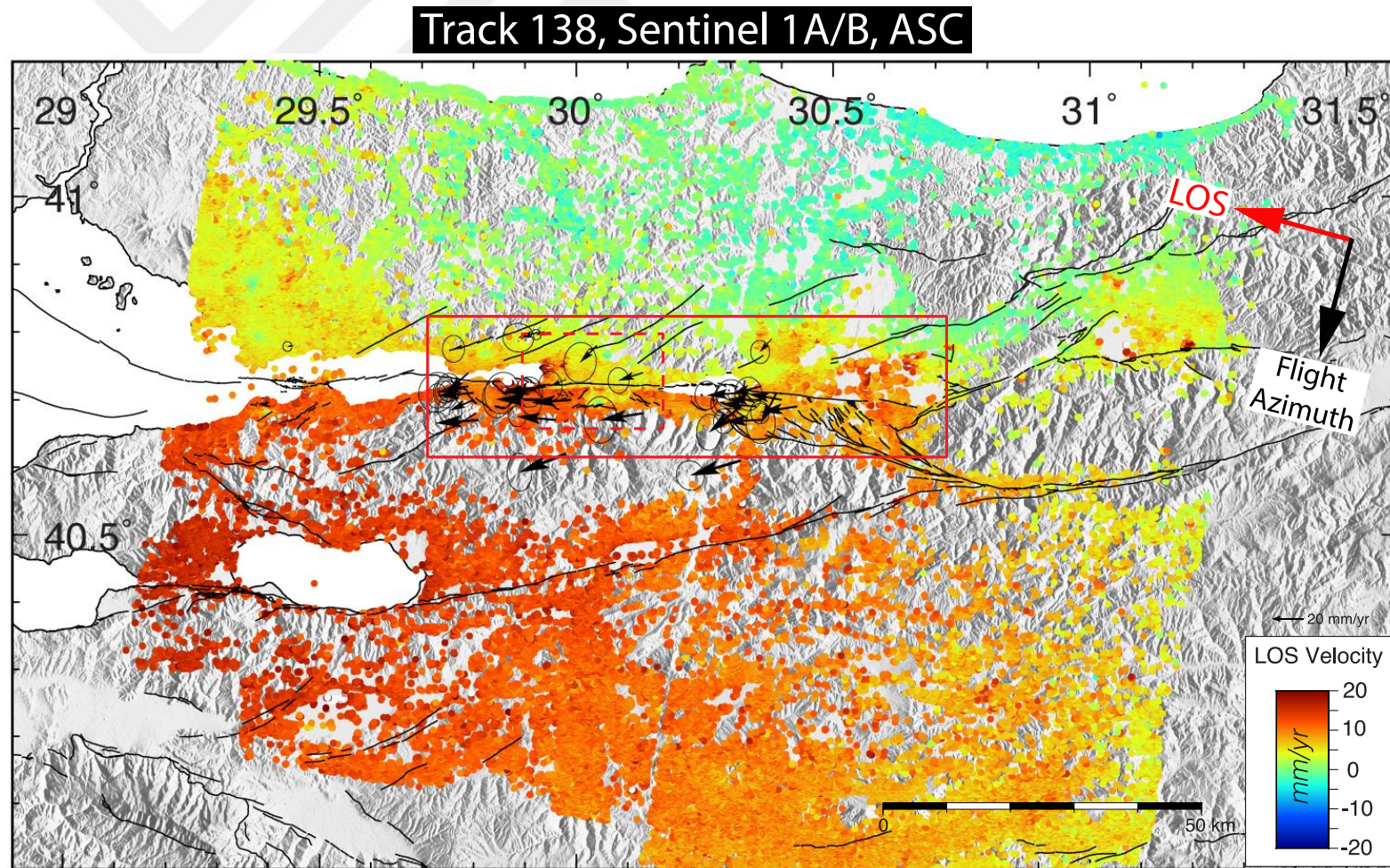
Figure 4.4 : Mean line-of-sight velocity fields for the period 2014–2017, from Sentinel 1A/B descending track 138 obtained from PS-InSAR time series analysis, and expressed in a Eurasia-fixed reference frame
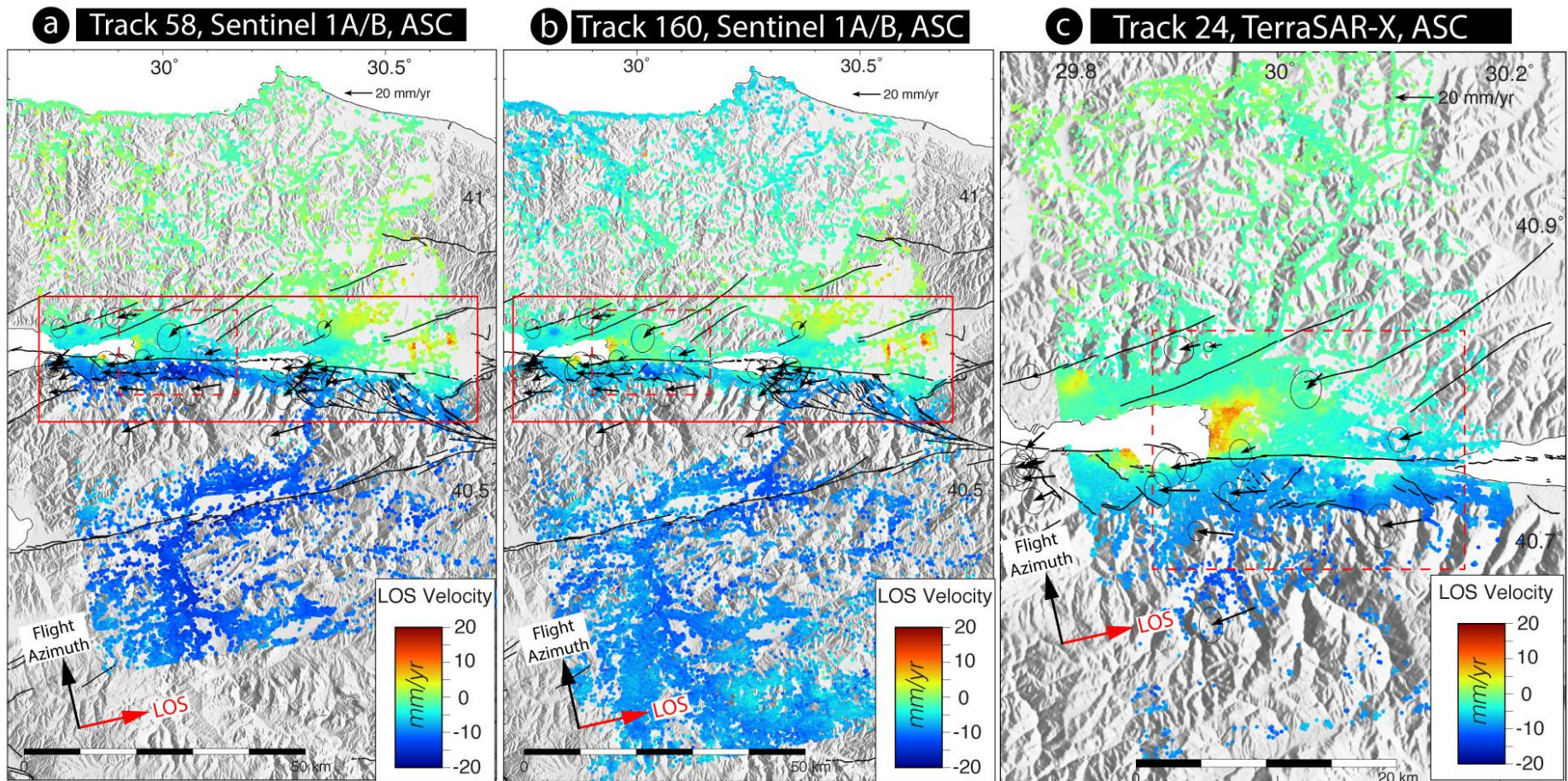
Figure 4.5 : Mean line-of-sight velocity fields for the period 2014–2017, from Sentinel 1A/B ascending tracks 58 (**a**) and 160 (**b**), and for the period 2011–2015 from TerraSAR-X ascending track 24 (**c**), obtained from PS-InSAR time series analysis, and expressed in a Eurasia-fixed reference frame.
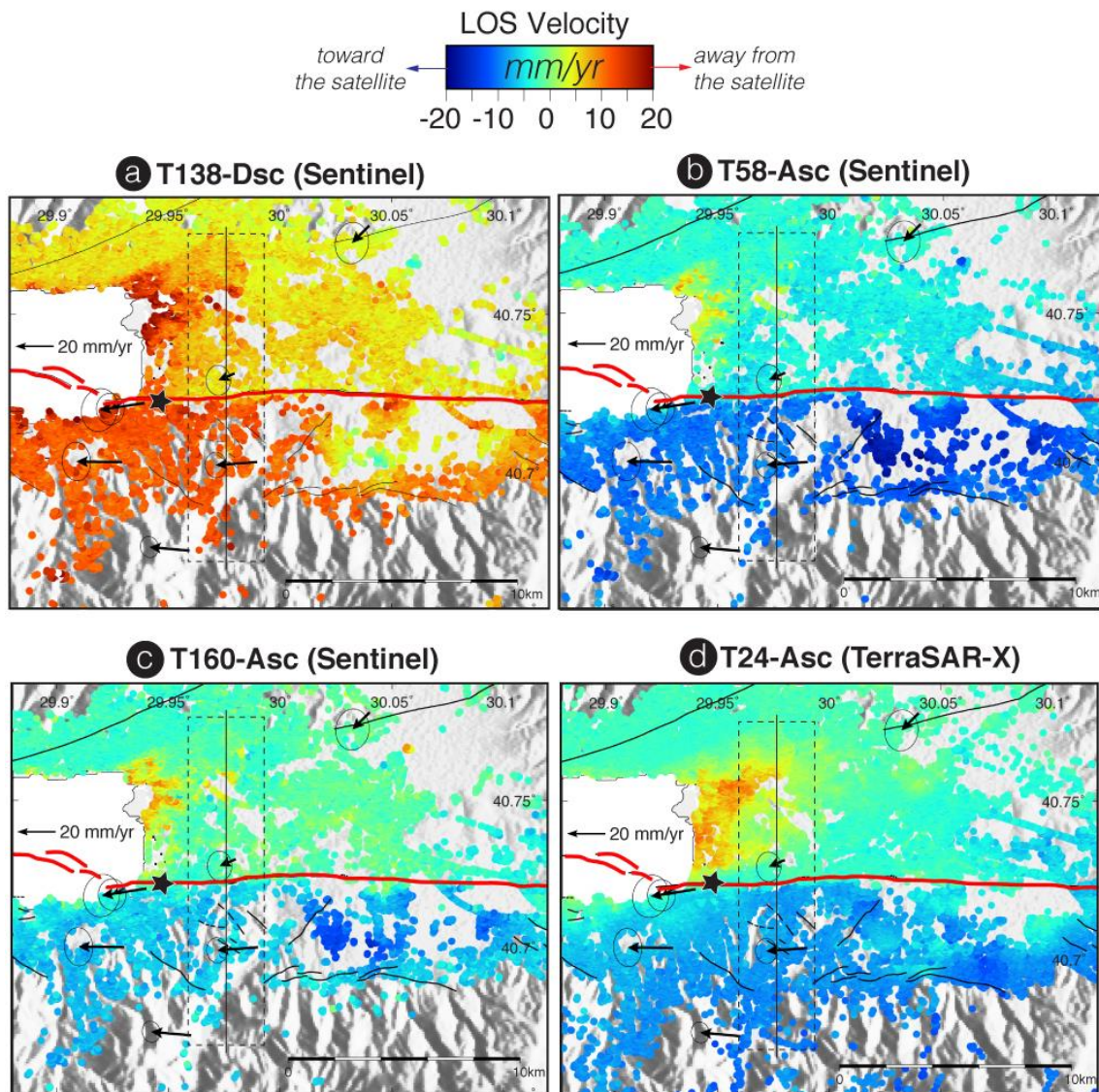
Figure 4.6 : Close-up views on average velocity fields on four different tracks (same tracks as in Figure 4.4) along the Izmit Bay-Sapanca Lake segment of the Izmit earthquake rupture. The sharp velocity jump observed along the fault is attributed to shallow creep. Red lines indicate 1999 Izmit rupture (Barka et al., 2002) and black lines indicate active faults (Emre et al., 2013). Boxes with dashed-lines contour data points selected to plot profile of Figure 4.7.
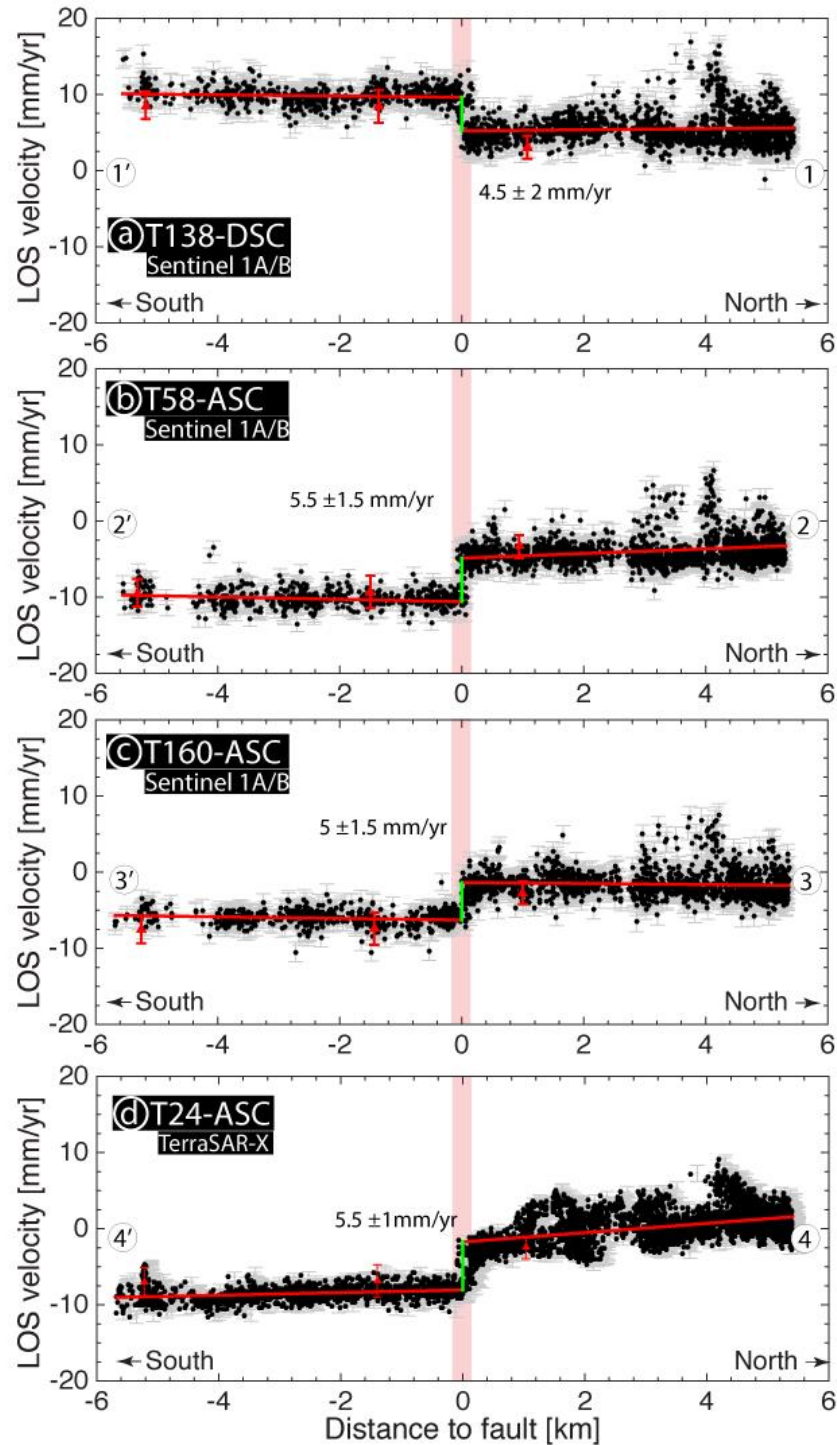
Figure 4.7 : Line-of-sight velocities from the four processed tracks along an unique north-south profile perpendicular to the 1999 fault rupture near Izmit (see dashed box in Figure 4.6 for the profile location). Black dots are PS-InSAR data points within the swath profile, projected onto its centerline. Gray error bars indicate 1σ variations across profile. Transparent red box indicates location of fault where PS points are not taken into account for calculation of best linear fit to the velocities (red lines). Jumps in the velocity profiles on the fault indicate surface creep rate (green lines).

4.4.2 Fault-parallel horizontal velocities versus vertical velocities

The InSAR technique measures projections of ground displacements only along the line-of-sight look angle. In order to retrieve the components of 3D deformation, InSAR line-of-sight displacement fields observed under different viewing directions (i.e. different satellite tracks) over the same ground location must be combined (Wright et al., 2004).

In order to analyze the spatial variations of horizontal creep rate along the fault, we inverted the line-of-sight velocity fields to retrieve the horizontal (parallel to the east-west fault strike) and vertical components using the formalism of Wright et al. (2004) (Figures 4.8 and 4.9, see also Figures S5 in the appendix C for the associated uncertainties). We neglected here the motion along the north-south direction, a reasonable assumption for a strike-slip fault, consistent with observations of surface displacement during and after the 1999 earthquake. Only the line-of-sight mean velocity fields calculated from Sentinel 1 A/B images, that cover the same time interval, were used. Initially we resampled the mean line-of-sight velocities for the ascending and descending tracks onto a similar grid (with a 200-m pixel spacing) using a nearest neighbor procedure. Subsequently we selected pixels existing in all three velocity maps from ascending and descending tracks. Finally the inversion was carried out for these pixels, taking into account the local incidence angle of the satellite view.

The discontinuity observed in line-of-sight velocity fields along the North Anatolian Fault is now much better pronounced in the east-west horizontal velocity field, especially along the Izmit section of the fault, between Izmit Bay and Sapanca Lake (Figures 4.8 and 4.9-a). This sharp discontinuity disappears in the east of Sapanca Lake. We note a slight velocity gradient also along the Iznik fault ~40 km south of the main North Anatolian Fault (Figure 4.8). The vertical component (Figure 4.9-b) does not show any prominent discontinuity across the fault, which implies that aseismic slip is mostly purely horizontal. Variations in the vertical velocity field are seen at some places around the fault with various spatial patterns and rates, particularly in the Adapazari basin, as reported previously by Cakir et al. (2012) and Hussain et al. (2016) for the period between 2002 and 2010 (section 4.4.4).
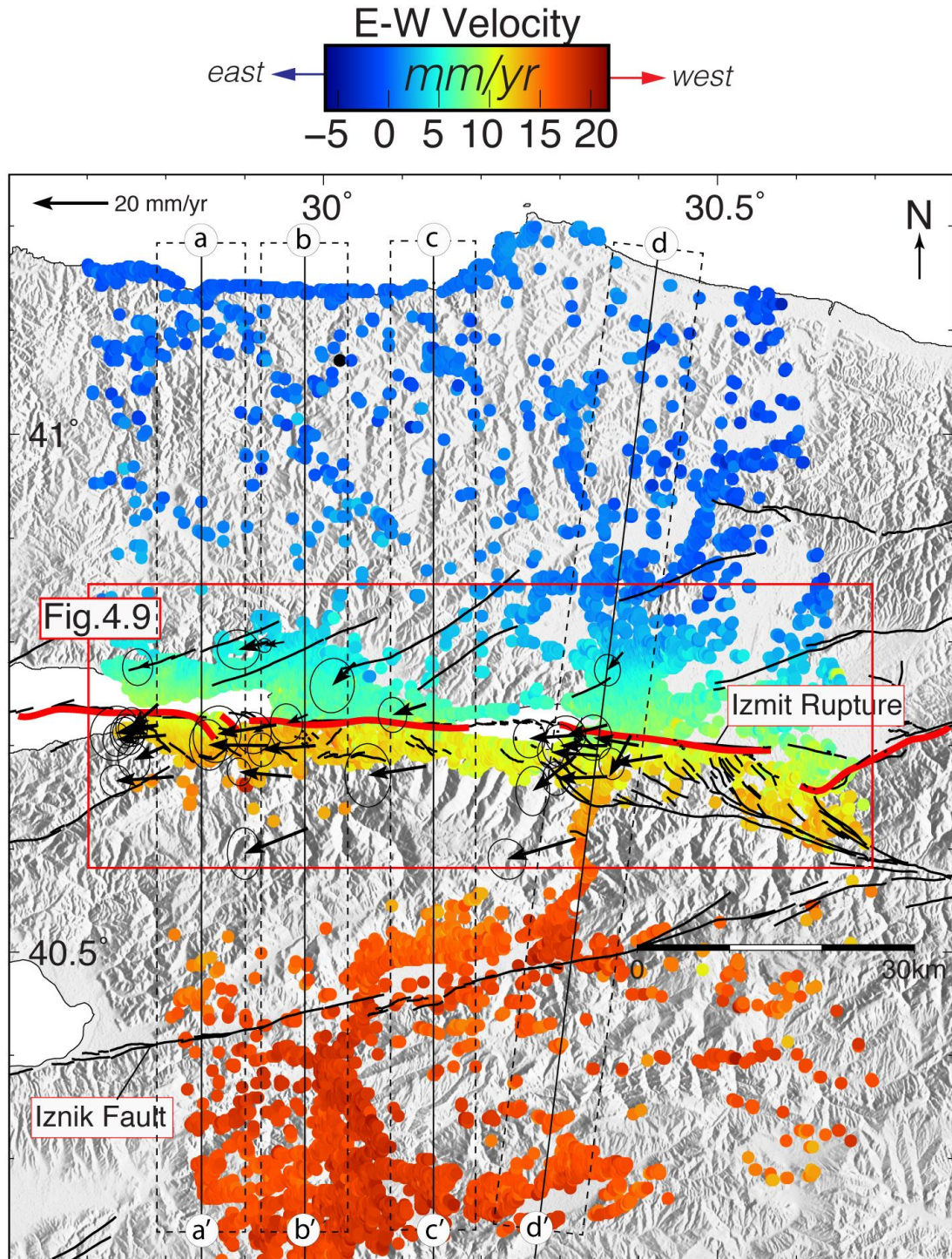
Figure 4.8 : Fault-parallel, horizontal velocity field inverted from line-of-sight velocity fields of all Sentinel satellite tracks used in this study (2014-2017). Black lines are mapped active faults in the region from Emre et al, (2013). Red lines indicate the 1999 Izmit rupture. Lines labeled A-A', B-B', C-C'and D-D' show locations of profiles of Figure 4.11.
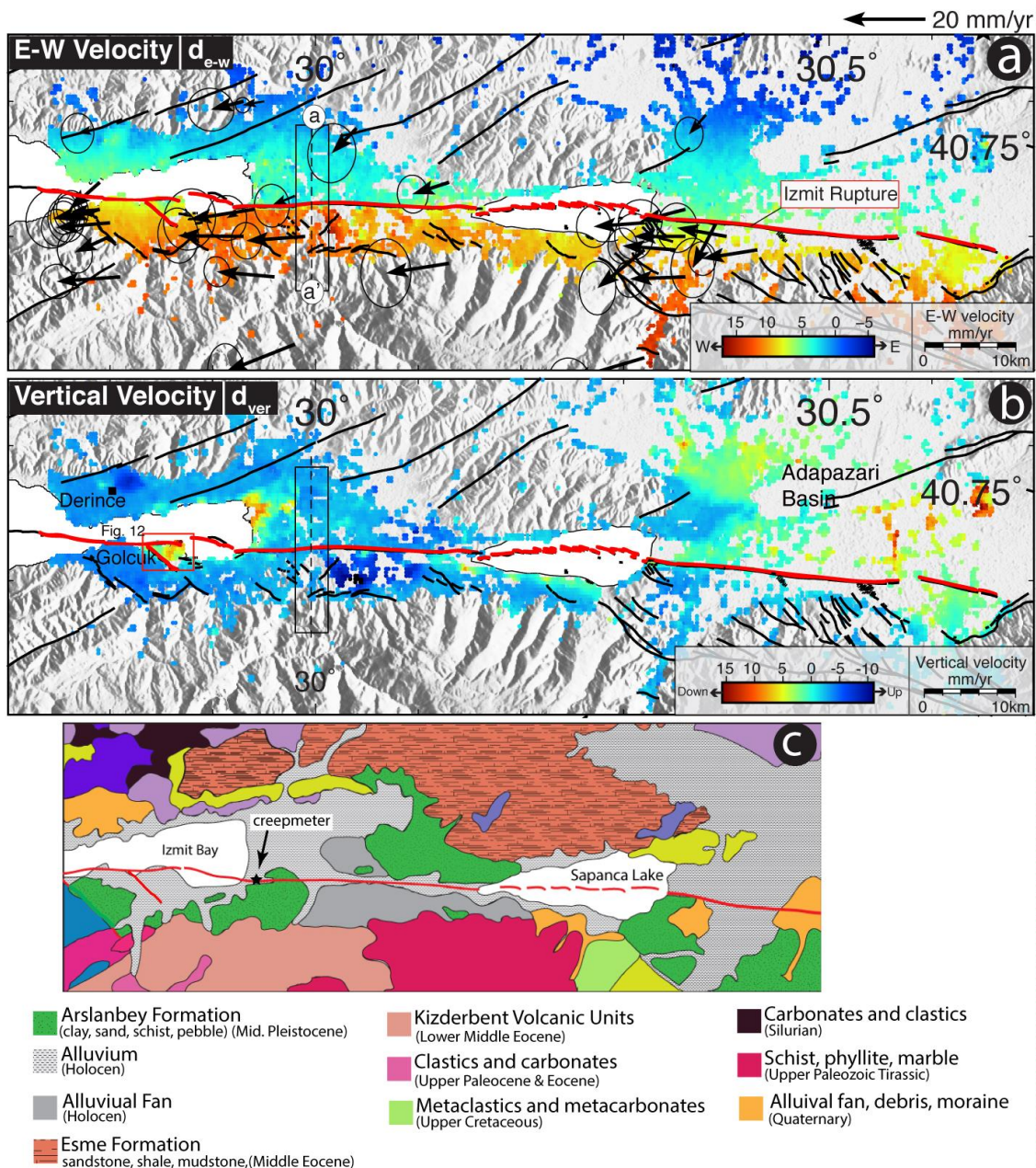
Figure 4.9 : Enlarged view of the Izmit creeping section of the North Anatolian Fault. Fault-parallel, horizontal (**a**) and vertical (**b**) velocity fields inverted from line-of-sight velocity fields of Sentinel satellite tracks used in this study (2014-2017). A sharp discontinuity observed along the 1999 Izmit rupture reveals shallow creep between the Sapanca Lake to the east and the Gulf of Izmit to the west. The black rectangle with dashed line labeled a-a' in east-west velocity field indicates the location of the profile shown in Figure 4.10-a. It is superimposed as well on vertical velocity field in (b) in order to highlight the continuity of the vertical velocity across fault. The red box indicates location of maps shown in Figure 13. (**c**) Geological map of the study region simplified from MTA – Turkey General Directorate of Mineral Research and Exploitation 1/500000 scale geologic map.

4.4.3 Horizontal Creep Rate Distribution Along Fault

The E-W horizontal velocity field can be used to analyze the along strike variations of the creep. We first use a similar approach as Kaneko et al. (2013). We plot a series of 8 km-long, 2 km-wide velocity profiles perpendicular to the fault, every 7 km along strike (Figure 4.9, showing one example of profile -aa'-, and Figure 4.10). Velocities on both sides of the fault are fitted by a linear trend and the offset across fault between these best-fit lines is measured, corresponding to the creep rate (Figure 4.10-a). Figure 4.10-c shows strong variations of this creep rate along fault. These variations are at first order consistent with the results from Hussain et al. (2016), with a maximum creep rate at the same location, south of Izmit, and an eastward decrease of the creep rate from the Izmit Bay to the east of Sapanca Lake. However, the maximum creep rate appears to have decreased from ~10 mm/yr during the 2002-2010 period covered by their Envisat data to ~8 mm/yr for the 2014-2017 period covered by our Sentinel-1 data. This is expected due to the temporal decay of the creep rate since the Izmit earthquake (Cakir et al., 2012).

4.4.4 Vertical Motion Along the 1999 Rupture

The vertical velocity field shows various anomalies along and near the Izmit rupture zone (Figure 4.8b). While local subsidence and uplifts areas with varying spatial extent and rate are observed in the vicinity of the fault, vertical motion localized on the fault zone is observed only in the Golcuk pull apart basin bounded to the south by an oblique normal fault, on which 2.5 meters of vertical offset was observed during the 1999 Izmit earthquake (Barka et al, 2002). The subsidence with a rate of the order of 10 mm/yr in Gölcük is bounded by this normal fault. Figure 12 shows the highest spatial resolution of the line-of-sight velocity across the fault from the TerraSAR-X dataset, highlighting a high gradient at the fault location. Such a sharp gradient across fault may be indicative of creep at shallow depth. However, without any complementary data or modelling (out of scope of this paper), we cannot exclude that the subsidence is related to compaction of unconsolidated sediments in the basin or water pumping.

Another distinctive feature in the vertical velocity field for the studied period 2011-2017 is the pattern of localized subsidence in the city of Izmit. This subsidence was first reported by Cakir et al. (2012) using InSAR analysis of Envisat images between

2003 and 2009. It likely results from urbanization along the northeastern boundary of the Izmit basin.
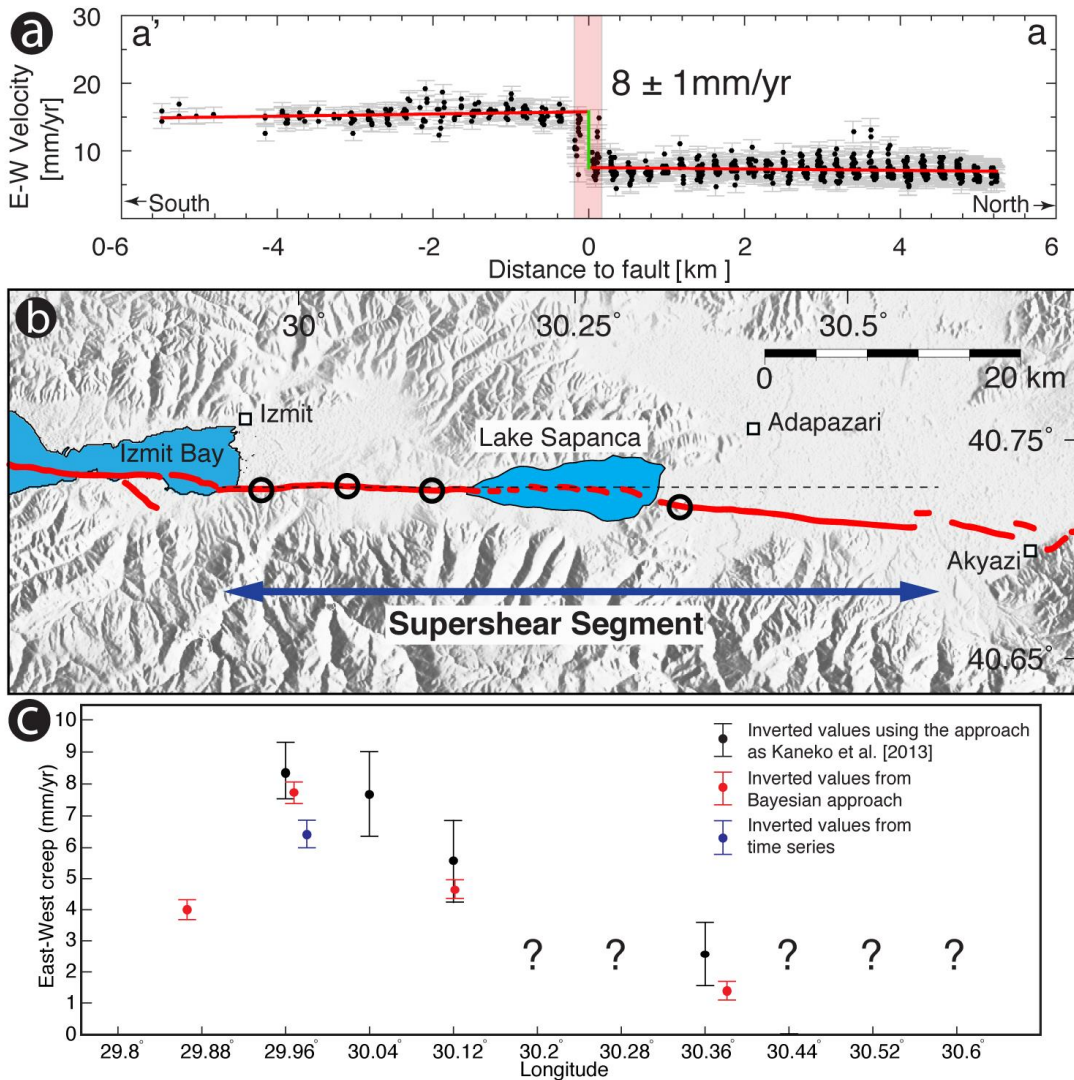
Figure 4.10 : (**a**) Measuring horizontal creep rate along a fault-perpendicular velocity profile (profile a-a' in Figure 4.9). Black dots are E-W PS velocities within the box projected onto profile centerline, with 1σ uncertainties shown by gray error bars (from data inversion, see text for details). Red straight lines correspond to best fit to the data on both sides of the fault (with data within a 200-m distance to the fault, marked with transparent red box are ignored). The creep rate is the vertical distance (green line) between the two red lines on the profile. (**b**) Map of the 1999 Izmit rupture with (**c**) variations of horizontal creep rate along fault, estimated as in (a), inverted using a Bayesian approach or inverted from time-series analysis (black, red, blue dots and error bars, respectively). Positive creep values in east-west direction indicate right-lateral motion.

As reported by Hussain et al. (2016) using Envisat ASAR images acquired between 2002 and 2012, the Adapazari basin, a deep sedimentary basin, is subsiding at a rate of ~6 mm/yr. The most devastating effects of liquefaction were observed in this basin during the 17 August 1999 Izmit earthquake (Bol et al., 2010). A clear velocity gradient is observed west of the Adapazari, most likely marking a passive boundary between competent bedrock in the north on Sapanca Lake and Holocene loose fluvial, palustrine and lacustrine deposits in the Adapazari depression (no active fault is known at this boundary). Finally, an area of uplift, with an uplift rate of ~6mm/yr, is observed in the Derince neighborhood in the province of Kocaeli northwest of the Izmit bay (Figure 4.8b), as reported previously by Cakir et al. (2012).
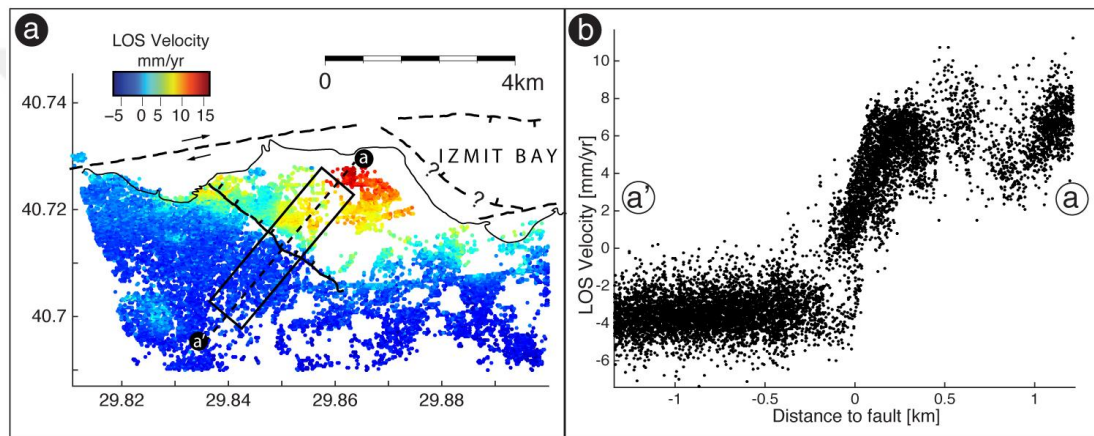
Figure 4.11 : (**a**) Close-up view of line-of-sight velocities across the Golcuk normal fault calculated from TerraSAR-X ascending track 24 for the period of 2011-2015. Fault location is indicated by black solid line inland and dashed lines offshore, inferred from fault geometry inland and bathymetry and shallow seismic profiles in the Sea of Marmara (Barka et al., 2002) (**b**). Line-of-sight velocity profile along profile a-a'shown in (a).

4.5 Modelling Profile Velocities

To further investigate the variations of the creep characteristics along fault (horizontal rate and depth), together with the tectonic loading (far-field loading rate and locking depth of the fault), we invert 80 km-long fault-perpendicular horizontal velocity profiles (Figures 4.8 and 4.12), chosen to represent the along-strike variability of the creep seen in Figure 10. We use a Bayesian sampling algorithm, which allows uncertainties on model parameters and trade-offs between these parameters to be quantified (Figures 4.8 and 4.13). The shape of the velocity profiles (Figure 11) confirms the existence of two different deformation signals: 1) the long-

wavelength arctangent shape associated with the interseismic tectonic strain accumulation, and 2) a sharp step at the fault (visible only between the Izmit Bay and Sapanca Lake), due to surface creep. The interseismic slip rate V is modeled using a screw dislocation at a depth D_1 in elastic half-space (Savage & Burford, 1973). The creep, from surface to depth D_2, with a rate C, is modeled using the back-slip approach proposed by Savage (1983), as a combination of slip along the entire fault plane and a screw dislocation at depth D_2 in reverse sense to the plate motion. In this configuration, creep occurs from the surface down to a shallow depth D_2 only and the fault is fully locked between depths D_1 and D_2. The total horizontal slip rate $\upsilon(x)$ derived from InSAR can thus be expressed as:

$$\upsilon(x) = \frac{V}{\pi} \arctan\left(\frac{x}{D_1}\right) + C\left[\frac{1}{\pi} \arctan\left(\frac{x}{D_2}\right) - \mathcal{H}(x)\right] + a, \qquad \textbf{(4.1)}$$

where x is the distance (km) along a direction perpendicular to the fault, and a is a constant velocity of adjustment between measured velocities and model.

We use the Bayesian algorithm of Goodman and Weare (2010) with a Markov Chain Monte Carlo (MCMC) sampler (Foreman-Mackey et al., 2013) to explore the model parameter space (V, D_1, C, D_2, a) and their full uncertainties. We use Gaussian prior distributions on the locking depth, centered on D_1 = 12 km (depth of seismogenic zone) with a 1σ value of 5 km (Ozalaybey et al., 2002), and on the tectonic slip rate, centered on V = 25 mm/yr (e.g. Cakir et al. (2012), Ergintav et al. (2014)) with a 1σ value of 7 mm/yr. An important additional constraint we impose here is that the maximum depth of the fault creep must be less than the locking depth, i.e. $D_2 \leq D_1$ as in Hussain et al. (2016). We assume a uniform prior probability distribution for C, D_2 and a within the bounds 0<C<8 mm/yr, 0<D_2<20 km, -20<a<20 mm/yr. For each model parameters or combination of parameters, we obtain posteriori probability density functions to analyze uncertainties and covariances and choose the mean of posteriori solution as the most representative one, close to the maximum solution as posteriori probability density functions are mostly Gaussian (Figure 4.13).

The results of the parameters inversion are shown on Figure 11. Figure 12 shows a posteriori probability density functions for estimated parameters on profile b-b' as an example (with high mean values and low two-sigma values, as for all profiles (see supporting information for profiles a-a', c-c' and d-d'-). The most prominent velocity step i.e. the maximum creep rate (7±0.5 mm/yr) is observed on this profile b-b' and

is consistent, within error bars, with the velocity surface offset measured directly from a short-length profile (Figure 4.10c). Consistently as well, profile c-c' show a creep rate lower than for profile b-b'. No significant horizontal creep is required by the models for the profile d-d'. This confirms that different segments of the Izmit rupture have presently different slip behaviors. Trade-offs exist between some parameters, as expected, especially between the rates and the depths, while the creep velocity and the tectonic loading rate appear uncorrelated (Figure 4.13). Mean solutions for the creeping depth vary around the value of 5.5 km (Figure 4.12e), consistent with previous studies (Cakir et al., 2012; Hussain et al, 2016) for the central segment of the rupture.
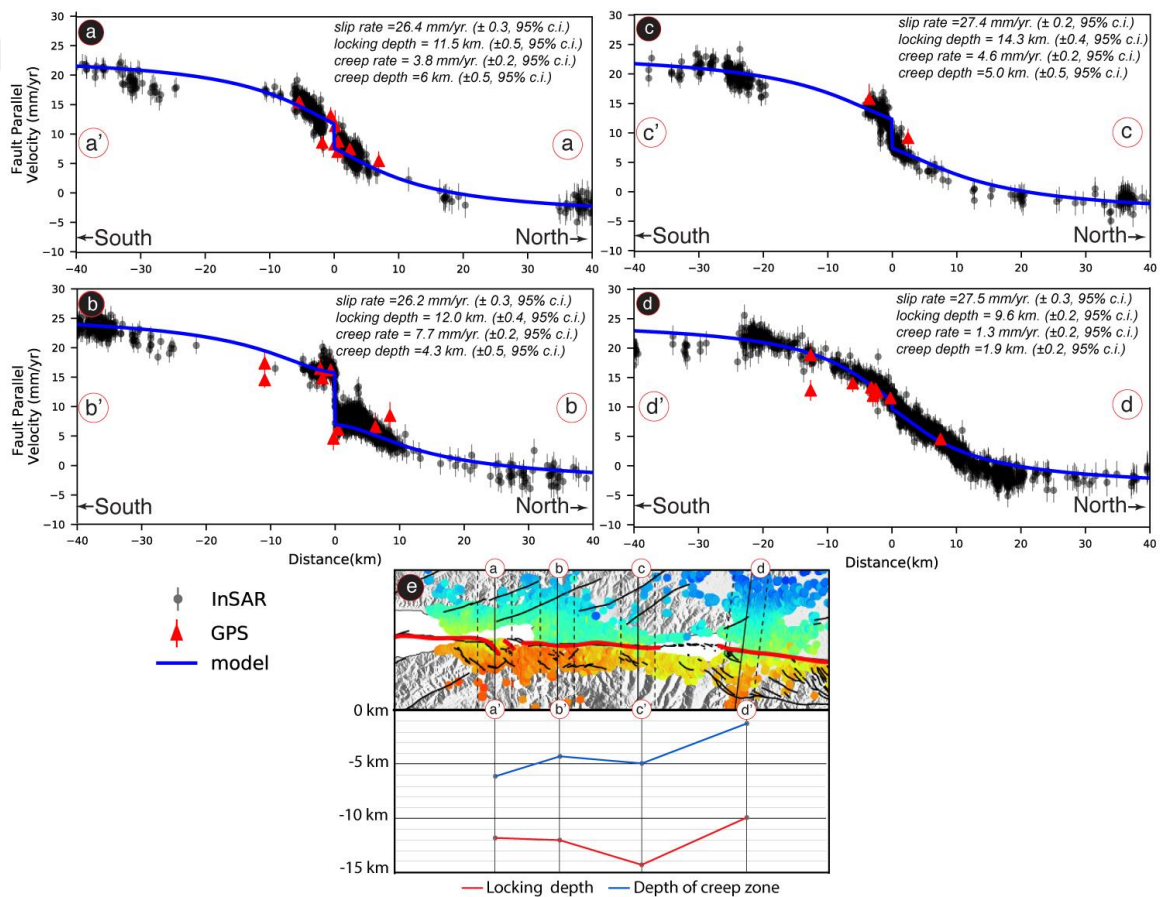
Figure 4.12 : Observed and modeled horizontal velocity profiles (**a** to **d**). Profiles are perpendicular to the fault and are shown on Figure 4.8. Blue curves show the mean solution of the interseismic model with shallow creep, from the Bayesian inversion, with corresponding parameters and one-sigma value given above each curve. Black arrows point to the location of the mapped active fault. (**e**) Map view of profiles in a to d in the near-field with spatial variations of locking depth and creep depth estimated for each profile.
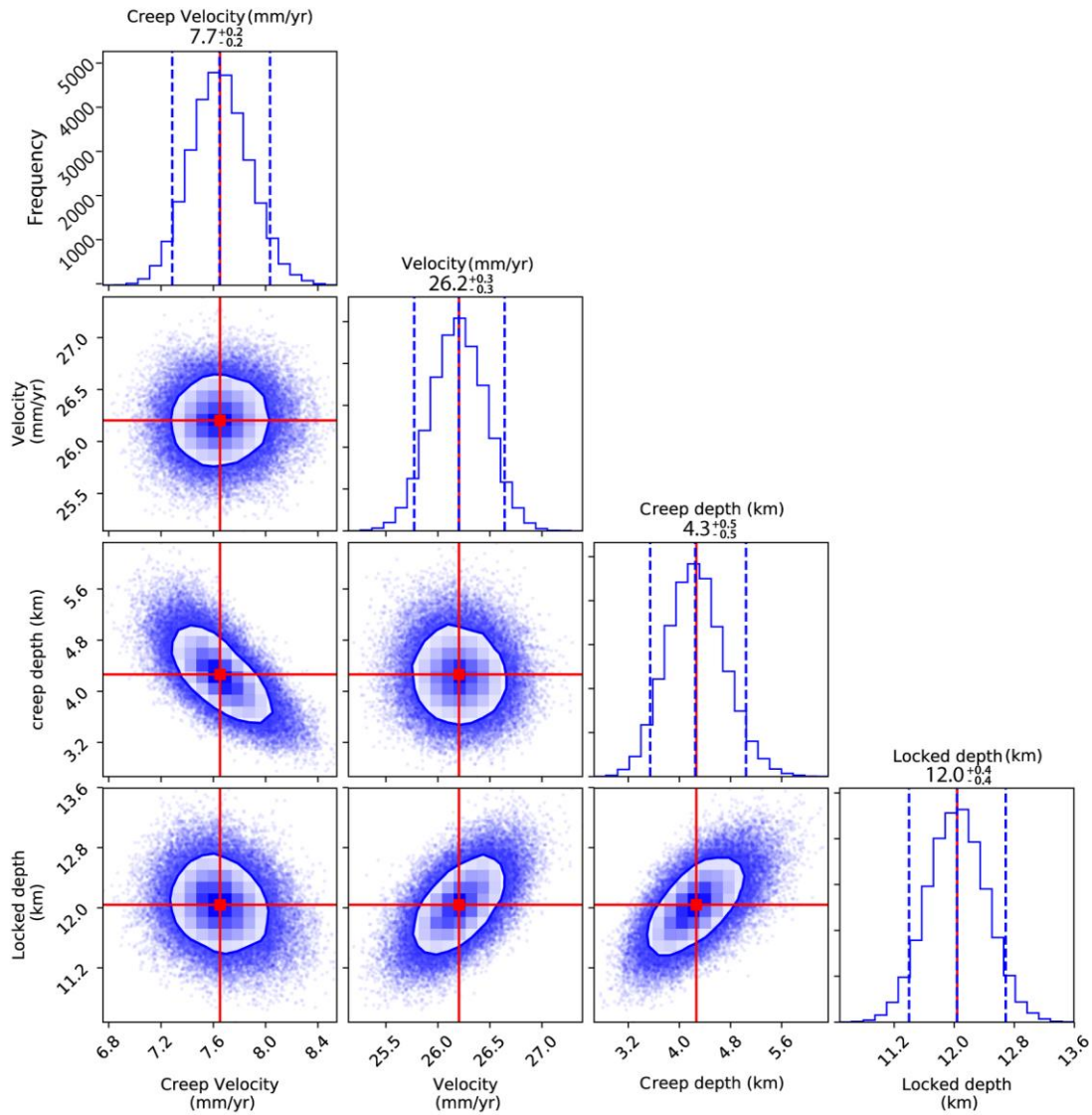
Figure 4.13 : One-dimensional and two-dimensional sampled probability distributions obtained from Monte Carlo Markov Chain exploration of the model parameters assuming a priori uniform distribution for all model parameters but locking depth D_1 (Gaussian distribution), for profile b-b'. The diagonal plots display the one-dimensional marginal distribution for each parameter independently in the histograms. The panels with clouds of points display the marginal two-dimensional distributions. The red solid lines indicate the mean value for each model parameter. Blue dashed lines mark the 95% confidence interval of the probability density functions. The values above each histogram indicate the mean value.

4.6 Temporal Evolution of Creep

In order to identify potential temporal variations of the creep rate, we performed a time series analysis of the surface displacement using all Sentinel 1A/B data. For each Sentinel track independently, we computed the temporal evolution of the fault perpendicular line-of-sight displacement profile shown on Figure 4.6 and at each time step of the time series, we computed the line-of-sight displacement offset at the fault (corresponding to surface creep projected in line-of-sight), using the Kaneko et al., (2013) approach as in section 4.4.1. These displacement offsets were then converted into horizontal creep, assuming pure horizontal motion, as justified by the results shown in Figure 4.10, and no motion along the north-south direction (i.e. pure fault-parallel horizontal motion).

Figure 4.13 shows the derived temporal evolutions of this surface creep for all three independent Sentinel tracks, and the creep rates appear remarkably consistent. The mean creep rate is 6.5 ± 0.5 mm/yr, which is in a good agreement with the average creep rate of $\sim 7 \pm 0.5$ mm/yr estimated from the analyses presented Figures 4.9 and 11. In order to minimize noise and explore creep rate variations, the obtained displacements (green, orange and magenta points on Figure 4.14a) were averaged using 2-month bins (blue dots on Figure 4.14a show the average value with the corresponding one standard deviation within the bin). This reveals a transient creep event in the time series around December 2016 that lasted for less than one month. A linear inversion of the creep rate, done separately for the periods before and after this month, allows estimating 1) an amplitude of ~ 10 mm for this transient creep event, which is equivalent to 1.5 years of steady creep at the mean rate of ~ 7 mm/yr, and 2) its approximate duration of three weeks.

To test the statistical validity of this creep event detection from noisy InSAR time series, we computed the Akaike Information Criterion (AIC, Akaike, 1974), as currently done for the analysis of GPS time series (e.g. Nishimura et al., 2013). The AIC is computed first for each time series independently, for a model of linear velocity and a model with a transient in addition. The AIC difference between the two models (ΔAIC) is indicative of the most robust model (Figure 4.14c, with a positive difference ΔAIC when the transient model is favored). We then sum up the ΔAIC of the three independent time series (Figure 14d).
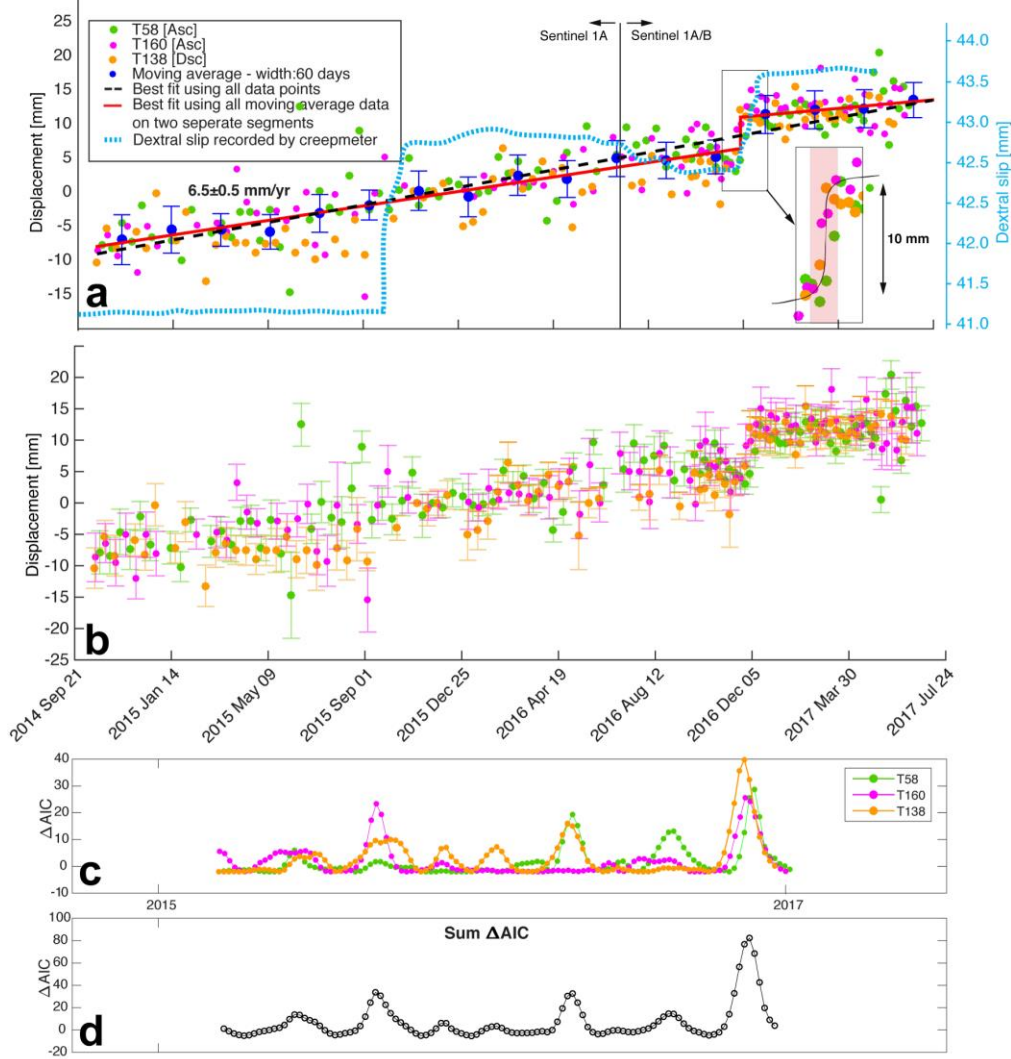
Figure 4.14 : Time series of horizontal creep estimated along a fault perpendicular profile (see location of the profile in Figure 5) using all Sentinel data sets and assuming pure horizontal motion parallel to the fault. (**a**) Blue dots are the binned averages every 60 days. Error bars show one standard deviation of the distribution of the points within each bin. A clear transient event is seen around December 2016 (see inset). Red lines are fitted to the two separate segments of the bin-averaged data before and after this month. The vertical red line shows the transient creep event amplitude calculated from the offset of the two red lines. Black dashed line is the best fitting line for the entire data set points that represent the mean rate (~6.5 mm/yr). The period of transient creep, from mid-November to mid-December 2016, is highlighted by the transparent red background in the inset. Blue dashed line shows surface slip measured by the creep meter for comparison. (**b**) Raw data showing estimated creep displacement with error bars that indicate two sigma standard deviation of the measurements. (**c**) Difference of AIC (Akaike Information Criterion) between linear creep rate models with and without a transient, computed for each track independently. ΔAIC is positive when the transient model is preferred. (**d**) Summation of all three ΔAIC, highlighting one major creep burst.

48

The one-month transient creep event of December 2016 discussed above has the highest ΔAIC for all three tracks, thus for the summed ΔAIC. Two other minor peaks of ΔAIC may also correspond to other transients during the earlier period, only sampled every 12 days.

We also compared the temporal trend of the InSAR time series with that of a creep meter installed near the epicenter of the Izmit earthquake (see location on Figure 2). This creep meter recorded two transient creep events in September 2015, with ~2.5 mm of slip, and in December 2016, with ~1 mm of slip (Figure 4.14a). We note the temporal correlation with two of the transients detected by InSAR, although slip amplitudes measured by the creep meter are up to ten times slower than the slip amount (10 mm) estimated using InSAR time series. Such slip discrepancy is likely suggesting that the creep meter underestimates the creep as it encompasses a small fraction (about 10 m) of the fault zone.

4.7 Discussion

Our results derived from a PS-InSAR analysis using high-resolution multi-sensor SAR images and GPS campaign measurements along the 1999 Izmit rupture reveal that the fault section with supershear velocities during the earthquake, between the Izmit Bay and Sapanca Lake (Bouchon et al., 2001), is still creeping 19 years after the earthquake. The average creep rate during the 2014-2017 Sentinel-1 period reaches up to ~8 mm/yr south of Izmit, a maximum value about half than that reported after the Izmit earthquake and during the 2002-2010 Envisat period (Cakir et al., 2012; Hussain et al., 2016). We discuss below the potential factors controlling this long-lasting creep and its along-strike variations, as well as the mechanical implications of the one-month creep burst detected during the 3-year period covered by Sentinel-1 data.

4.7.1 Spatial Distribution of Creep and Geometrical and Lithological Control

Supershear velocity ruptures, as the 1999 Izmit earthquake, have mostly been observed along major strike-slip faults with overall simple planar geometries (e.g. Bouchon et al. 2010, Michel and Avouac, 2002), but with local geometrical complexities, stress or/and frictional heterogeneities along faults that can favor the transition to supershear velocities (Liu and Lapusta 2008). The spatial coincidence

between the presently creeping and the 1999 supershear velocity segments of the North Anatolian Fault may suggest similar controlling factors for these two phenomena. A possible influence of fault geometry at all scales on creep has previously been suggested (Jolivet et al., 2015b). The very linear geometry of the Izmit-Sapanca Lake and Sapanca Lake-Akyazi segments may promote creep, with fault steps and jogs at these segments extremities controlling the creep lateral extent and first-order segmentation (Figure 10).

Several mechanisms of creep have been proposed that also correlate the existence of creep with the nature of the rocks in the fault zone (Moore and Rymer, 2007; Moore and Lockner, 2013). Along the Ismetpasa creeping section of the North Anatolian Fault, Kaduri et al. (2017, 2018) showed the important role of lithology and mineral transformation in the fault zone on frictional properties along fault, therefore on creep distribution along fault. The clay gouges associated with the aseismic slip on this fault section (Figure 4.9c) are rich in weak minerals, such as saponite and other smectites (Kaduri et al., 2017). These low friction minerals have been observed as well along the creeping segments of the San Andreas Fault in California, and the Long Valley Fault in Taiwan (Moore & Rymer, 2007, Thomas et al., 2014). Along the Izmit creeping section, similar detailed analysis of rocks compositions in the fault zone remain to be done. However, geological maps reveal that the central section of the 1999 Izmit rupture coinciding with the maximum surface creep puts in contact Quaternary alluvial deposits in the central depression of the Izmit basin, north of the fault, and Eocene volcanic units south of the fault (Figure 9c). The weathering of these lenses of volcanic rocks could produce weak minerals such as saponite, favoring the persistency of high creep rate in this location (Kaduri et al., 2017). These volcanic units become thinner to the east of Sapanca Lake, which could explain why creep is vanishing eastward.

4.7.2 High Temporal Resolution InSAR Data Reveal Burst-Like Behavior of Creep

The high temporal resolution provided by the Sentinel-1 data set reveals the existence of at least one burst of creep at the end of 2016, with a good temporal correlation with a transient slip event detected by a creep meter located nearby. Such type of transient creep event had previously been reported along the Ismetpasa

creeping section to the east, based on the analysis of short repeat time SAR acquisitions from the COSMO-SkyMed constellation, over a limited one year period (Rousset et al., 2016). The maximum amplitude (~10 mm in our case, whereas it was ~20 mm along the Ismetpasa section) and duration of these shallow bursts (~1 month) are similar. The growing number of evidence for such creep bursts along the North Anatolian Fault, as also suggested by long time series of creepmeter measurements (Altay & Sav, 1991, Bilham et al., 2016), and along other major strike-slip faults worldwide (DeMichele et al., 2011; Jolivet et al., 2015a; Pousse-Beltran et al., 2016; Khoshmanesh & Shirzaei, 2018), suggest that continuously decaying afterslip or steady interseismic creep may not be the rule for creep behavior. New mechanical models are required to account for coupling temporal variations at shallow depth and recurrent creep bursts triggering. Long and temporally dense sets of InSAR data will be a key to constrain these models and further investigate the magnitude, depth, return period and dynamics of such transient creep episodes, as well as their contribution to tectonic strain release.

4.8 Conclusion

We have studied the spatiotemporal evolution of surface displacements along the central section of the 1999 Izmit earthquake with an unprecedented temporal resolution, using 307 SAR images acquired between 2011 and 2017, combined with GPS campaign measurements acquired every six months from 2014 to 2016. The joint analysis of GPS data and all SAR images acquired from multi-viewing geometries and multi-sensors, through a PS-InSAR data analysis, allowed to extract both horizontal and vertical motion along the fault and relevant slip parameters on fault.Subsidence in the Adapazari basin is still observed, at a rate of ~6 mm/yr, as previously reported by Hussain et al. (2016) using Envisat ASAR images. Other localized subsidence and uplift areas are identified around the Izmit Bay area. A prominent subsidence is observed for the first time on the hanging wall of the Golcuk normal fault, which marks the southwestern boundary of a releasing stepover along the North Anatolian Fault, ruptured during the Izmit earthquake. The high velocity gradient of ~10 mm/yr detected across this oblique normal fault could be due either to passive subsidence in the basin located north-east of it or most likely to shallow afterslip.

Our results also show that creep along the Izmit section, previously interpreted as afterslip following the 1999 earthquake, is still taking place and continues to decay more than 19 years after the earthquake. The along-strike distribution of the average creep rate is consistent with previous GPS and InSAR studies (Cakir et al., 2012; Hussain et al., 2016), with a maximum creep rate now reduced to ~8 mm/yr. Creep is spatially correlated with the presence of volcanic rocks on the southern side of the North Anatolian fault that could produce weak minerals at the origin of creep. The analysis of the high temporal resolution of Sentinel-1 data reveals the existence of temporal fluctuations of the creep rate with the detection of a one-month burst of creep in December 2016, with an amplitude of ~10 mm. The occurrence of this transient event, together with similar observations along the Ismetpasa creeping section of the North Anatolian Fault, suggests that fault afterslip is not evolving continuously with time but can occur through a combination of continuous creep that decays with time after a major earthquake and accelerating bursts of creep event.

5. ANALYSIS OF SECULAR GROUND MOTIONS IN ISTANBUL FROM LONG-TERM INSAR TIME_SERIES (1992-2017)

5.1 Introduction

Very rapid social and economic transformation in recent decades caused a huge rural-to-urban migration all over the world, which fueled urban growth. This massive population shift brings many complex challenges together with regard to the sustainable development and natural disaster management. Istanbul is the largest city in Turkey with a population of approximately 14 million inhabitants and one of the most rapidly growing cities in Europe (Leeuwen et al., 2016). According to the Istanbul Transportation Master Plan (ITMP), when taking into account the consequence of Turkey's economic growth in the last two decades and the large immigration, projections indicate that the population will overcome 20 million inhabitants in 2023 (E.B.R.D report. Available online: http://www.ebrd.com/english/pages/project/eia/42163nts.pdf). This rapid population growth poses major threats to the city's development when considering its vulnerability to natural disasters such as earthquakes, landslides and floods, due to heavy and unplanned urbanization practices. Besides, the short distance (~20 km) of the main active branch of the North Anatolian Fault to the city poses major threat for Istanbul (Helgert et al., 2010)

Space-borne Interferometric Synthetic Aperture Radar (InSAR) is a powerful remote sensing tool that enables observations of Earth's surface day and night under all-weather conditions with high precision. Over the past decades, the method has been widely exploited to measure and monitor ground deformation induced by earthquakes (Massonnet et al., 1994; Zebker et al., 1994; Cakir et al., 2003; Diao et al., 2006) volcanoes (Biggs et al., 2016), withdrawal of ground water or other fluids (Tómas et al., 2011; Ruiz-Constán et al., 2016), soil consolidation (Kim et al., 2008; Kim et al., 2010), mining (Abdikan et al., 2014), landslides (Colesanti et al., 2004), permafrost melting (Liu et al., 2014), ground subsidence (Akarvardar et al., 2009; Ferretti et al., 2015), land reclamation (Xu et al., 2016) and sinkholes (Intrieri et al.,

2015). Previous studies have shown the capacity of InSAR methods to measure and map land subsidence due to various anthropogenic factors including ground water extraction in megacities such as Tianjin (Luo et al., 2014; Zhang et al., 2013), Shanghai (Chen et al., 2013), Mexico City, (Osmanoglu et al., 2011) and lithological factors in Bandung basin, Indonesia (Khakim et al., 2014). Among InSAR techniques, Persistent Scatterer InSAR (PS-InSAR) was developed to tackle limitations due to temporal and geometrical decorrelation and atmospheric effects (Ferretti et al., 2000, 2001 & 2004; Colesanti et al., 2003a, 2003b, 2003c) It enables to monitor the temporal evolution of the ground motion by exploiting multiple SAR images acquired over the same area. It uses the radar return signal reflected from persistent scatterers (PS, point-wise phase-stable targets) such as rooftops, large rock outcrops, bridges or motorways, where the spatial density of such PS is high (Ferretti et al., 2001). PS-InSAR analyses provide time series of PS displacements and average surface velocities by searching a motion model relative to a reference point, assumed to be motionless.

In the megacity of Istanbul, PS-InSAR time series analysis have allowed to monitor ground motions induced by antropegenic activities (Calo et al., 2015), lithological features (Walter et al., 2010) and tectonic activities (Diao et al., 2006, 2016). However, there has been little discussion about the long-term temporal evolution of the ground motion and its possible causes. This study presents a PS-InSAR analysis of the secular ground motion in the urbanized metropolitan area of Istanbul. The processed InSAR data (Figure 5.1) span nearly 25-years from 1992 to 2017, with multi-sensor images acquired along ascending and descending orbits. All surface motion anomalies that we identify are associated with ground subsidence induced by various factors including natural compaction, and anthropogenic activities. These subsidence anomalies are carefully measured and analyzed from the perspective of urbanization and assessment of geohazard for the city of Istanbul. The causes of subsidence in cities are diverse and include factors such as lithology, variations in soil moisture content, groundwater exploitation and overburden load associated with human activity. In Istanbul, considering the proximity of several segments of the active North Anatolian Fault (NAF) in the Sea of Marmara that remains unbroken since 1776, the characterization of subsidence susceptibility for Istanbul is crucial with regards to hazard mitigation and urban planning, as it can allow to identify the

vulnerable parts of the region prone to damage by a possible future earthquake. The main goal of the present study is thus to use long-term PS-InSAR time-series 1) to quantify subsidence phenomena and discuss associated causes such as lithology-controlled natural compaction and anthropogenic activities, 2) to monitor the temporal evolution of the subsidence.
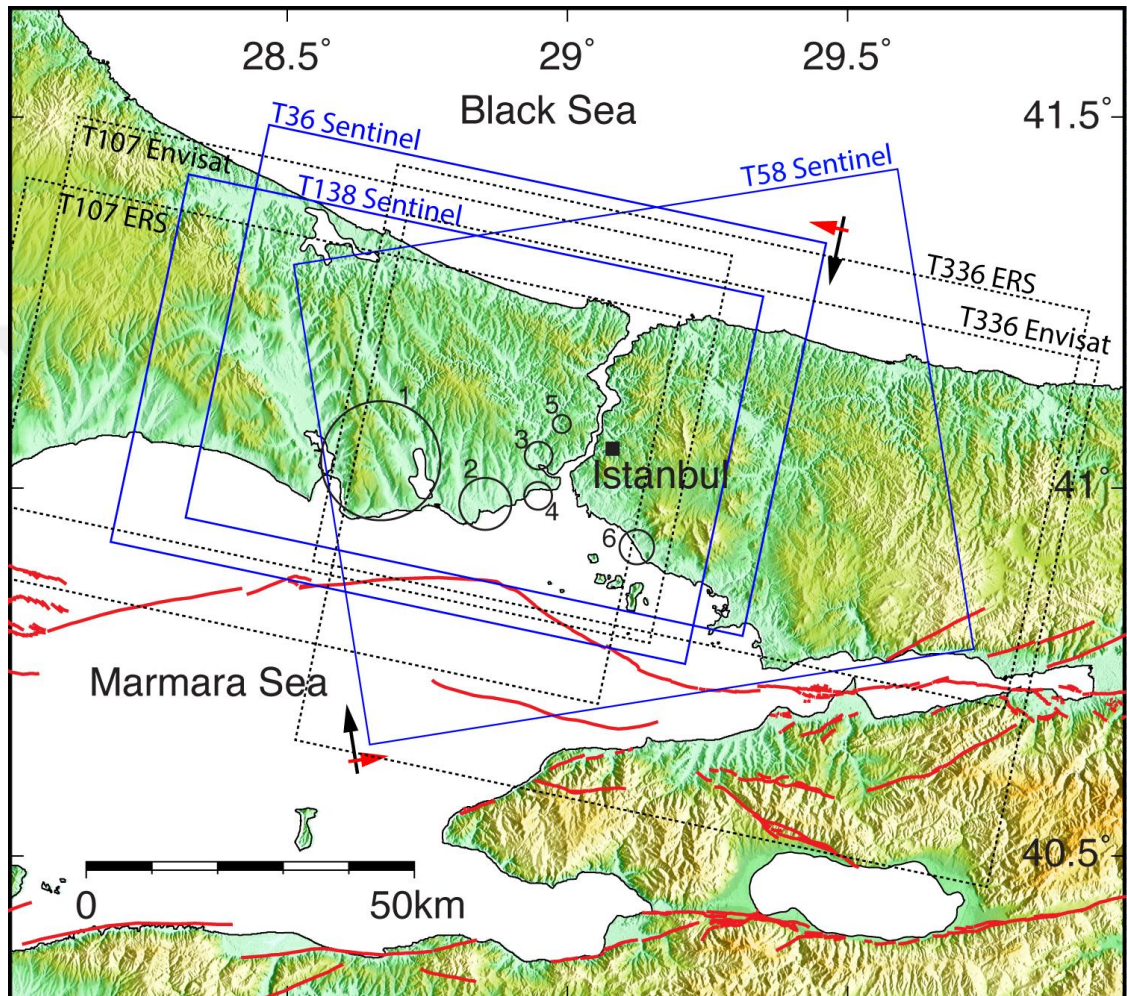
Figure 5.1: Study area and satellite synthetic aperture radar data coverage used in the present study. The shaded topography is given by the Shuttle Radar Topography Mission (SRTM) along the North Anatolian Fault (NAF) in the Sea of Marmara and major faults are drawn in red (Emre et al., 2003). Rectangles labeled with sensor and track number indicate the coverage of the SAR images used in the present study. The red and black arrows indicate satellite's line-of-sight look and flight directions, respectively. Circles with numbers show the study regions in the paper (details are given in the text).

5.2 Background of Study Areas

The present study primarily focuses on six areas where InSAR time-series allow to detect anomalous ground displacement: the region of Haramidere where a series of active natural landslides had been previously mapped (circle 1 in Figure 5.1 and 5.2), the Ayamama flood plain (circle 2 in Figure 5.1), as well as several local subsidence areas related to anthropogenic activities (circles 3 to 6 in Figure 5.1).

5.2.1 Geological setting

The Haramidere and the Ayamama streams are located near the boundary between the Istranca Methamorphic Unit (Paleozoic-Mesozoic) and Istanbul Unit (Paleozoic). These units are covered by the Eocene sedimentary sequence of the Thrace basin (Okay et al., 2001). The Paleozoic metamorphic basement of the study area consists in the east in a thick turbiditic sandstone-shale sequence of Carboniferous age while the Eocene cover is made of limestone, marl and claystone units, transgressive on Çatalca metamorphic units in the west (Figure 5.2).

5.2.2 Study Area 1: Haramidere valley and Avcilar neighborhood

The Haramidere valley is located between Buyukcekmece Lake and Kucukcekmece Lake in the Avcilar Peninsula, located about 15 km north of the NAF which cuts across the Sea of Marmara (Figure 5.2). Although the Avcilar district is located at a distance of 120 km west of the epicenter of the August 17, 1999 Izmit earthquake, it was the only area in the Istanbul metropolitan region that suffered extensive damage (Tezcan et al., 2002). During this earthquake, 27 buildings collapsed and 2076 other buildings were heavily damaged and 273 casualties were reported in Avcilar (Ozmen 2000; Sen 2007). The maximum ground acceleration measured on soft sediments was 0.25 g, six times higher than the peak ground acceleration recorded on the bedrock in the center of Istanbul (Tezcan et al., 2002). This difference is the result of the amplification of seismic-waves in surficial layers with soft lithology (Tezcan et al., 2002; Sen 2007; Meremonte et al., 2000; Ozel et al., 2002; Ergin et al., 2004). Despite a low background seismicity, which suggested no active faulting in the region (Eyidogan 2006), destructive and widespread damage during the 1999 Izmit earthquake drew a considerable attention on this area, requiring the reassessment of active faulting. In order to investigate any relationship between faults and damage

observed in Avcilar and vicinity, faults mapping was refined from field studies and seismic reflection analyses (Ergintav et al., 2001; Sen 1994, 1996; Koeri 2000). These studies showed that the presence of secondary faults might be an important driving factor for the localized seismic amplification (Diao et al., 2006; Dalgic et al 2004).
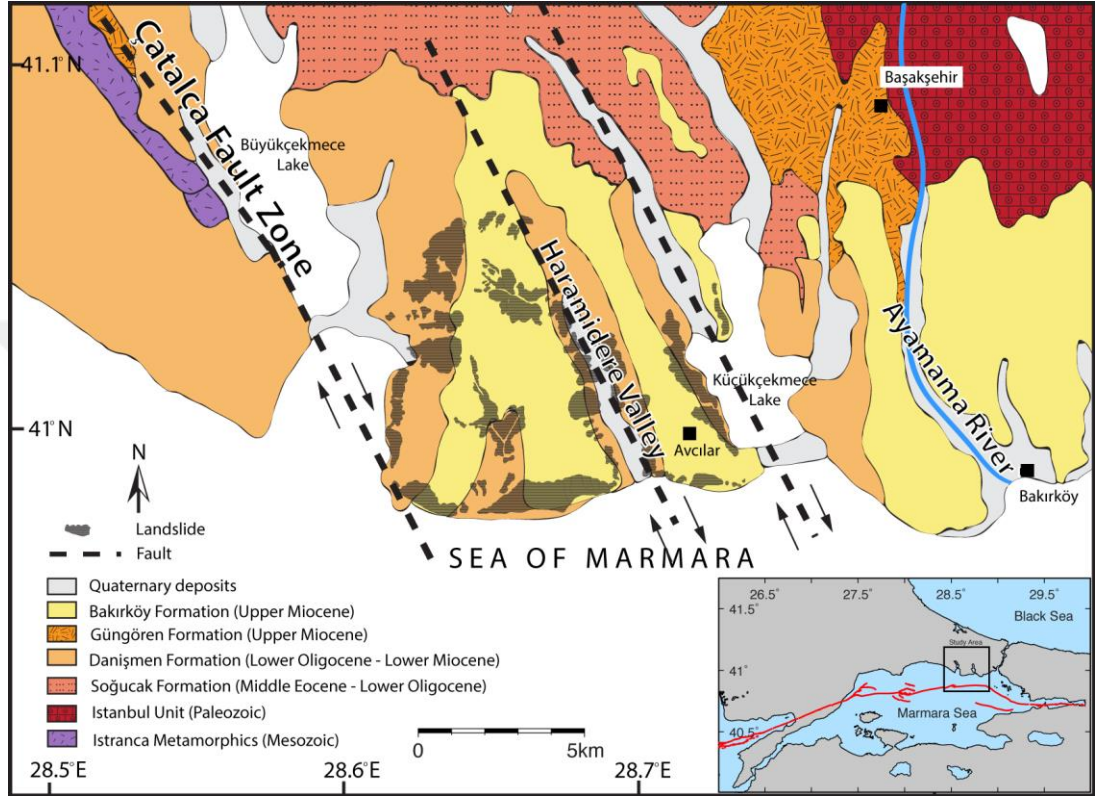
Figure 5.2 : Simplified geological and structural map of study areas 1 and 2. Numerous active landslides (dark green patches) were mapped between Küçükçekmece and Büyükçekmece lakes (simplified from Ergintav et al., 2001; Duman et al., 2004; Ozgul et al., 2005). Inset map shows figure area north of the Sea of Marmara and the main segments of the NAF in red (Emre et al., 2005).

Landslides have been identified as another important geohazard in the suburb of Avcilar for many years (Duman 2004; Duman et al., 2005a; 2005b). Recent events in that area often result from the reactivation of old landslides due to the overloading of the existing landslides by new constructions. The investigation of these old landslides in more detail is very important to anticipate measures that could be taken to avoid future possible damage in the urbanized center of the Avcilar peninsula. A total of 391 landslides are mapped (Figure 5.2) in the region (Duman 2004). Approximately half of all landslides are distributed between Buyukcekmece and Haramidere valley, which are important local landforms in the region (Figure 5.2).

Based on field geological observations, Duman et al. (2005a; 2005b) have argued that the parameters that control landslide initiation are shallow groundwater level, lithology and liquefaction.

5.2.3 Study Area 2: Ayamama river valley

The Ayamama valley is located in the western part of Istanbul, east of the Haramidere valley (Figure 5.2). The river flows north-south from the eastern part of Basaksehir district and towards the Sea of Marmara in Bakirkoy district (Einfalt & Keskin 2010). It runs through the heavily urbanized and highly populated area of the European side of Istanbul. The lower parts of its basin show various land use patterns and a high density of population (Komuscu et al., 2013). The Ayamama stream is known to produce seasonal flooding. According to the municipality of Istanbul, sedimentation and illegal urbanization in riverbeds have decreased floodplain capacity, which has caused periodic floods and over flows. One of the worst flooding events has affected the region in September 9, 2009 and has caused 31 casualties and 50 injuries. In the city's development plan, the Ayamama river basin and its surrounding zone had been set aside for recreational areas. However, after an amendment had been made to develop it into residential area in 1997, industrial and residential land use rapidly increased along the axis of the stream (Ozcan & Musaoglu 2010).

5.2.4 Study Areas 3 to 6: Subsidence events associated with land reclamation and urbanization

Istanbul lies on both sides of the Bosphorus strait (*İstanbul Boğazı*) and has been subjected to heavy and unplanned urbanization. This rapid urbanization gave rise to land reclamation along the coastal areas of the Marmara Sea in order to provide new recreational areas to compensate for the destruction of green areas (Burak & Kucukakca 2015). Nearly 2.6 square kilometers of land have been gained from Istanbul coast by filling up the sea since 2000. We have focused on the two recreational areas on the Yenikapi neighborhood and Maltepe district to investigate the ground deformation related to land reclamation by PS-InSAR method (sites 4 and 6). Another two local subsidence phenomena have been observed along the banks of the Golden Horn (Haliç, site 3) and around a skyscraper located in the Levent neighborhood of Istanbul (site 5).

5.3 Datasets

The SAR data used in the present study consist of 291 *C-band* (5-6 GHz, ~6 cm wavelength) images acquired with various sensors, including 51 ERS 1/2 images on two overlapping ascending tracks spanning from 1992 to 2001, 52 ENVISAT images on two overlapping ascending tracks spanning from 2003 to 2011 and 188 Sentinel 1A/B TOPS images in one ascending and two descending orbits acquired between 2014 and 2017 (Figure 5.3, see Table 5.1 for details). The Istanbul metropolitan area is entirely covered by all tracks. These multi-orbit/sensor datasets enable us to examine the consistency between different sets of observations by inter-comparisons.

ERS 1/2 and ENVISAT ASAR are the C-band satellites and acquire SAR images since 1992 which are characterized by a medium spatial resolution (20 m x 4 m) and 35 days revisint time. Sentinel-1 constellation offers an improvement in revisiting time (12-day) over ERS-1/2 and ENVISAT ASAR but acquaring higher resolution. In this study, we used Single Look Complex (SLC) Interferometric Wide (IW) mode products. It acquires the data with a 250 km swath at 5 m by 20 m spatial resolution

Table 5.1 : Characteristics of each processed track.

Track	C band/ satellite	Geometry	Time Interval	Interferograms Used	Density^2 (PS/km^2)
T107	ERS 1/2	Descending	1992-2001	28	93
T336	ERS 1/2	Descending	1992-2001	21	212
T107	ENVISAT	Descending	2003-2011	25	190
T336	ENVISAT	Descending	2003-2011	25	176.8
T58	SENTINEL 1	Ascending	2015-2017	56	250.4
T36	SENTINEL 1	Descending	2014-2017	65	289.6
T138	SENTINEL 1	Descending	2014-2017	65	252.7

[1] SENTINEL 1 A/B TOPS; [2] Density of Permanent Scatterers (PS) in the urban areas.
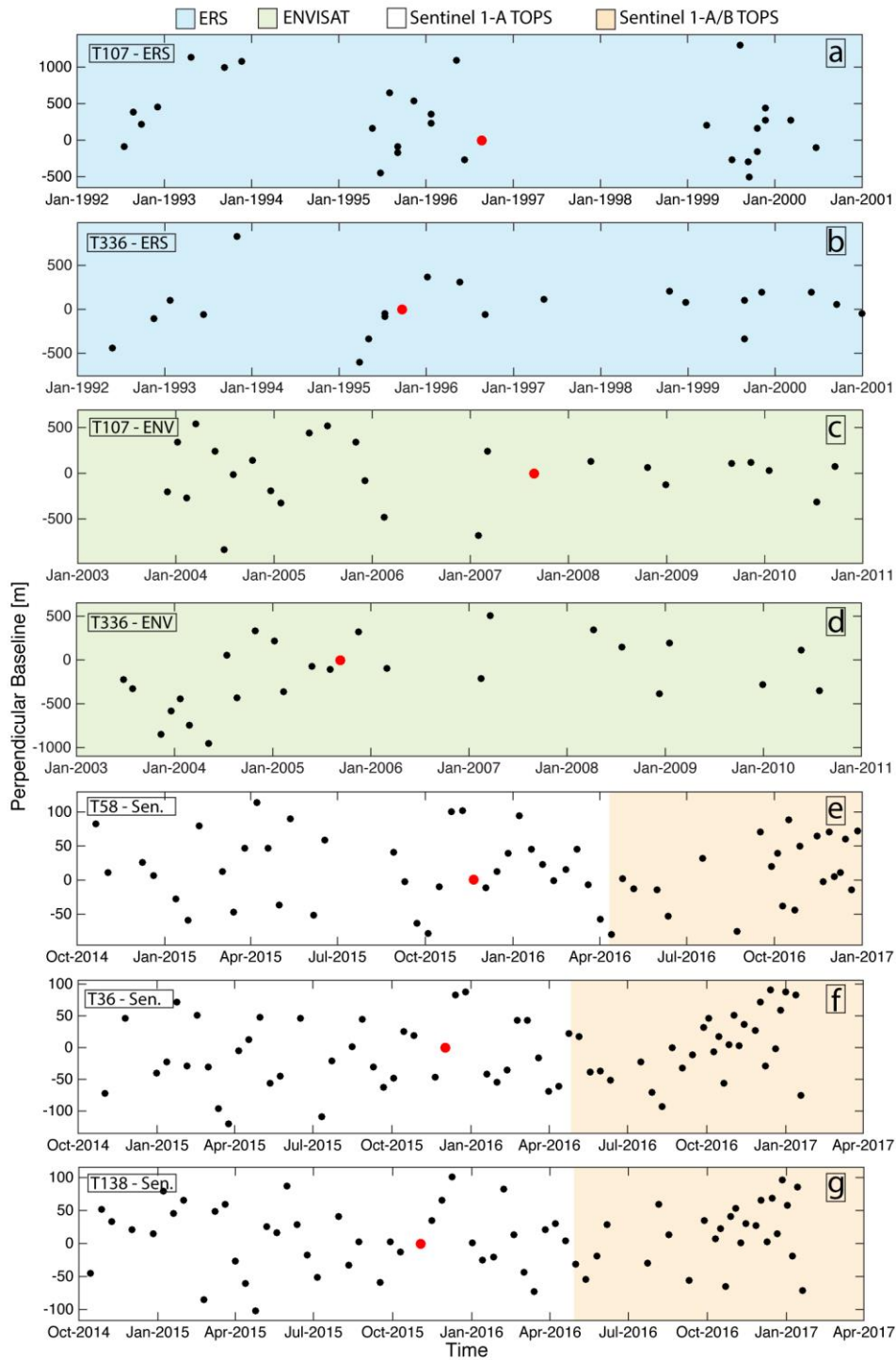
Figure 5.3 : Baseline versus time plots for the seven tracks used in this study. The red dots indicate the master image used as a reference for each track. For the Sentinel data, the period when the two satellites 1A/1B were operational is indicated in orange (before this period only satellite 1A was operational).

5.4 Results and Discussion

5.4.1 Main deformation patterns

Figure 5.4 shows the mean line-of-sight velocity fields calculated from PS-InSAR time series on the metropolitan city of Istanbul with varying time-spans depending on sensor. Negative velocities (cold colors) represent displacement of the ground toward the satellite and positive velocities (warm colors) indicate displacement away from the satellite. Red lines in the Sea of Marmara indicate the submarine branches of the NAF. Average line-of-sight velocity (a) for Sentinel ascending track 58. (b) for SENTINEL 1A/B descending track 36, (c) for Sentinel descending track 138, (d) for Envisat descending track 107, (e) for ERS descending track 336, (f) for ENVISAT descending track 336 and (g) for ERS descending track 107. A main deformation feature, common to all tracks, is the NNW-SSE elongated area in the southwest region of Istanbul, along the Haramidere valley on the Avcilar peninsula (Figure 5.4, circle 1 in a, site 1 described in section 5.2.1 and 5.2.2). The associated motion is away from satellite for both descending and ascending tracks, suggesting a dominant subsidence signal, peaking at up to 10 mm/year in the line-of-sight. We identify another likely subsiding area along the Ayamama stream valley. This anomaly is elongated in a WNW-ESE direction and located along the western side of the Kucukcekmece Lake (Figure 5.4a circle 2, named as site 2). The area labeled with circle 3 in Figure 5.4a (named as site 3) covers the primary inlet of the Bosphorus called Golden Horn urban waterway. This Golden Horn's bank is also likely subject to subsidence. Other potential subsidence anomalies caused by the settlement of the reclamation in the coastal areas are identified along the northern coast of the Marmara sea (circles 4 and 6 in figure 5.4a corresponding to sites 4 and 6). Lastly, we point to a local subsidence signal at a rather fast rate observed around a skyscraper (Figure 5.4a, circle and site 5) located in the Levent neighborhood of Istanbul. The spatial and temporal variations of these different deformation patterns are discussed with their possible underlying causes in the next sections.
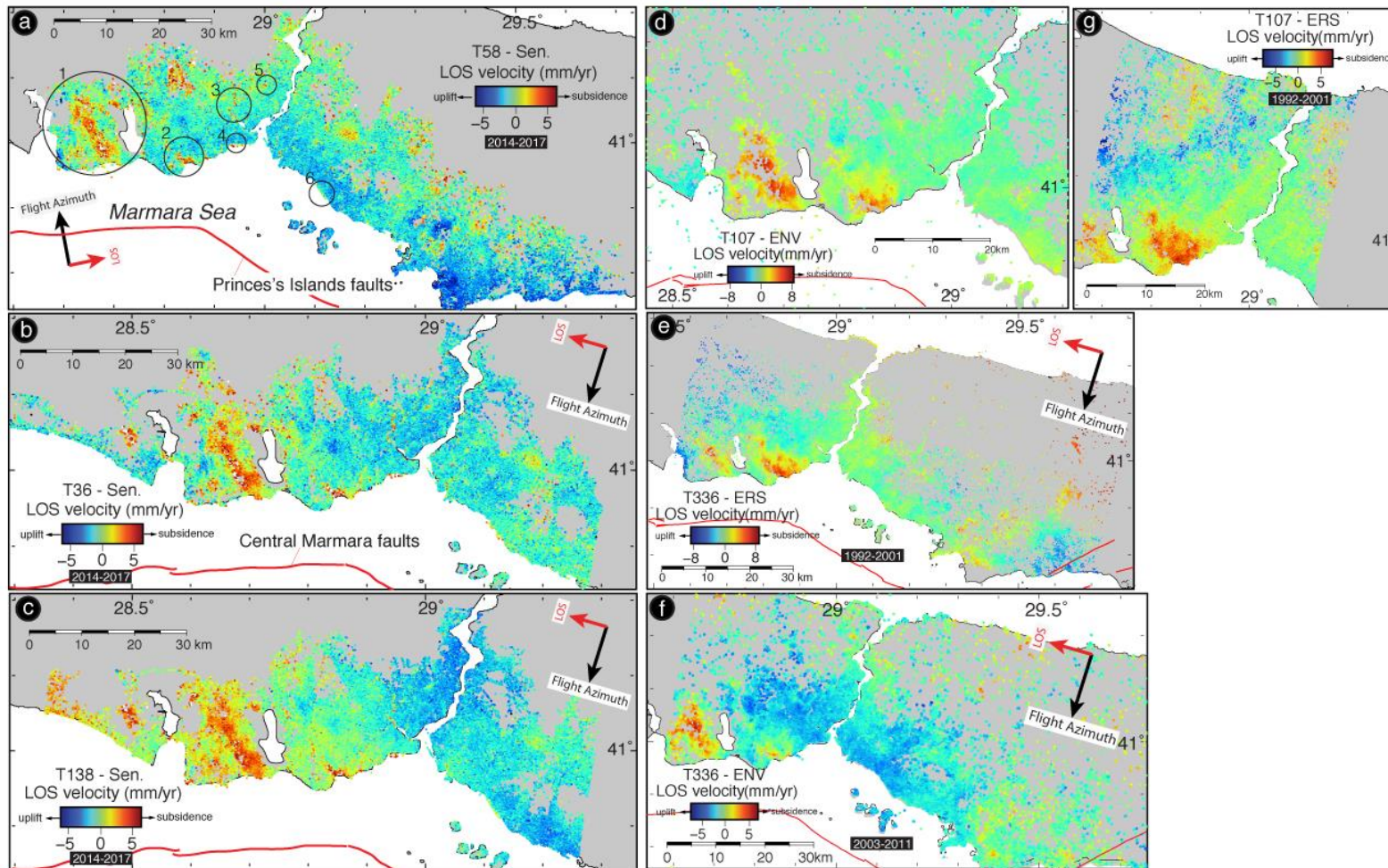
Figure 5.4 : Averaged line-of-sight velocity maps of Istanbul metropolitan area, from InSAR time series analysis, with varying time-spans depending on sensor

We first quantitatively assess the consistency of InSAR mean velocity measurements calculated from different datasets across different time periods, for the widest areas of subsidence in the Haramidere Valley and Avcilar valleys. An inter-comparison of the displacement rates in these areas is performed using a two-step procedure. In a first step, the mean-velocity fields are down-sampled by a factor of 10 to minimize errors of geo-localizations (spatial mismatch between measurements). In a second step, we select all pixels in the localized deforming areas of Haramidere Valley and Avcilar neighborhood that are common to a pair of overlapping tracks, and compare the distribution of their subsidence rates for each pair of tracks (figure 5.5). The consistency of velocities is good in overall (mean correlation = 0.62). The observed differences could originate from various factors: (1) different temporal coverages, (2) geo-localization uncertainty, (3) InSAR processing errors, and (4) seasonal effects (Ge et al., 2014).

5.4.2 Site 1 : Haramidere valley

Close-up views of the elongated pattern of subsidence in the Haramidere valley are shown on figure 5.6 for all tracks. In order to quantify the vertical, subsidence component of the motion, we have decomposed the mean PS-InSAR line-of-sight velocity fields into east-west and vertical components using the method described by (Samieie-Esfahany et al., 2009). We only used the velocity fields calculated from Sentinel 1A/B images (two tracks, 58 [Asc] and 138 [Dsc]) that cover the same time interval, to calculate this decomposition. We assume there is no north-south displacement. Doing so, we reduce the number of unknown variables for each permanent scatterer point to two displacement components, d_{ver} the vertical displacement (positive downward) and d_{hor} the horizontal displacement in the east-west direction (positive toward west). In a first step, we resampled the mean line-of-sight velocities for the ascending and descending tracks onto a 0.0005° x 0.0005° regular grid (approximately 10 m spacing). We used the nearest neighbor procedure in the resampling of persistent scatterer pixels within 30 m of the center of each grid nodal point. In a second step, we selected all the pixels that exist in both the ascending and descending tracks. For further interpretation of the displacements, we referenced the two tracks using reference points located in an area assumed to be stable (circle in NE part of figure 5.6). In a third step, the decomposition of line-of-

sight velocity fields into east-west and vertical components was calculated taking into account the local incidence angle of the satellite view (figure 5.7).

$$\begin{pmatrix} d_{asc} \\ d_{dsc} \end{pmatrix} = \begin{pmatrix} \cos\theta_{asc} & -\cos\alpha_{asc}\sin\theta_{asc} \\ \cos\theta_{dsc} & -\cos\alpha_{dsc}\sin\theta_{dsc} \end{pmatrix} \begin{pmatrix} d_{ver} \\ d_{hor} \end{pmatrix}, \qquad (5.1)$$

where θ_{asc} and θ_{dsc} represent the local incidence angles and α_{asc} and α_{dsc} are the satellite heading angles of Sentinel-1's ascending and descending modes, respectively.
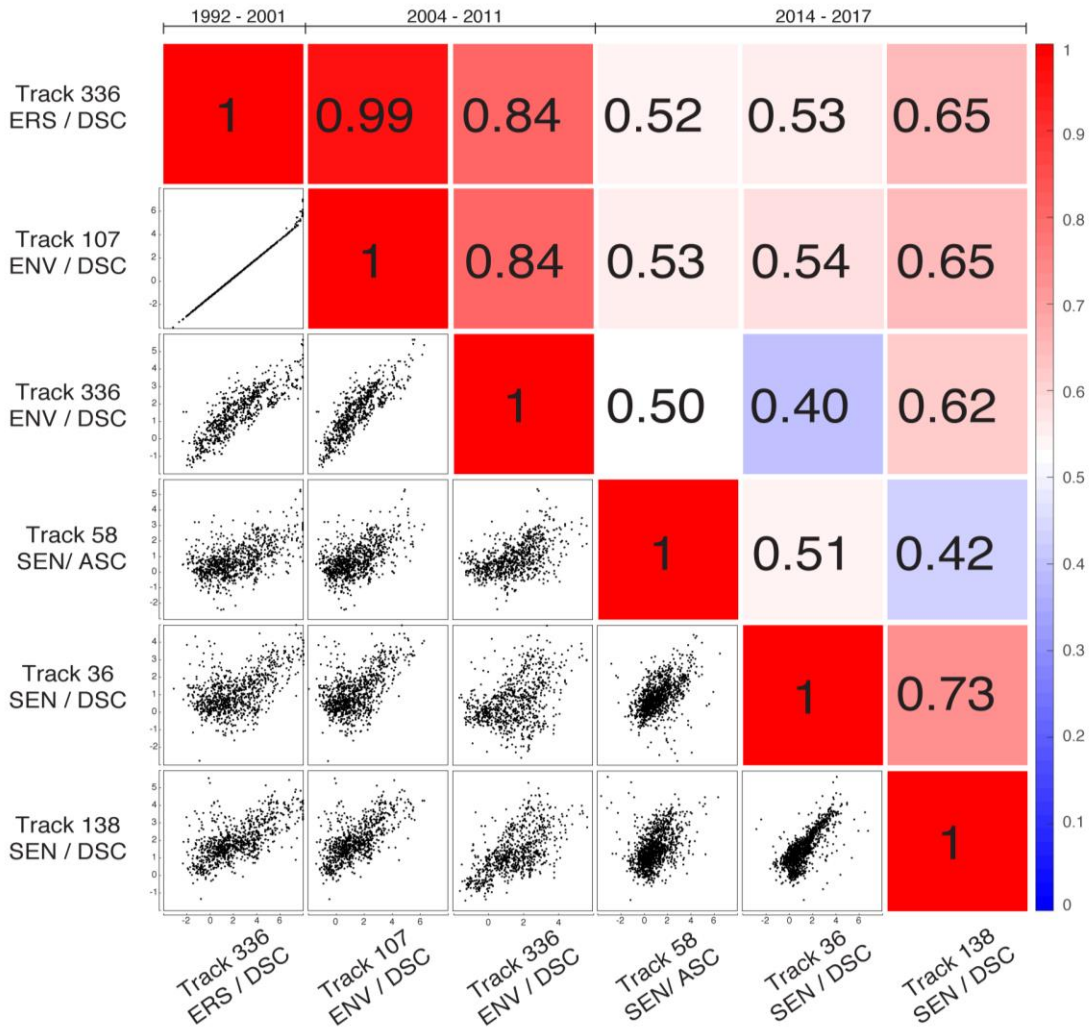
Figure 5.5 : Quantitative comparison of the displacement rates between all tracks used in the present study. In upper-right triangle matrix, pairwise correlations of different tracks are shown, with correlation values and color intensities (blue and red indicate low and high correlation, respectively). In lower-left triangle, black dots denote the points that can be extracted on both tracks. SEN and ENV in the panel represent SENTINEL and ENVISAT, respectively.
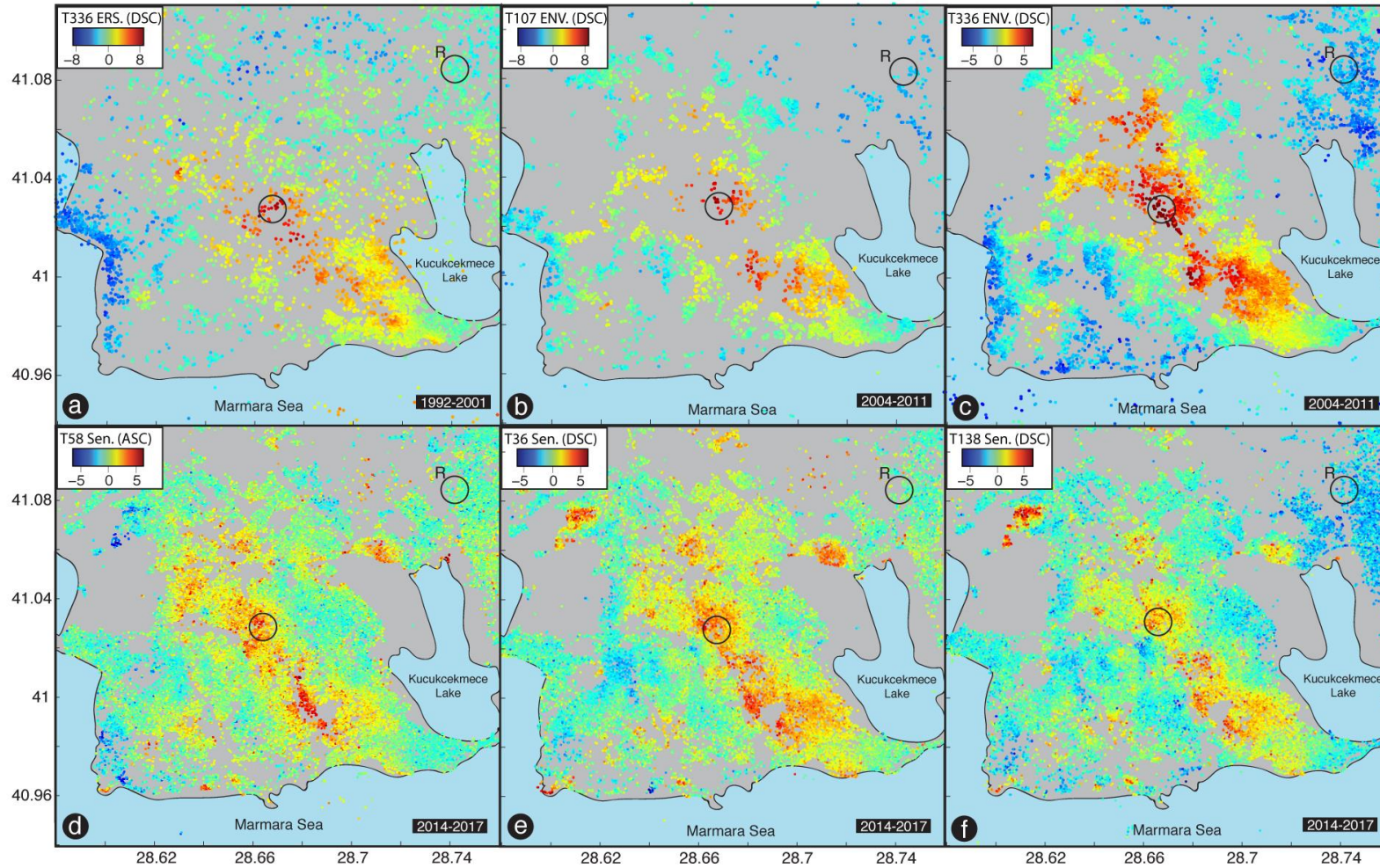
Figure 5.6 : Zoom views of displacement rates in the Haramidere Valley and its surrounding area.

In Figure 5.6, the mean velocity value of the PS-InSAR points within the solid black circle in the center of maps has been used to illustrate the temporal evolution of the subsidence associated with weak-lithology (figure 5.8). It is referenced to the mean value of PS-InSAR points within the circle labeled R which is considered as a stable area. DSC and ASC labels are for descending and ascending orbits.

In Figure 5.7-c, the vertical displacement field shows that subsidence occurs on both banks of the Haramidere valley and follows an elongated area in the valley in a northwest-southeast direction.
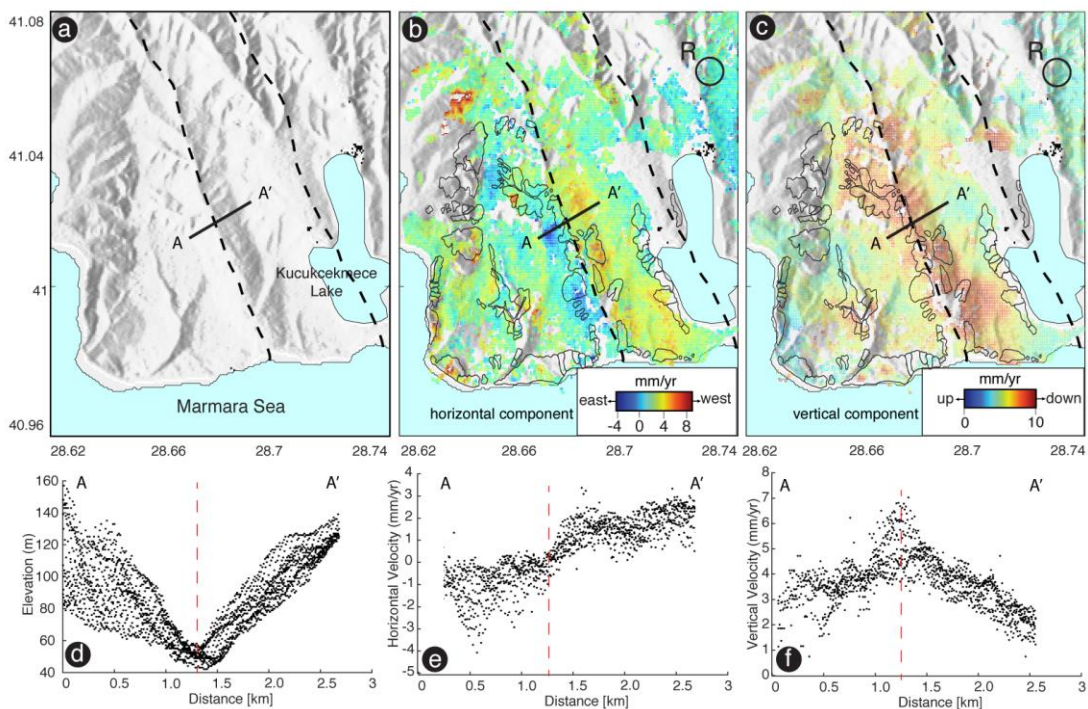
Figure 5.7 : Decomposition of horizontal and vertical components of ground displacement using only S-1 datasets. (**a**) The shaded topography is given by the Shuttle Radar Topography Mission (SRTM) along the Avcilar region. Fault lines are simplified from Ergintav et al., 2001. (**b**) Vertical component. Patches with thick dark boundaries correspond to landslides identified on geological maps and shown on Figure 2 (simplified from Duman2004; Ozgul et al., 2002). (**c**) Horizontal component in the east-west direction. (**d**)Valley-perpendicular elevation profile extracted from (a). (**e**) and (**f**) are horizontal and vertical velocity profiles extracted from (b) and (c) respectively.

This region has a long, slow-moving landslides history and is located in an area with shallow water level, poor soil conditions and weak lithology, all parameters considered as favoring landslides (Akarvardar et al., 2009; Tezcan et al., 2002; Dogan et al., 2012). The subsidence we observe coincides in overall with previously

mapped active landslide zones. However, contours of these mapped landslides do not match precisely with areas of highest subsidence in our vertical velocity map. The horizontal component in the east-west direction derived by decomposition shows the horizontal movement of both banks of the valley in opposite direction, toward the valley center, which is in agreement with the expected horizontal movement induced by subsidence.

To analyse the subsidence temporal evolution (figure 5.8), we select permanent scatterer points located in an area previously detected as undergoing landslide activity and where the subsidence rate is among the highest observed in the present study. For the sake of consistency between datasets acquired from different viewing geometries, these selected PS points are from an area where the horizontal velocity is considered neglectible (circle in center of Figure 5.6), so that line-of-sight velocities are converted into vertical velocities by a simple geometrical equation. The date of the first SAR image used here is taken as the reference time of the time series. As seen in Figure 5.8, the three datasets used for the Haramidere valley and Avcilar area have different starting dates and temporal coverage. For comparison, we set one reference time as 26 May 1992 for the three datasets and the time series mapped from Envisat and Sentinel datasets were shifted with a constant, which was calculated by assuming the site is undergoing subsidence with a constant rate (Figure 5.8).

calculated by assuming the site is undergoing subsidence with a constant rate (Figure 5.8).
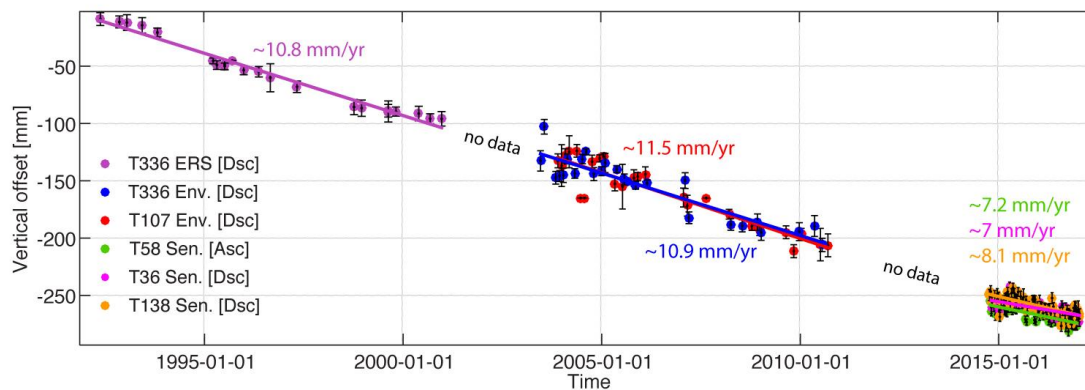
Figure 5.8 : Time series of the vertical displacement at the selected PS points circled in center of figure 5.6 (referenced to points in area labeled R in figure 5.6).

Although the subsidence rate calculated from ERS and Envisat datasets are consistent with each other and match well, the subsidence rates obtained from Sentinel datasets are slightly smaller. Two reasons might lie behind this difference. The first reason is related to the relatively short duration of SENTINEL 1 A/B time series, which could alter the accuracy of the rate estimate, and the second reason may be the retardation of the settlement, due to a long-term decay of the soil consolidation rate related to ground water extractions. Such an exponential decay of ground subsidence was proposed to explain InSAR time series on Great Salt Lake in Utah (Hu et al., 2017).

Ground subsidence in the Avcilar peninsula has been previously reported at a mean rate of 6 mm/yr using InSAR analysis of ERS-1 and ERS-2 satellite images between 1992 and 1999 (Akarvardar et al., 2009), and at a rate of 10 mm/yr using ERS 1/2 and ENVISAT satellites from 1992 to 2010 (Ge et al., 2014). These authors concluded that the spatial coverage of the land subsidence in this area, in overall consistent with ours, is associated with partially saturated and unconsolidated shallow layers of soil formation with a relatively weak lithological profile. The results of the present study thus support the observation of land subsidence in Avcilar, at similar to higher rates. Such type of lithology-controlled subsidence has also been observed in Bandung basin on the island of Java in Indonesia, using ALOS-1 dataset, although at much higher rates (up to 12 cm/yr), along the

68

boundaries between consolidated rocks and unconsolidated sediments (Khakim et al., 2014).

5.4.3 Site 2 : Ayamama river

Another subsidence zone lies along the dense settlements of Ayamama stream banks in the western part of Istanbul (site 2, figure 5.4a). Here, the river has the typical morphology of a delta and the streambed is mostly composed of young alluvial deposits, varying in thickness in the range 3-10 m (Kilic et al., 2005). The subsidence rates we measure are about 6 mm/yr at maximum in the line-of-sight, corresponding to a maximum vertical subsidence rate of about 10 mm/yr (Figure 5.9).
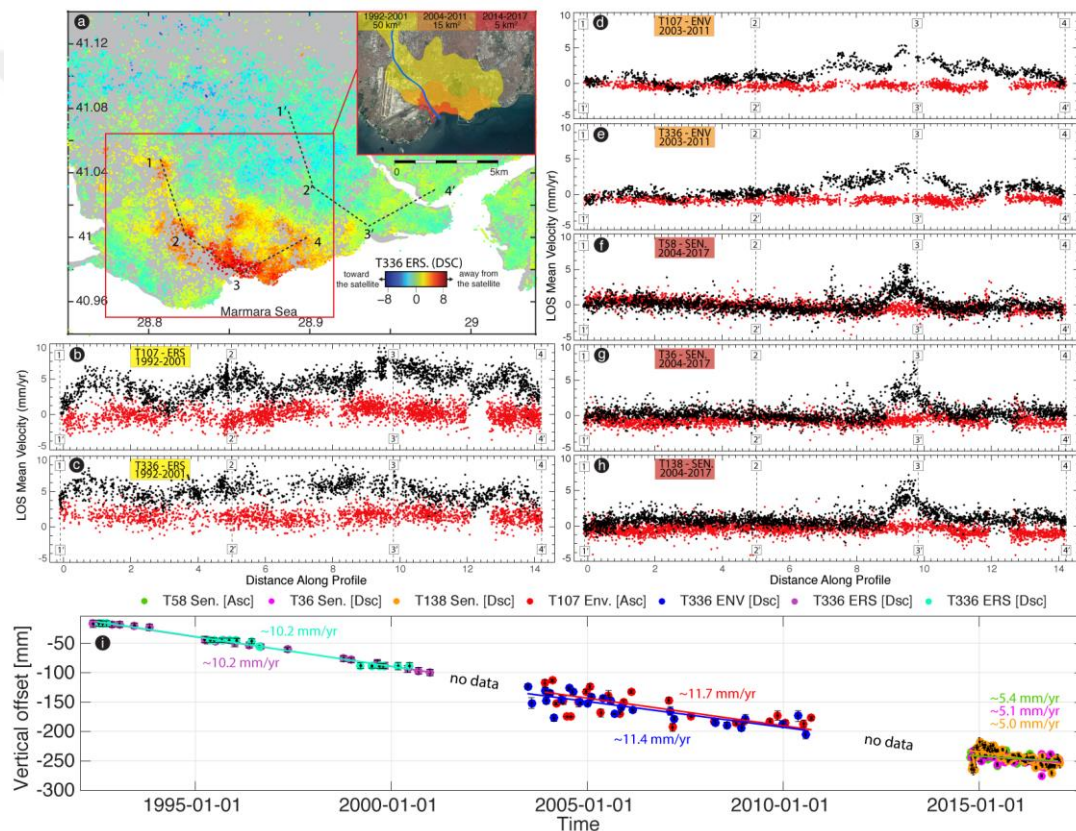
Figure 5.9 : Spatio-temporal characteristics of subsidence along the Ayamama river valley study area. (**a**) Mean displacement rates in line-of-sight obtained from track 336 ERS dataset. The black dashed lines indicate two profiles, one in an area with active subsidence (profile labeled 1-4), and the other one with the same length in an area considered as stable and used as a reference (profile labeled 1'-4'). Inset map indicates the temporal and spatial pattern of subsidence for the region, from 1992 to 2017. (**b-h**) Rates along the profiles 1-4 (black) and 1'-4' (red) taken for each track. (**i**) Temporal evolution of coastal subsidence of selected points around point 3 in Figure 5.9a.

69

The area affected by subsidence is shrinking gradually (Figure 5.9) during the observation period, which we interpret as resulting from the flood prevention and remediation project of the river and stream system, which has started in 2008. The subsidence pattern along the Ayamama stream was firstly reported by (Walter et al., 2010) with a more limited data set, who suggested that the ongoing land subsidence in the region is related with sediment consolidation process and might be direct or indirect consequences of the destructive flood events, such as one in 2009. This is thus consistent with our interpretation of recovery of the region following the restoration of the river and stream system.

5.4.4 Sites 4, 6 and 3

We also identify other sites along the terrestrial and coastal region of Istanbul undergoing ground subsidence. The subsidence that we relate to land reclamation in two recreational areas on the Yenikapi neighborhood (Figure 5.10a, site 4 in Figure 5.4a) and Maltepe district (Figure 5.10d, site 6 in Figure 5.4a), which were constructed in 2014, is observed at a vertical rate of 10 mm/yr. This subsidence is presumably related to the compaction induced by primary consolidation process of the alluvial clay beneath the reclamation zone. The subsidence rates measured in both reclamation areas are likely dependent on the physical characteristic and thickness of the underlying alluvial deposit and used matrix of filling material (Kilic et al., 2005; Plant et al 1998) Another local subsidence area related to a similar phenomena is observed along the shores of the Golden Horn (*Haliç*) (Figure 5.10b, site 3 in Figure 5.4a). A significant part of this subsidence is located on reclamation areas transformed into parks and recreational facilities along both banks of the Golden Horn. Besides that, the shorelines in this area have undergone significant urban changes within the frame of the renovation project of all the waterfronts in Istanbul. During the renovation, sediments made of loose clay deposits were removed from the shallowest parts of the Golden Horn, which might have triggered subsidence in the nearby waterfront areas. The subsidence pattern along the Golden Horn that we observe is consistent with the coastal subsidence previously described in the figures 5.5 and 5.7 of (Colesanti et al., 2003) that used a dataset of high-resolution TerraSAR-X SAR images covering the period 2010-2012. In their analyses of subsidence evolution over the urbanized region of Istanbul, these authors

similarly concluded that the pattern of settlement along the Golden Horn shores are caused by anthropogenic factors arising from unsustainable urban development.
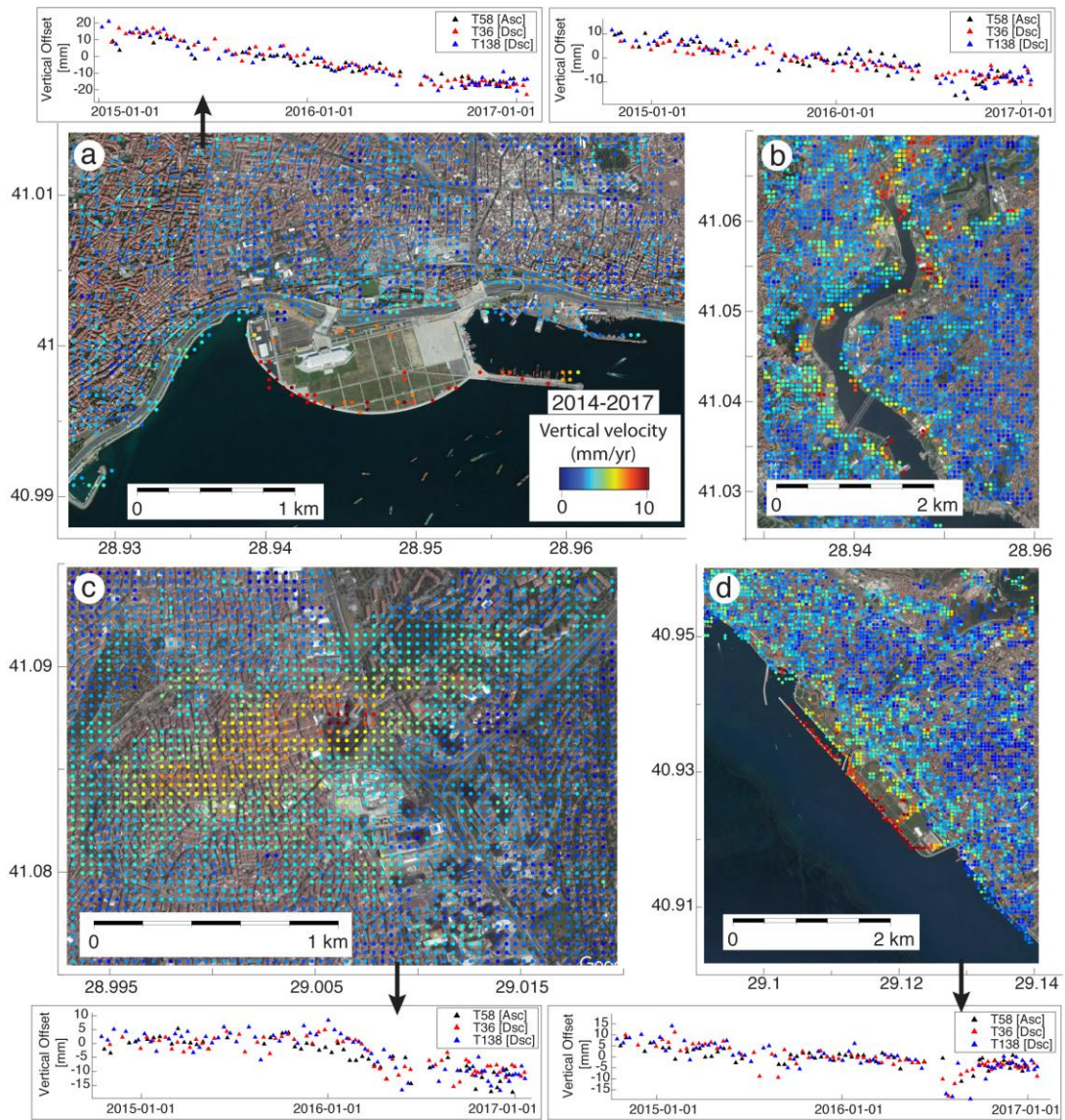
Figure 5.10 : Vertical velocities obtained by decomposition of mean velocity fields of Sentinel 1 data (T58 ascending track and T138 descending track) superimposed on Google Earth image in Istanbul, and relevant time series of the vertical displacement. Black, red and blue triangles represent the ascending T58, descending T36 and descending T138 tracks, respectively. (**a**) Yenikapi coastal and land reclamation area (circle 4 in Figure 4a). The color scale represents the vertical displacement of the surface. (**b**) Golden Horn area (circle 3 in Figure 5.4a). (**c**) Highly urbanized area of Istanbul, with subsiding persistent scatterer points clustered around the highest skyscraper of Istanbul (circle 5 in Figure 5.4a). (**d**) Maltepe reclamation zone (circle 6 in Figure 5.4a).

71

5.4.5 Site 5

High skyscrapers might suffer rapid settlement and declination and cause local ground surface subsidence due to consolidation of the underlying soft soil deposits. In this study, we detect a very localized subsidence pattern around a skyscraper built in 2010 and other high-rise buildings in Levent neighbourhood of Istanbul, starting from 2016 with an average subsidence rate of about 15mm/yr (Figure 5.10c). Time series analysis of point targets surrounding the skyscraper shows very rapid increase of subsidence rate during the first four months of 2016, which might be related with groundwater lowering around the foundation of the building that may cause downward movement of the surface surrounding the building.

5.5 Conclusion

Istanbul has been subject to intense industrialization and population increase especially since the 1960's and this is causing very rapid urbanization and heavy land-use changes. We identified several sites along the terrestrial and coastal region of Istanbul undergoing vertical ground subsidence at rates ranging from 5 to 15 mm/yr. In the present study, a PS-InSAR time series analysis was performed using 291 C-band SAR images to characterize these subsidence phenomena by combining multi-track/sensor InSAR datasets to provide insights into the potential hazards induced by local soil conditions and human activities. Using the PS-InSAR technique, enough time-coherent pixels were obtained over six different sites in Istanbul. The most extended, clearly visible subsidence signals have been detected over the western part of Istanbul consistently in all the frames. The spatio-temporal variability of the ground displacement was measured over the last 25 years in Avcilar, which suffered extensive damage during the 1999 Izmit earthquake and along the Haramidere valley where a long-lasting landslide history has been reported. The time series analysis in this region reveals that Haramidere valley banks are undergoing ground vertical subsidence at a rate of 10 ± 2 mm/yr. Another subsidence area has been reported along the Ayamama river banks, made of shallow alluvial deposits due to the local substratum consolidation process, at a rate of 10 ± 1.8 mm/yr, and the surface area affected by subsidence is shrinking gradually following the restoration of river and stream system, which has started in 2008. The inter-comparison of PS-InSAR measurements from different satellite sensors for the

western part of Istanbul show that the correlation between the mean velocity fields are high between 1992-2011 and decrease with time due to spatio-temporal change of the ground deformation. Sentinel-1A/B InSAR measurements acquired between 2014 and 2017 show that reclaimed lands in both European (Yenikapi reclamation area) and Asian (Maltepe reclamation area) coastlines of Istanbul underwent significant subsidence of up to 8 ± 1.3 mm/yr as a result of primary consolidation process of the alluvial clay beneath the filling material. Lastly, a very localized subsidence pattern has been detected around a skyscraper with average subsidence rate of 15 ± 1.2 mm/yr.

On the whole, we can conclude that during the interseismic period human-driven changes produce a more significant control on the coastal subsidence in Istanbul than natural factors. In future studies, such high-resolution SAR data over the very dense urban area of Istanbul could help monitoring continuously the urbanized areas suffering from the land subsidence. With this purpose, future plans include the processing of high-resolution X-band sensors COSMO-Skymed and TerraSAR-X datasets to better quantify the surface settlement and reveal the underlying causes of these settlements in order to provide more complete data to public organizations in charge of sustainable urban policies and hazard mitigation.

6. INVESTIGATING SUBSIDENCE IN THE BURSA PLAIN, TURKEY, WITH SATELLITE RADAR INTERFEROMETRY

6.1 Introduction

Subsidence is one of the most diverse forms of ground vertical displacement, varying from local collapses to regional-scale sinking. Depending on the deformation regimes of the subsidence, vertical displacement may also produce horizontal deformation that may have significant damaging effects. A previous study has shown that the Bursa plain in Turkey has been subsiding (Kutoglu et al., 2014). The first InSAR-derived observation of land subsidence was documented using four ALOS PALSAR (L-band) images acquired between 2007 and 2010 (Kutoglu et al., 2014). These authors investigated the surface deformation using differential InSAR technique and concluded that Bursa plain is subsiding at a rate of 10.9 cm/yr. They suggested that this subsidence is driven by local tectonic activity, where a pull-apart basin geometry is caused by strike-slip faulting. However, it is well known that subsidence may also occur due to the compaction of unconsolidated sediments that results from exploitation of groundwater (Galloway et al., 1998; Béjar-Pizarro et al., 2017). It is therefore important to determine the mechanism of subsidence and its spatiotemporal characteristics because it allows developing better mitigations that could minimize the risk of damage to surface structures and infrastructures.

Ground subsidence is a common phenomenon in urban areas built on thick, unconsolidated loose soil layers consisting of clay, silt and peat formations (Zeitoun et al., 2013), as it is the case in the Bursa basin. Subsidence has been correlated to strata lithology, formation and structure (Wang et al., 2013). Dewatering of loose soil layers in which the water provides structural support produces volumetric contraction and surface subsidence. Consequently, the depth of groundwater exploitation strong controls the magnitude of land subsidence.

Space-borne Interferometric Synthetic Aperture Radar (InSAR) is an observation technique that uses differences in reflected radar signals acquired at different times to detect and monitor different forms of ground deformations over wide areas (up to

400x400 km) in high resolution and precision. Due to the development of new satellite technologies and advancing processing techniques, InSAR has been successfully used to investigate deformation resulting from subsidence due to withdrawal of groundwater or other fluids (Béjar-Pizarro et al., 2017; Massonnet et al., 1997; Fielding et al., 1998; Wright & Stow 1999; Crosetto et al., 2018), soil consolidation (Kim et al., 2010), subsurface mining or collapse of old mines (Carnec & Delacourt 2000; Abdikan et al., 2014), thawing subsidence (Rykhus et al., 2008), tectonic activity (Temtime et al., 2018), and soluble earth materials (Baer et al., 2018). Besides, InSAR has also been used to infer aquifer hydraulic properties such as compressibility and storage coefficient as well as the mechanics of aquifer system (Galloway et al., 1998; Béjar-Pizarro et al., 2017; Hoffmann et al., 2001; Tómas et al., 2009; Calderhead et al., 2011; Ezquerro et al., 2014).

The present study focuses on the surface deformation associated with groundwater extraction, and its temporal evolution in the Bursa Plain in order to understand how surface subsidence evolves in response to changing aquifer and soil properties. We investigate this evolution by integrating SAR interferometry and geological and hydrogeological data in order to shed insight on the underlying processes governing subsidence. We have restricted our study to the Bursa Plain located in the east of Bursa basin along the northern slope of the Uludag Mount (Figures 6.1, 6.2a). We use PS-InSAR time series with data acquired between 2014 and 2017. The observed subsidence signal is interpreted by comparison with spatiotemporal piezometric level variations in the aquifer, and analyzed in terms of local geological conditions. We first describe the tectonic and geological setting of the study area, and other morphological characteristics. After summarizing the Sentinel-1 SAR data used and its processing methodologies employed, we present mean velocity fields obtained from different viewing geometries, and their vertical components. Finally, we compare vertical InSAR velocity fields with hydrologic and geologic data in order to constrain the compressibility of the underlying aquifer that compacted due to reduction of water level. In addition, we apply visual interpretation on Landsat 8 images to better understand the relationship between subsidence and the spatial pattern of alluvial fans, bare lands, urban and agricultural areas and other land-use patterns.
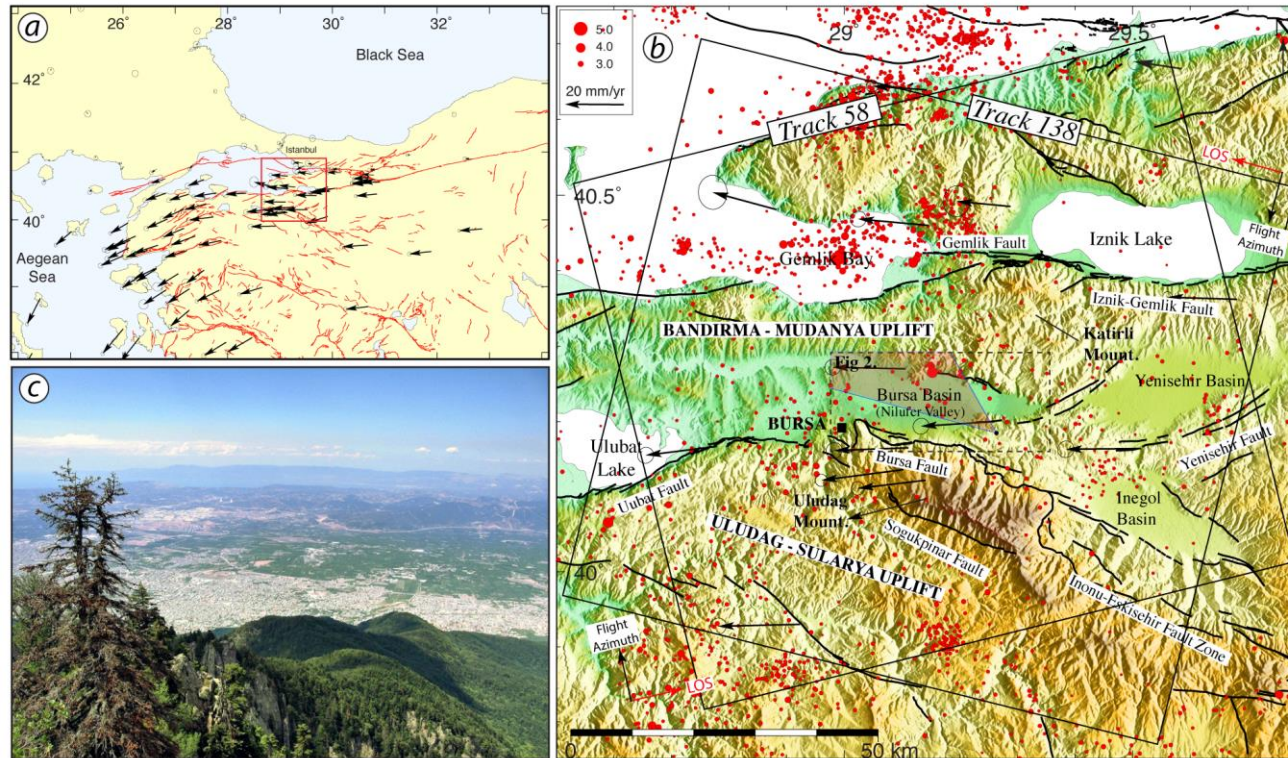
Figure 6.1 : Study area and Sentinel synthetic aperture radar data coverage used in the present study. (**a**) Map shows North-West of Turkey and the major active faults drawn in red (Emre et al., 2003) with GPS vector in a Eurasia fixed reference frame (Reilinger et al., 2006). Plain red box highlights the region of Interest. (**b**) The shaded topography is given by the Shuttle Radar Topography Mission (SRTM) along the South of Marmara Region with major active faults.. Red dots depict the seismicity of the region since 2005 (KOERI-RETMC). Black arrows are GPS velocities with respect to fixed Eurasia (Reilinger et al., 2006). (**c**) The view of the Bursa Plain, looking to the North from the hills of Mount Uludag (Wikipedia- Available Online: https://tr.wikipedia.org/wiki/Bursa (accessed on 26 November 2018)).

6.2 Study Area

Located on the northern slope of the Mount Uludag (2543 masl) in North-West Turkey, the city of Bursa is one of the most industrialized and populated cities of Turkey with a population of 2.9 million inhabitants (TUIK - Available online: http://www.tuik.gov.tr/HbGetirHTML.do?id=27587) The Bursa plain is located 5 km to the north of the city and bordered by the Mount Uludag to the south and Mount Katirli to the north (Figure 6.1b). The plain has a high agricultural potential due to its rich underground aquifer and surface water resources, and its fertile soils (Serbetci 2018). Consequently, the plain exerts considerable impact upon Turkey's national economy, which led to rapid population inflow over the past few decades and consequently rapid expansion of industrial and residential zones into the fertile Bursa plain that was used previously mainly for farming activities.

The southern branch of the North Anatolian Fault (NAF) in the Marmara region controls the long-term tectonic evolution of the Bursa basin. The segments of the NAF in the region cause a roughly N-S extension, which in turn produces the Bursa Plain in the eastern part of E-W trending Bursa-Gönen Depression, bounded to the north and the south by the Bandirma-Mudanya and Uludag-Sularya uplifts (Figure 6.1b). These highlands consist of metamorphic and granitic basement rocks and are dominant morphological features along the southern branch of the NAF (Selim et al., 2013-a). Tectonic models suggest that the depressed areas opened as pull-apart basins and are filled with Upper Pleistocene fluvial terrace and alluvial fan materials (Figure 6.2b) (Selim et al., 2013-b). The Quaternary sediments thicken to the south and exceeds 300 m in the Bursa basin (Imbach, 1997), suggesting that the deposition pattern is tectonically controlled (Selim et al., 2013-a). The alluvium has high transmissivity in comparison with the Neogene deposits surrounding the Nilufer Valley (Bursa Environment Project Report on Hydrology and Water Quality Modelling, 1991). The city of Bursa is located within the area with the highest probability of strong earthquakes in Turkey (i.e. first-degree seismic hazard zone). The seismicity of the region is controlled mainly by active faults such as the Gemlik Fault, Geyve-Iznik Fault Yenisehir Fault, Bursa Fault and the Inonu-Eskisehir Fault Zone (Gok & Polat, 2012). Bursa also hosts thermal springs that follow major fracture zones (Eisenlohr, 1995).
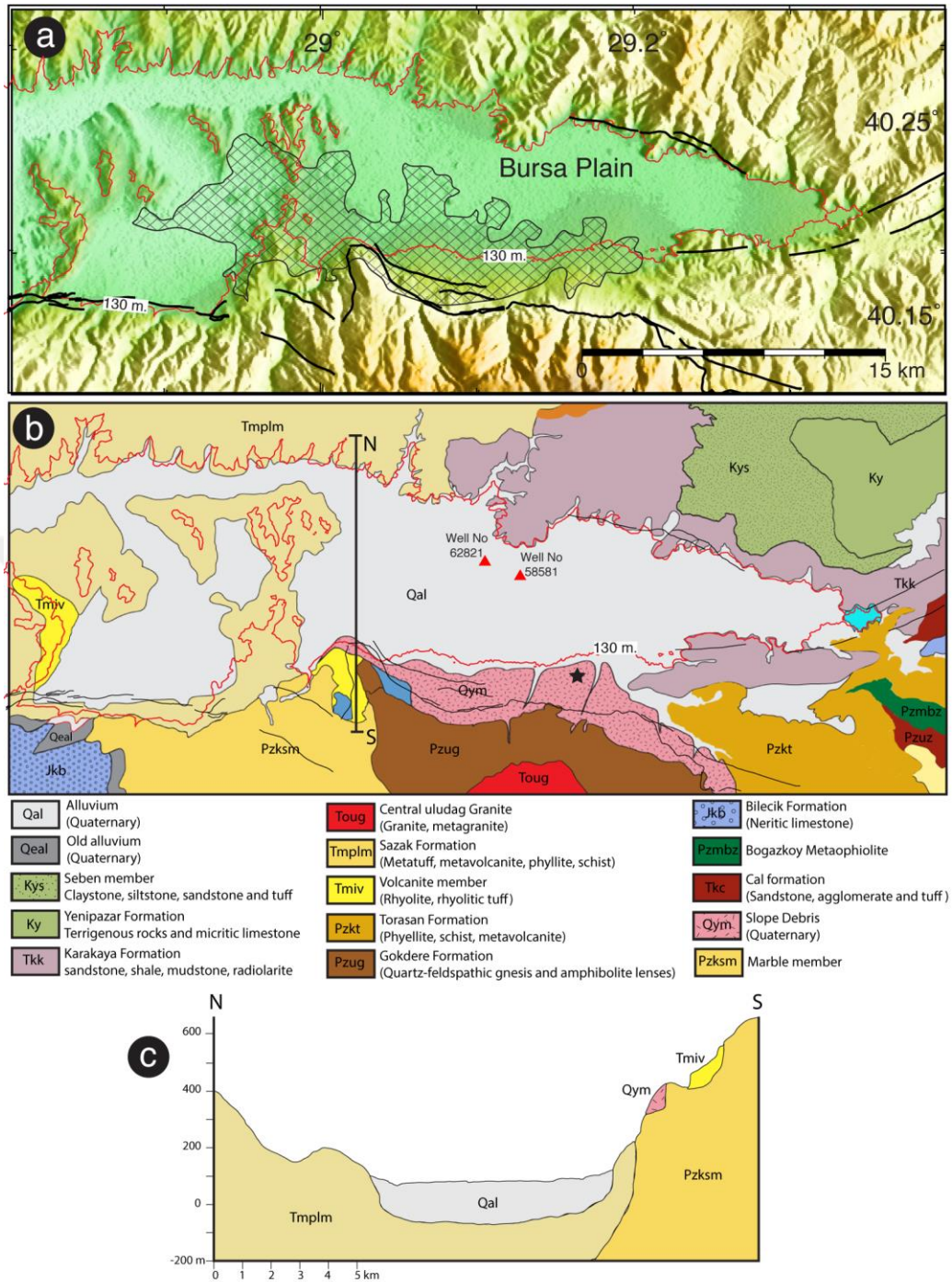
Figure 6.2 : (**a**) Topographic view of the Bursa Plain. Elevation contours at 130 m surrounding the Bursa Plain shown in red solid line. Shaded area shows the extent of urbanization for Bursa. (**b**) Geological map of the study area simplified from MTA – Turkey General Directorate of Mineral Research and Exploitation 1/100000 scale geology map. Red triangles show the locations of wells (well #58581 and 62821). The black star shows the area to which InSAR velocities are referenced. (**c**) North-South geological cross section of the Nilufer Valley from (Bursa Environment Project Report on Hydrology and Water Quality Modelling, 1991).

79

6.3 Datasets

We use C-band (5. GHz, ~6 cm wavelength) Sentinel 1 A/B TOPS images to map the rate and spatial distribution of subsidence in the Bursa Basin. The data used in the present study consist of two datasets with short temporal coverage, under the assumption of a linear model of the deformation during the observation period. 105 images were acquired on ascending *Track 58* between 21 October 2014 and 28 December 2017, and 96 images were acquired on descending *Track 138* between 8 November 2014 and 4 December 2017. The study area is fully covered by all tracks.
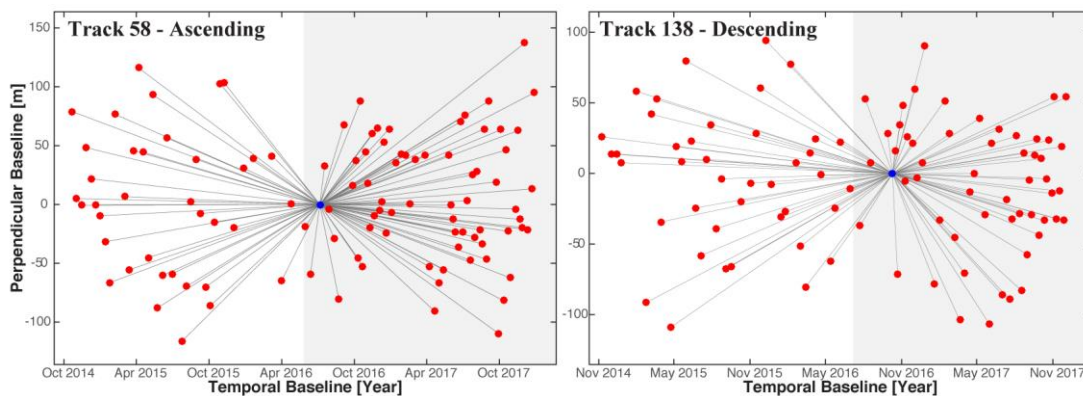
Figure 6.3 : Baseline configurations of single-master interferograms. Baseline versus time plots for Sentinel ascending tracks 58 and descending track 138 used in this study with red dots donating the time of image acquisitions. The blue dots indicate the master image used as a reference for each track. Gray lines connect pairs (interferograms). Temporal resolution of the dataset increased from 12 days until mid-2016 to 6 days after it, after the launch and starting of operational phase of Sentinel 1B indicated in gray zone.

6.4 Deformation Decomposition of Sentinel -1 Data

The subsidence signal in the Bursa plain is covered entirely by Sentinel – 1 data from two different orbits and therefore only two different viewing geometries are available. Consequently, we can only retrieve two of the three components of the actual deformation vector. We decomposed the mean PS-InSAR line-of-sight velocity fields into east-west and vertical components. We assumed that the north-south displacement was negligible because the near polar orbits of the SAR satellites produce a low sensitivity to the north-south component of displacement (Wright et al., 2004). In a first step, we resampled the mean line-of-sight velocities for the

80

ascending and descending tracks onto a 100x100 m regular grid, which is used as input for displacement decomposition. We used a nearest neighbor procedure to resample the persistent scatterer pixels that are within 200 m of the center of each grid nodal point. In a second step, we selected all the pixels that exist in both the ascending and descending tracks. Before decomposition, we transformed InSAR mean velocity fields of both tracks into the same reference frame using the reference point considered as a stable area (black star in Figure 6.4). In a last step, the line-of-sight velocity fields were decomposed into two components: the horizontal component along the azimuth look direction ($\mathbf{d_{hor}}$) and the vertical component ($\mathbf{d_{ver}}$) were computed, taking into account the local incidence angle of the satellite view by solving the following equation (Fialko et al., 2001; Motagh et al., 2017)

$$\begin{pmatrix} d_{asc} \\ d_{dsc} \end{pmatrix} = \begin{pmatrix} \cos\theta_{asc} & -\cos\alpha_{asc}\sin\theta_{asc} \\ \cos\theta_{dsc} & -\cos\alpha_{dsc}\sin\theta_{dsc} \end{pmatrix} \begin{pmatrix} d_{ver} \\ d_{hor} \end{pmatrix}, \tag{6.1}$$

where $\boldsymbol{\theta_{asc}}$ and $\boldsymbol{\theta_{dsc}}$ represent the local incidence angles and $\boldsymbol{\alpha_{asc}}$ and $\boldsymbol{\alpha_{dsc}}$ are the satellite heading angles of Sentinel-1's ascending and descending modes, respectively.

6.5 Results

6.5.1 InSAR-derived land subsidence maps

Figure 6.4 shows the InSAR-derived mean line-of-sight velocity fields calculated from PS-InSAR time series analysis for the Bursa Plain. There is no ground-truth data (i.e. data collected at the ground surface) available in the study area. Consequently, the mean phase values for both tracks are initially used for referencing the velocity fields in time series analysis. The area in the south of the subsiding basin located within the shaded polygon representing the extension of the Bursa city was chosen as the reference area because it is considered as a stable area (black star in Figure 6.3). Referencing has been performed by considering the local incidence angles.

The main subsidence signal is located in the eastern part of the basin, to the northeast of the metropolitan city of Bursa. The velocity fields of both tracks exhibit similar spatial patterns. This similarity suggests that the LOS velocities show mostly vertical deformation with negligible horizontal motion and atmospheric effects. In order to

assess the consistency between ascending and descending orbits, we perform an inter-comparison of the line of-sight displacement rates (Section 6.6.1). Differences in the locations of the subsidence patterns is also discussed below. While near-urban areas (marked by shaded polygon) have high density of PS points, such points are scarce in the basin due to dense vegetation coverage and higher deformation rates.
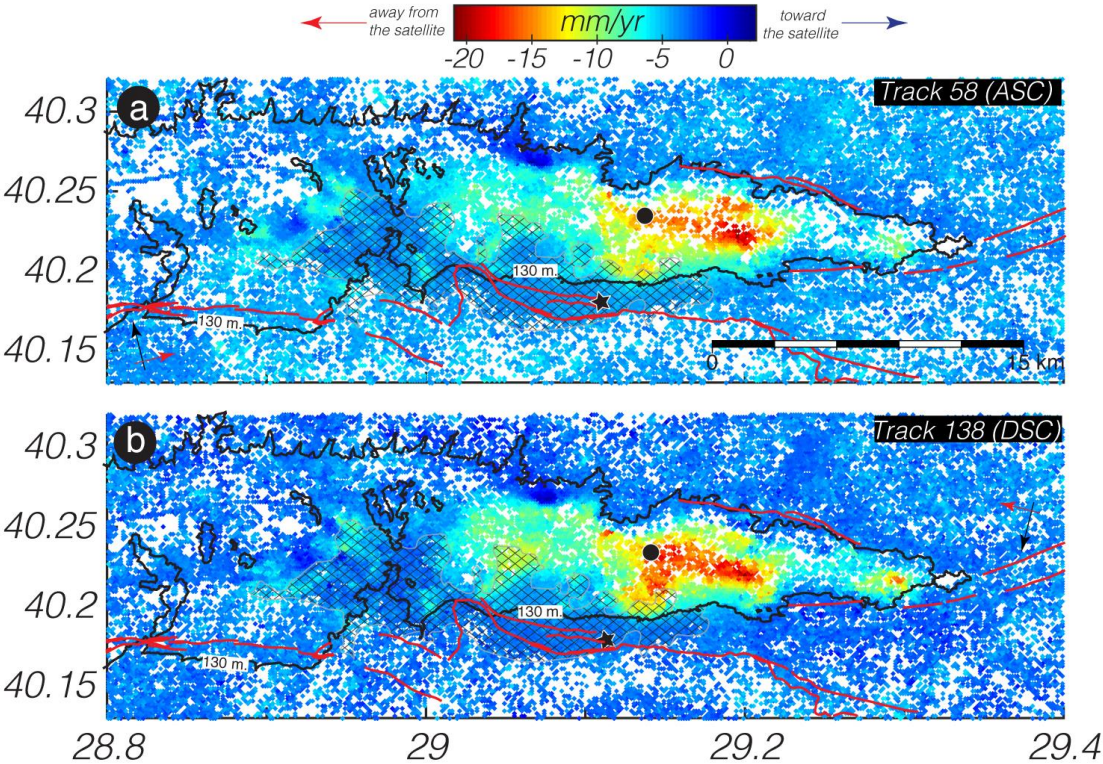
Figure 6.4 : Line-of-sight (LOS) velocity maps from Sentinel 1A/B time-series analysis for the time period 2014-2017. Positive velocities (cold colors) represent stable areas and displacement of the ground toward the satellite and negative velocities (warm colors) indicate displacement away from the satellite. Average line-of-sight velocity (**a**) on Sentinel ascending track 58, and (**b**) on Sentinel descending track 138. Elevation contours at 130 m around the subsiding Bursa Plain are shown in black solid lines. Shaded area shows building stock of Bursa city. The mean velocity value of the PS-InSAR points within the solid black point is used later to illustrate the temporal evolution of the subsidence (Figure 6.8). It is referenced to the mean value of PS–InSAR points within the black solid star, considered as a stable area.

The spatial distribution of subsidence rates for the period 2014-2017, obtained from the vertical component of the average yearly subsidence rate, are shown in Figure 6.5c. Figure 6.5c shows that the city of Bursa, which is settled on the northwest slope of the Uludag Mountain, is not affected by the subsidence. The maximum subsidence rate at the center of the depression is ~25 mm/yr. Comparison shows that the shape

and the location of the subsidence pattern agree with the agricultural zone whose activity relies heavily on groundwater exploitation.
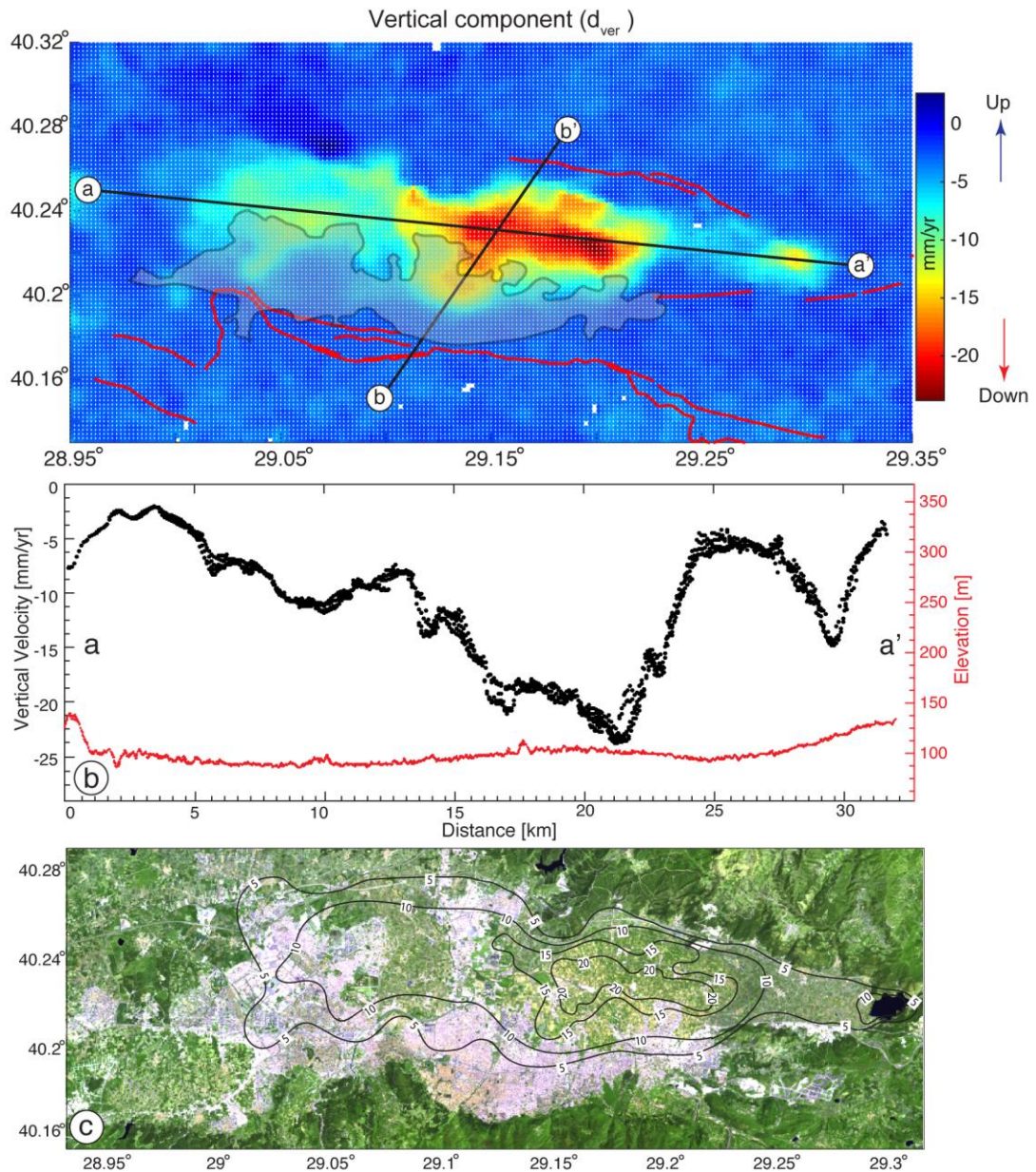
Figure 6.5: Decomposition of LOS displacement from Sentinel data for the time period 2014-2017 to vertical component. (**a**) Vertical mean velocity map. The warm colors represent the land subsidence relative to the reference point. Contour maps for certain elevations are superimposed onto the vertical velocity field map. The shaded area shows Bursa city. (**b**) Cross section showing vertical deformation rates in black and altitude in red taken from East-West a-a' profile. (**c**) 5 mm/yr interval contour maps superimposed onto the Landsat 8 image of April 23, 2018 in RGB combination of band 7, band 6 and band 4. Agriculture areas appear in shades of light green and yellow during the growth season and are located where the subsidence is the highest. Urban areas are in white, gray or light purple color (Focareta et al., 2015).

6.6 Discussion

6.6.1 Impact of the looking geometry on self-consistency checking between the ascending and descending InSAR observations
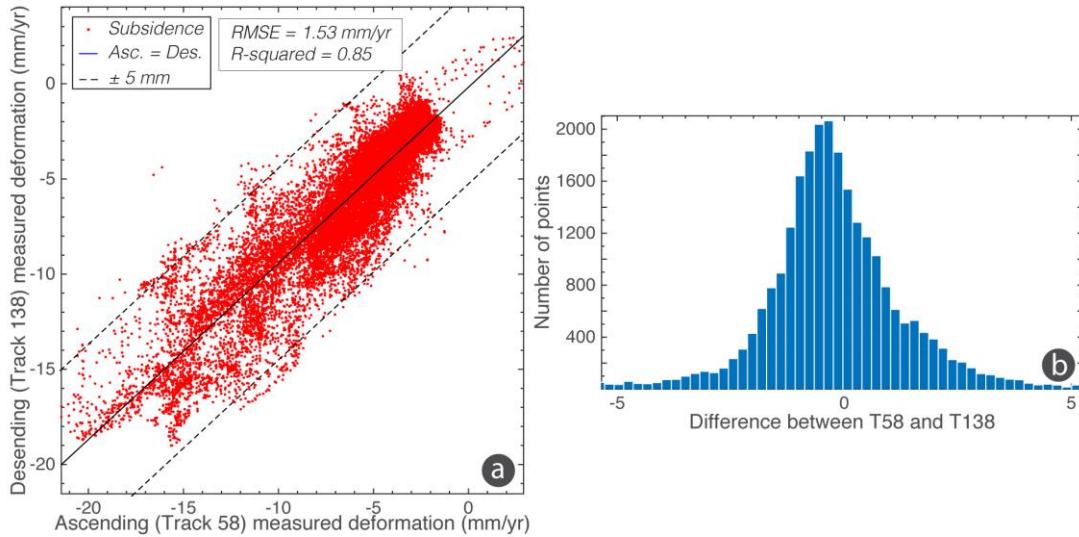
Figure 6.6: Quantitative comparison of the line-of-sight displacement rates between ascending and descending tracks. (**a**) Correlation between the point measurements. (**b**) Differences analysis between T58 Ascending and T138 Descending tracks.

Figure 6.6 shows the correlation between the point measurements within the region of interest. In order to show the self-consistency between InSAR measurements, we first quantitatively assess the consistency of InSAR mean velocity measurements calculated from the two different Sentinel 1A/B datasets for the subsidence area in the Bursa plain and its surrounding region. An inter-comparison of the line-of-sight displacement rate in this area is performed using a two-step procedure. In the first step, the mean velocity fields are resampled to a grid of 100x100 m to minimize the error of geo-localization (spatial mismatch between measurements). In the second step, we selected all pixels in the localized deforming areas that are common to the pair of overlapping tracks. Then, we compare the distribution of the subsidence rates for both tracks. We find a root-mean-square value of 1.53 mm/yr and the coefficient of determination (R^2) is close to 0.85. These values indicate that the two subsidence patterns (mean velocity) obtained from the different datasets are correlated with each other. This agreement demonstrates that the deformation obtained from both datasets

84

exhibits similar linear motions between 2014 and 2017, lending confidence to the subsidence patterns and amplitude determined by these datasets.

Comparison of the deformation rates between ascending and descending InSAR measurements of the same or different sensors is a common practice for quantitatively checking the consistency of measurements. The observed differences could stem from insufficient acquisitions, georeferencing uncertainty, seasonal biases, long temporal gaps, different temporal coverage and most importantly, different looking geometries. In order to show the impact of the looking geometry on the observed differences of the land subsidence induced by a single point source, we simulated a simple subsidence depression (Figure 6.7a).
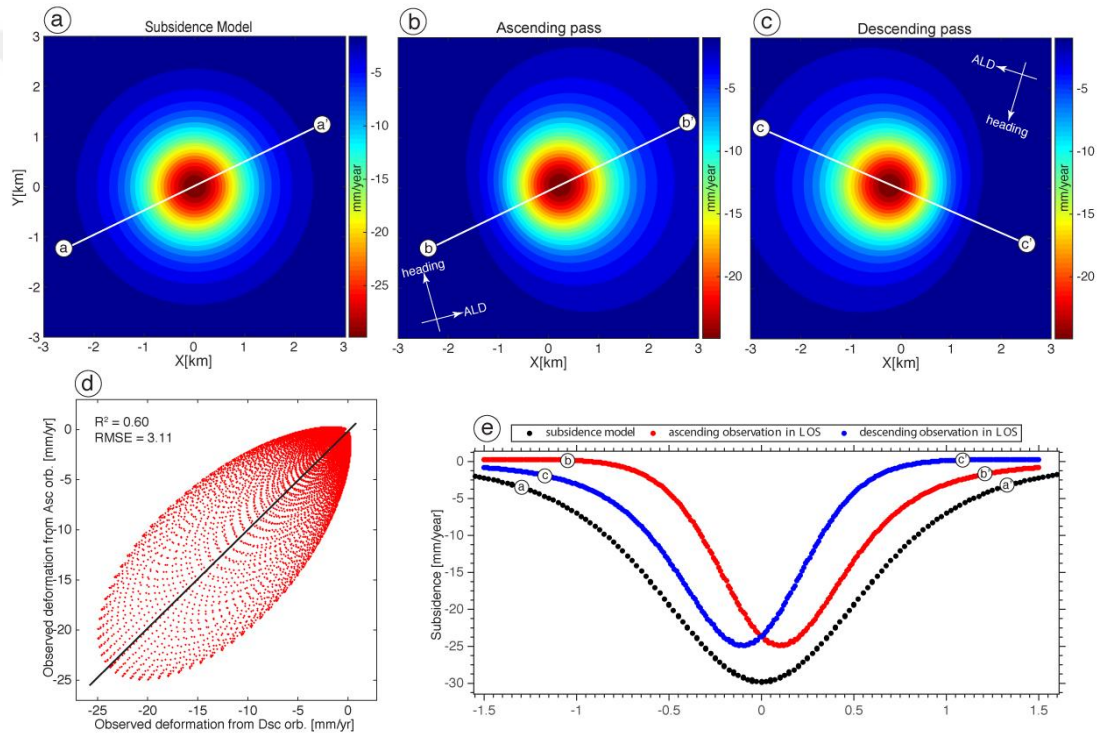
Figure 6.7 : Effect of the looking geometry on the InSAR observations. (**a**) Simulated subsidence model induced by a single point source. (b) Ascending observation. (**c**) Descending observation. (**d**) Comparison of deformation rates observed from ascending and descending orbits. (**e**) Cross section of the subsidence observations along the azimuth look directions (ALD).

When this synthetic subsidence signal is observed with an incidence angle of $\mathbf{37.5}^{\circ}$, considered as a mean incidence angle for Sentinel 1, and a heading angle of $\mathbf{-13.5}^{\circ}$ for ascending orbit, and $\mathbf{-166.5}^{\circ}$ for descending orbit, the deformation pattern depends on the looking geometry of the sensor (Figure 6.7b and 6.7c). The maximum subsidence value moves away from the center along the azimuth look directions

between the ascending and descending tracks. This deformation of the idealized subsidence pattern is giving a large dispersion and low correlation between the ascending and descending tracks due to the dispersion of the data points around the line of best fit.

6.6.2 Water table variations and InSAR time series

Using piezometric measurements, we can better constrain the geologic processes that produce the observed subsidence. Agricultural activity that relies significantly on irrigation contributes to the groundwater depletion in aquifer systems of fine-grained sediments (Castelazzi et al., 2016). Ground-truth monitoring, satellites (Catelaazzi et al., 2018), InSAR (Béjar-Pizarro et al., 2016), GPS (Liu et al., 2018) and numerical modeling have been utilized to understand the spatiotemporal variations of groundwater depletion. Many studies have shown that InSAR-derived subsidence patterns agree with water budgets (Castellazzi et al., 2016; Chaussard et al., 2014; Calo et al. 2017). Exploitation of aquifers decreases the groundwater volume, causing land subsidence that can be detected by InSAR. Given the lithological and hydrogeological data throughout the subsiding basin, we can constrain the amount of the groundwater depletion from the inversion of InSAR-derived land subsidence.

The Bursa ground water basin has a surface area of 208 km^2. In order to investigate the correlation between groundwater exploitation and surface deformation, we compared the temporal variation of the water table measured in two wells available for the period of InSAR measurements (2014-2017) in LOS component that fall within 1 km radius around the wells. As seen in Figure 8, the decreasing trend between InSAR-derived deformation rate and water level data show good agreement. The pressure head variations of both wells show ~10 and ~20 m of water level decrease in mid-2017. These decreases overlap the trend of ground deformation.
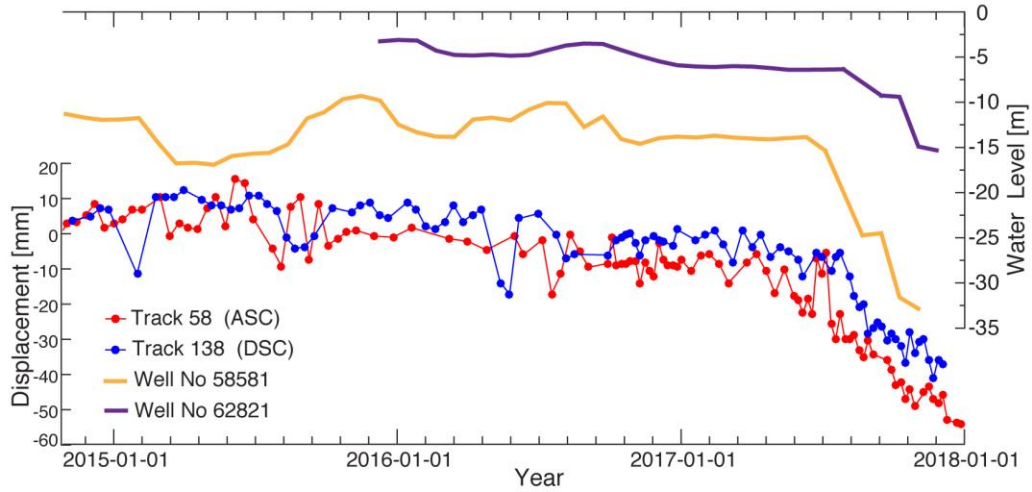
Figure 6.8 : Temporal evolution of the subsidence of selected points within the black solid circle shown in Figure 6.4. Locations of well #58581 and #62821 are shown in Figure 6.2b. The blue line represents the displacement measured using T138 descending data, and red line represents the displacement measured using the T58 ascending Sentinel 1 data. Orange and purple lines represent water level at wells #58581 and #62821, respectively.

6.6.4 Compressibility of the aquifer in the Bursa plain

We now use the subsidence measured using the InSAR data and the level of water in the two wells (Figure 8) to estimate the compressibility of the aquifer that compacted due to water level decrease. The compressibility of an aquifer is defined as $\alpha = -\frac{dV_T}{d\sigma_e V_T}$, where V_T is the total volume of the aquifer and $d\sigma_e$ is the change in effective pressure in the aquifer (Hiscock & Bense 2009). We consider an increment of drawdown dV_w due to pumping of water in the aquifer. This drawdown induces an increment of subsidence at the surface, dS_u related to a compaction of the reservoir such that $\frac{dV_T}{V_T} = -\frac{dS_u}{b}$, where b is the thickness of the aquifer taken here as equal to 50 m. The change in effective pressure is $d\sigma_e = \rho_w g dV_w$, where $\rho_w = 1000$ kg.m^{-3} and g=9.81 m.s^{-2} are the density of water and the constant of gravity, respectively. The compressibility can be calculated as $\alpha = \frac{dS_u}{b \rho g dV_w}$. Applied to the Bursa basin and considering a unit surface area of 1 m^2, the Figure 6.8 shows that the drawdown increased in the range $9 < dV_w < 18$ m during the year 2017 and the surface subsidence increased in the range $0.035 < dS_u < 0.045$ m. As a result, the compressibility is in the range $0.5 \cdot 10^{-6} < \alpha < 2 \cdot 10^{-6}$ Pa^{-1}, which falls in the range of values typical for clay and sand sediments (Hiscock & Bense 2009). These

values are in agreement with the alluvium sedimentary filling of the Bursa basin (see geological map in Figure 6.2).

6.6.3 Lithological and tectonic control over land subsidence

Alluvial deposits in the Bursa plain area in which we observe subsidence are made of Neogene and Quaternary deposits (Selim et al., 2013-a). The thickness of these deposits varies from 50 to 300 m (Imbach, 1997). They are composed of predominantly soft clay and loose silt and sand (Selim et al., 2013-b) Such highly compressible lithological units are more vulnerable to land subsidence due to groundwater extraction. We estimate a maximum vertical subsidence rate of 25 mm/yr for the 2014 – 2017 time period in the Bursa plain. The spatial distribution of subsidence is characterized by an east-west oriented, elongated, elliptical shape of deformation along the axis of the Bursa plain, in areas where agricultural activities are well developed (Figure 6.5c). The vertical mean velocity field shows the subsidence to be on the order of 10 mm/yr in the part of the alluvial plain that extends for approximately 200 km^2 in the northern part of the Bursa city center. Within this subsidence zone, an oblong subsidence lobe (red in Figure 6.5a) is subsiding the fastest, sinking at a maximum rate of 25 mm/yr. The overall subsidence pattern in the study area shows very clear correlation with the shape of the basin, agricultural land use and geological units of the study area. These correlations suggest that the land deformation is partially controlled by lithology and human activities. The fact that the pattern of subsidence mimics the shape of the basin may suggest that the alluvial thickness of the basin impacts the subsidence rate.

Similar to our results, Kutoglu et al. (2014) have detected a subsidence signal in the Bursa plain between 2007 and 2010 and interpreted this signal as due to movements of the active faults that in the long term have created the Bursa basin. However, the subsidence rate of 10.9 cm/yr proposed by Kutoglu et al. (Kutoglu et al., 2014) is too high to be attributed to tectonic movements such as shallow (surface creep) or lower crust deep creep. This is because, as shown with GPS velocities in Figure 1b, N-S horizontal velocity difference between the northern and southern shoulders of the Bursa basin that may cause aseismic slip on the basin boundary faults is negligible or too small to be detected in a few decades. As seen in Figure 6.9, there are no differences in the InSAR velocity across both the southern and northern boundary

faults, confirming that there is no shallow creep on them. A deep creep would cause subsidence in the entire basin, not only in the alluvial plain. Therefore, these observations and the strong correlation between the subsidence rate and ground water level suggest that most of the current subsidence detected in the past years is most likely due to decline of ground water table, rather than tectonic movements. Extremely high subsidence rate for the period of 2007-2010 was probably due to either droughts or over pumping of the aquifer.
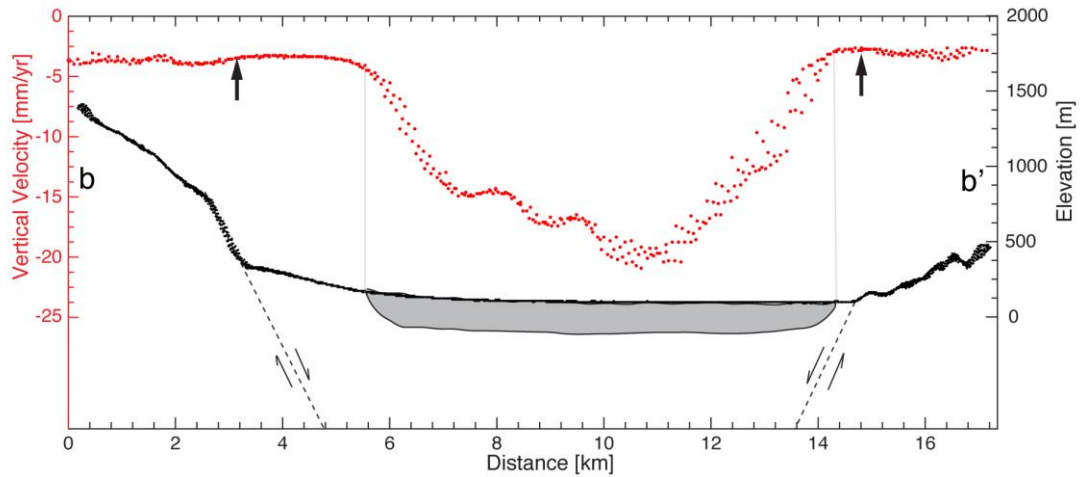
Figure 6.9 : Cross section showing vertical deformation rates in red and altitude in black taken from b-b' profile shown in Figure 6.5-a.

6.7 Conclusion

The population of Bursa is increasing due to the city's growing economy. This growing population is causing rapid urbanization; heavy land use and land cover change. This rapid land development is forcing the land use to change from agricultural to more urban activities on the city's outskirt and hinterland. We have detected ground subsidence in the northern part of Bursa at rates ranging from 5 to ~25 mm/yr in an area of 200 km^2 from Sentinel 1-A/B images collected between 2014 and 2017.

In order to investigate the possible correlation between detected InSAR-derived land subsidence and water level change, we analyzed piezometric records between 2014 and 2017. These records show a water table drop in mid 2017 that correlates with the InSAR-derived time series. The coincidence of the InSAR subsidence spatial extent with the alluvial deposits suggests a hydrogeological control of the Bursa plain on the observed subsidence. The eastern part of the subsiding area is sinking at a

maximum rate of ~25 mm/yr where agricultural activities rely significantly on groundwater extraction. The spatial pattern of subsidence reveals that the urban environment is not yet affected by significant subsidence. All these observations indicate that the subsidence in Bursa plain is due to excessive groundwater extraction, not tectonic motions

7. CONCLUSIONS AND PERSPECTIVES

In this dissertation, we measured and analyzed the temporal and spatial characteristics of small surface deformation signals in northwest Turkey by integrating SAR interferometry, GNSS measurements, geological and hydrogeological data and ground-truth observations such as creep meter data to discuss their origin and driving mechanisms. Throughout three case studies in this work, we highlighted the ability of InSAR time series analysis to understand different geophysical phenomena such as aseismic slip and subsidence and natural hazard events. More specifically, this work addresses three cases that include the present-day behavior of shallow aseismic slip along the 1999 Izmit rupture on the North Anatolina Fault, subsidence induced by different factors in the urban areas and sedimentary basins near Istanbul and south of the Marmara Sea.

Improving our understanding of shallow creeping continental faults and its role on the earthquake cycle requires detailed obsersarvations and analyses of slow deformation related to active faulting. In the first case study, we have investigated the spatial and temporal distribution of aseismic shallow creep along the 1999 Izmit earthquake using Sentinel 1 A-B and TerraSAR-X images in both ascending and descending viewing geometries from 2011 to 2017 in combination with GPS measurements. Our results show a very clear discontinuity in the LOS velocity fields obtained from each SAR dataset, particularly along the central segment of the 1999 rupture. During the InSAR and GPS observation period, the fault creep occurs at an average rate of 8 mm/year in the shallow uppermost 5 km of the crust that extends from Gulf of Izmit in the west to the Sapanca Lake in the east. Considering the frictional heterogeneities and simple planar geometry of the 1999 rupture that can favor the supershear velocities, there is a spatial coincidence between the presently creeping section and the 1999 supershear velocity fault section. This coincidence along the very linear geometry of the Izmit-Sapanca Lake and Sapanca Lake-Akyazi segments of the rupture may suggest that fault geometry partly control the creeping behaviour. Geological maps shows that the maximum surface creep puts in contact

Quaternary alluvial deposits in the central depression of the Izmit basin, north of the fault, and Eocene volcanic units south of the fault that can also favor the aseismic behaviour in the region. Our results obtained from high temporal resolution of Sentinel-1 data also reveals the existence of temporal accelerations of the creep rate, with the detection of a one-month burst of creep in December 2016, with an amplitude of ~10 mm, consistent with creepmeters observations. We also find a prominent subsidence on the hanging wall of the Golcuk Normal Fault ruptured during the Izmit earthquake. The velocity discontinuity along this oblique normal fault could be due to subsidence in the basin or shallow afterslip on the fault.

The current rate of energy release due to aseismic slip in the upper shallow layer of the fault is about 30-40 % of the annual tectonic loading rate. Therefore, we conclude that a significant strain accumulation remains in this region of the NAF.

In the second case study, we presented the surface displacements associated with ground subsidence along several selected sites in the terrestrial and coastal region of Istanbul. Spanning almost twenty-five years of satellite radar observations, we computed InSAR time-series of multiple satellites data in order to provide insights into the potential hazards induced by local soil conditions and human activities. Using the PS-InSAR technique, abundant number of time-coherent pixels were obtained over six different sites in Istanbul. The most prominent and clearly visible subsidence signals have been detected over the western part of Istanbul consistently in all the frames. The spatio-temporal variability of the ground displacement was measured over the last 25 years in Avcilar that suffered extensive damage during the 1999 Izmit earthquake and along the Haramidere valley where a long-lasting landslide history has been reported. The time series analysis in this region reveals that Haramidere valley banks are undergoing ground vertical subsidence at a rate of 10 ± 2 mm/yr. Another subsidence area has been reported along the Ayamama river banks, made of shallow alluvial deposits due to the local substratum consolidation process, at a rate of 10 ± 1.8 mm/yr. The surface area affected by this subsidence is shrinking gradually with time following the restoration of river and stream system in 2008. The inter-comparison of PS-InSAR measurements from different satellite sensors spanning different periods for the western part of Istanbul shows that the correlation between the mean velocity fields is very high between 1992-2011 and decreases with time due to spatio-temporal change of the ground deformation.

Sentinel-1A/B InSAR measurements acquired between 2014 and 2017 show that reclaimed lands in both European (Yenikapi reclamation area) and Asian (Maltepe reclamation area) coastlines of Istanbul underwent significant subsidence of up to 8 ± 1.3 mm/yr as a result of primary consolidation processes of the filling material.

Over all, we conclude that during the interseismic period human-driven changes produce a more significant control on the coastal subsidence in Istanbul than natural factors. In future studies, such high-resolution SAR data over the very dense urban area of Istanbul could help monitoring continuously the urbanized areas suffering from land subsidence. With this purpose, future plans include the processing of high-resolution X-band sensors COSMO-Skymed and TerraSAR-X datasets to better quantify the surface settlement and reveal the underlying causes of these settlements in order to provide more complete data to public organizations in charge of sustainable urban policies and hazard mitigation.

As a final case study, we present a detailed map of the subsidence of Bursa Plain in southern Marmara region of Turkey using Sentinel 1-A/B images collected between 2014-2017, and reconsider the origin of the subsidence, previously proposed to result from tectonic motions in the region. We investigate the possible correlation between InSAR-derived land subsidence and water level changes between 2014 and 2017. These records show a water table drop in mid 2017 that correlates with velocity change in the InSAR-derived time series. This observation and the coincidence of the InSAR subsidence spatial extent with the alluvial deposits suggests a hydrogeological control on the subsidence of the Bursa plain. The eastern part of the subsiding area is sinking at a maximum rate of ~25 mm/yr where agricultural activities rely significantly on groundwater extraction. The spatial pattern of subsidence reveals that the urban environment is not yet affected by significant subsidence. All these observations indicate that the subsidence in Bursa plain is due to excessive groundwater extraction, not to tectonic motions.

REFERENCES

Abdikan, S., Arıkan, M., Sanli, F.B., and Çakir, Z., (2014). Monitoring of coal mining subsidence in peri-urban area of Zongundak city (NWTurkey) with persistent scatterer interferometry using ALOS-PALSAR. *Environ. Earth Sci.*, 71, 4081–4089.

Adam, N., Kampes, B., Eineder, M., Worawattanamateekul, J., and Kircher, M., (2003). The development of a scientific permanent scatterer system, *ISPRS Hannover Workshop, Inst.* for *Photogramm. and Geoinf.*, Hannover, Germany.

Altay, C., and Sav H. (1991). Continuous creep measurement along the North Anatolian Fault zone, *Bulletin of Geological Congress*, Turkey, 6, 77–84.

Akaike, H. (1974). A new look at the statistical model identification, *IEEE Trans. Autom. Control*, *19*, 716-723.

Akarvardar, S., Feigl, K.L., and Ergintav, S. (2009). Ground deformation in an area later damaged by an earthquake: monitoring the Avcilar district of Istanbul, Turkey, by satellite radar interferometry, *Geophys. J. Int.*, *178*, 976–988.

Akyol, N., Akıncı, A., and Eyidogan, H. (2002). Site amplification of S-waves in Bursa City and its vicinity, Northwestern Turkey: comparison of different approaches, *Soil Dynamics and Earthquake Engineering*, *7*, 579-587.

Ambraseys, N. (1970). Some characteristic features of the Anatolian fault zone. *Tectonophysics*, *9*, 143-165.

Aslan, G., Cakır, Z., Ergintav, S., Lasserre, C., and Renard, F. (2018). Analysis of Secular Ground Motions in Istanbul from a Long-Term InSAR Time-Series (1992–2017). *Remote Sensing*, *10*, 408.

Aslan, G., Cakir, Z., Lasserre, C., and Renard, F. (2019). Investigating Subsidence in the Bursa Plain, Turkey, Using Ascending and Descending Sentinel-1 Satellite Data, *Remote Sensing*, *11*, 85.

Aslan G, Lasserre C, Cakir Z, Ergintav S., Cetin S., Dogan U., Bilham R., and Renard F. (2019). Shallow creep along the 1999 Izmit earthquake's rupture (Turkey) from high temporal resolution interferometric synthetic-aperture radar data (2011-2017). *Journal of Geophysical Research, Solid Earth*.

Avouac, J.-P. (2015), From Geodetic Imaging of Seismic and Aseismic Fault Slip to Dynamic Modeling of the Seismic Cycle, *Annual Review of Earth and Planetary Sciences*, *43*, 233-271.

Aytun, A. (1982), Creep measurements in the Ismetpasa region of the North Anatolian fault zone, In *Multidisciplinary Approach to Earthquake Prediction*, edited by A. M. Isikara and A. Vogel, 279–292, Friedr. Vieweg and Sohn, Braunshweig/Wiesbaden.

Baer, G., Magen, Y., Nof, R.N., Raz, E., Lyakhovsky, V., and Shalev, E. (2018). InSAR Measurements and Viscoelastic Modeling of Sinkhole Precursory Subsidence: Implications for Sinkhole Formation, Early Warning, and Sediment Properties. *J. Geophys. Res. Earth Surf.*, *123*, 678–693.

Bamler, R. and Hartl, P. (1998). Synthetic aperture radar interferometry. Inv, Prob., 15:R1-R54

Barka, A., Akyuz, H.S., Sunal, G., Cakir, Z., Dikbas, A., Yerli, B., … and Armijo, R. (2002). The surface rupture and slip distribution of the 17 August 1999 Izmit earthquake (M 7.4), North Anatolian Fault, *Bulletin of the Seismological Society of America*, *92(1),* 43–60.

Barra, A., Solari, L., Béjar-Pizarro, M., Monserrat, O., Bianchini, S., Herrera, G., Crosetto, M., Sarro, R., González-Alonso, E., Mateos, R.M., Ligüerzana, S., López, C., and Moretti, S. (2017). A Methodology to Detect and Update Active Deformation Areas Based on Sentinel-1 SAR Images. *Remote Sens.*, *9*, 1002.

Béjar-Pizarro, M., Guardiola-Albert, C., García-Cárdenas, R. P., Herrera, G., Barra, A., López Molina, A., Tessitore, S., Staller, A., Ortega-Becerril, A.J., and García-García, R. P. (2016). Interpolation of GPS and geological data using InSAR deformation maps: Method and application to land subsidence in the alto guadalentín aquifer (SE Spain). *Remote Sensing*, *8(11),* 965.

Béjar-Pizarro, M., Ezquerro, P., Herrera, G., Tomás, R., Guardiola-Albert, C., Ruiz Hernández, J.M., Fernández Merodo, J.A., Marchamalo, M., and Martínez, R. (2017). Mapping groundwater level and aquifer storage variations from InSAR measurements in the Madrid aquifer, Central Spain, *J. Hydrol.,* 678–689.

Bekaert, D. P. S., R. J. Walters, T. J. Wright, A. J. Hooper, and D. J. Parker (2015). Statistical comparison of InSAR tropospheric correction techniques, *Remote Sens. Environ.*, *170*, 40–47.

Berardino, P., Fornaro, G., Lanari, R., and Sansosti, E. (2002). A new algorithm for surface deformation monitoring based on small baseline differential SAR interferograms, *Geosci. and Remote Sensing, IEEE Trans. on, 40*, 2375-2383.

Biggs, J., Wright, T., Lu, Z., and Parsons, B. (2007). Multi-interferogram method for measuring interseismic deformation: Denali Fault, Alaska. *Geophysical Journal International*, *170(3),* 1165-1179.

Biggs, J., Bürgmann, R., Freymueller, J. T., Lu, Z., Parsons, B., Ryder, I., ... and Wright, T. (2009). The postseismic response to the 2002 M 7.9 Denali Fault earthquake: constraints from InSAR 2003–2005, *Geophys. J. Int.*, *176*, 353-367.

Biggs, J., Robertson E., and Cashman K. (2016). The lateral extent of volcanic interactions during unrest and eruption, *Nature Geoscience*, *9*, 308-311.

Bilham, R. (1989). Surface slip subsequent to the 24 November 1987 Superstition Hills, California, earthquake monitored by digital creep-meters, *Bulletin of the Seismological Society of America, 79*, 424–450.

Bilham, R., Ozener, H., Mencin, D., Dogru, A., Ergintav, S., Cakir, Z., Aytun, A., and Aktug, B. (2016). Surface creep on the North Anatolian Fault at Ismetpasa, Turkey, 1944-2016, *Journal of Geophysical Research: Solid Earth*, *121(10),* 7409-7431.

Bitelli, G., Bonsignore, F., and Unguendoli, M. (2000), Levelling and GPS networks to monitor ground subsidence in the Southern Po Valley. *J. Geodyn., 30*, 355–369.

Bol, E., Arel, E., Önalp, A., Sert, S., and Ozocak A. (2010). Liquefaction of silts: the Adapazari criteria, *Bull Earthquake Eng*, 8, 859.

Bouchon, M., Bouin, M. P., Karabulut, H., Toksoz, M. N., Dietrich, M., and Rosakis, A. J. (2001). How fast is rupture during an earthquake? New insights from the 1999 Turkey earthquakes, *Geophysical Research Letters*, *28*, 2723–2726.

Bouchon, M., Karabulut, H., Bouin, M.-P., Schmittbuhl, J., Vallée, M., Archuleta, R., Das, S., Renard, F., and Marsan, D. (2010). Faulting characteristics of supershear earthquakes, *Tectonophysics*, *493(3-4),* 244-253.

Brown, L. G. (1992). A survey of image registration techniques. *ACM computing surveys (CSUR), 24(4),* 325-376.

B.U. KOERI-RETMC (Boğaziçi University Kandilli Observatory and Earthquake Research Institute - Regional Earthquake-Tsunami Monitoring Center) – Earthquake Catalogue. Retrieved 20 October, 2018, from http://www.koeri.boun.edu.tr/sismo/2/earthquake-catalog/

Burak, S., and Kucukakca, E. (2015). Impact of Land Reclamation on the Coastal Areas in Istanbul, *EGU General Assembly Conference 2015*, Vienna, Austria, 12-17 April.

Burford, R. O., and Harsh, P. W. (1980). Slip on the San Andreas fault in central California from alignment array surveys, *Bulletin of the Seismological Society of America*, *70*, 1223–1261.

Bursa Environment Project Report on Hydrology and Water Quality Modelling, (1991). Institute of Hydrology, Wallingford, Oxon, OX10 8BB, December 1991, p. 14.

Brunori, C.A., Bignami, C., Albano, M., Zucca, F., Samsonov, S., Groppelli, G., Norini, G., Saroli, M., and Stramondo, S. (2015). Land subsidence, Ground Fissures and Buried Faults: InSAR Monitoring of Ciudad Guzmán (Jalisco, Mexico). *Remote Sens.*, *7*, 8610-8630.

Burgmann, R., Schmidt D., Nadeau R., d'Alessio, M., Fielding, E., Manaker, D., McEvilly, T., and Murray, M. H. (2000). Earthquake potential along the northern Hayward fault, *Science*, *289*, 1178–1182.

Burgmann, R., Rosen, P. A., and Fielding, E. J. (2000). Synthetic aperture radar interferometry to measure Earth's surface topography and its deformation. *Annual review of earth and planetary sciences*, *28(1),* 169-209.

Burgmann, R., and Thatcher W. (2013), Space geodesy: A revolution in crustal deformation measurements of tectonic processes. *In The Web of Geological Sciences: Advances, Impacts and Interactions*: Ed. ME Bickford, 397-430, GSA Spec. Pap. 500. Boulder, CO: GSA.

Burgmann, R. (2018). The geophysics, geology and mechanics of slow fault slip. *Earth and Planetary Science Letters*, *495*, 112-134.

Cakir, Z., de Chabalier, J. B., Armijo, R. Meyer, B., Barka, A., and Peltzer, G., (2003a). Coseismic and early postseismic slip associated with the 1999 Izmit earthquake (Turkey), from SAR interferometry and tectonic field observations, *Geophysical Journal International*, *155*, 93-110.

Cakir, Z., Barka, A., de Chabalier, J-B., Armijo, R., and Meyer, B. (2003b). Kinematics of the November 12, 1999 (Mw=7.2) Düzce earthquake deduced from SAR interferometry, *Turkish Journal of Earth Sciences*, *12*, 105-118.

Cakir, Z., Akoglu, A.M., Belabbes, S., Ergintav, S., and Meghraoui, M. (2005). Creeping along the Ismetpaşa section of the North Anatolian Fault (Western Turkey): Rate and extent from InSAR, *Earth Planet Sc. Lett.*, *238*, 225-234.

Cakir, Z., Ergintav, S. Ozener, H. Dogan, U., Akoglu, A. M., Meghraoui, M., and Reilinger R., (2012). Onset of aseismic creep on major strike-slip faults, *Geology*, *40*, 1115–1118.

Calderhead, A. I., Therrien, R., Rivera, A., Martel, R., and Garfias, J. (2011). Simulating pumping-induced regional land subsidence with the use of InSAR and field data in the Toluca Valley, Mexico. *Advances in Water Resources*, *34(1),* 83-97.

Caló, F., Notti, D., Galve, J. P., Abdikan, S., Görüm, T., Pepe, A., and Balik Şanli, F. (2017). Dinsar-based detection of land subsidence and correlation with groundwater depletion in Konya Plain, Turkey. *Remote Sensing*, *9(1),* 83.

Caló, F., Abdikan, S., Gorum, T., Pepe, A., Kilic, H., and Sanli, F.B. (2015). The space-borne SBAS-DInSAR technique as a supporting tool for sustainable urban policies: The case of Istanbul Megacity, Turkey, *Remote Sens., 7*, 16519–16536.

Carpenter, B. M., Marone, C., and Saffer, D. M. (2011). Weakness of the San Andreas Fault revealed by samples from the active fault zone, *Nature Geoscience*, *4(4),* 251–254.

Carnec, C., and Delacourt, C. (2000). Three years of mining subsidence monitored by SAR interferometry, near Gardanne, France. *J. Appl. Geophys., 43*, 43–54.

Castellazzi, P., Martel, R., Rivera, A., Huang, J., Pavlic, G., Calderhead, A. I, Chaussard, E., Garfias, J., and Salas, J. (2016). Groundwater depletion in Central Mexico: Use of GRACE and InSAR to support water resources management. *Water Resources Research*, *52(8)*, 5985-6003.

Castellazzi, P., Martel, R., Galloway, D. L., Longuevergne, L., and Rivera, A. (2016). Assessing groundwater depletion and dynamics using GRACE and InSAR: potential and limitations. *Groundwater*, *54(6)*, 768-780.

Castellazzi, P., Longuevergne, L., Martel, R., Rivera, A., Brouard, C., and Chaussard, E. (2018). Quantitative mapping of groundwater depletion at the water management scale using a combined GRACE/InSAR approach. *Remote Sensing of Environment*, 2018, *205*, 408-418.

Cavalié, O., Lasserre, C., Doin, M. P., Peltzer, G., Sun, J., Xu, X., and Shen, Z. K. (2008). Measurement of interseismic strain across the Haiyuan fault (Gansu, China), by InSAR. *Earth and Planetary Science Letters*, *275(3-4)*, 246-257.

Champenois, J., Fruneau, B., Pathier, E., Deffontaines, B., Lin, K.C., and Hu, J.C. (2012). Monitoring of active tectonic deformations in the Longitudinal Valley (Eastern Taiwan) using Persistent Scatterer InSAR method with ALOS PALSAR data, *Earth Planet Sc. Lett.*, *337*, 144-155.

Chang, W. Y., Wang, C. T., Chu, C. Y., and Kao, J. R. (2012). Mapping geo-hazard by satellite radar interferometry. *Proceedings of the IEEE*, *100(10)*, 2835-2850.

Changxing, S., Dian, Z., Lianyuan, Y., Bingyuan, L., Zulu, Z., and Ouyang, Z. (2007). Land subsidence as a result of sediment consolidation in the Yellow River Delta. *Journal of Coastal Research*, 173-181.

Chaussard, E., Wdowinski, S., Cabral-Cano, E., and Amelung, F. (2014). Land subsidence in central Mexico detected by ALOS InSAR time-series. *Remote Sens. Environ., 140*, 94–106.

Chen, J., Wu, J., Zhang, L., Zou, J., Liu, G., Zhang, R., and Yu, B. (2013). Deformation trend extraction based on multi-temporal InSAR in Shanghai, *Remote Sens., 5*, 1774–1786,

Crosetto, M., Arnaud, A., Duro, J., Biescas, E., and Agudo, M. (2003). Deformation monitoring using remotely sensed radar interferometric data, In Proc. *11th FIG Symposium* on *Deformation Measurements*, Patras Univ., Santorini, Greece, 25 May 2003.

Crosetto, M., Devanthéry, N., Monserrat, O., Barra, A., Cuevas-González, M., Mróz, M., ... and Crippa, B., (2018). A Persistent Scatterer Interferometry Procedure Based on Stable Areas to Filter the Atmospheric Component. *Remote Sensing*, *10(11)*, 1780.

Colesanti, C., Ferretti, A., Prati C., and Rocca, F. (2003). Monitoring landslides and tectonic motion with the Permanent Scatterers Technique. *Eng. Geol*, *68*, 1–14,

Colesanti, C., and Wasowski, J. (2004). Satellite SAR interferometry for wide-area slope hazard detection and site-specific monitoring of slow landslides. In Proceedings *Ninth International Symposium on Landslide*s, Rio de Janeiro, Brazil, 28 June – 2 July 2004.

Colesanti, C., Ferretti, A., Novali, F., Prati, C., and Rocca, F. (2003). SAR monitoring of progressive and seasonal ground deformation using the permanent scatterers technique. *IEEE Trans. Geosci. Remote Sensing*, *41(7),* 1685-1701,

Colesanti, C., Ferretti, A., Prati, C., and Rocca, F. (2003). Monitoring landslides and tectonic motions with the permanent scatterer technique, *Engineering Geol., Spec. Issue Remote Sensing and Monitoring of Landslides, 68(1),* 3-14,

Colesanti, C., Ferretti, A., Locatelli, R., Novali, F., and Savio, G. (2003). Permanent scatterers: precision assessment and multi-platform analysis. *Int. Geosci. Remote Sensing Symp.*, Tolouse, France, 21-25 July 2003.

Cranswick E., Ozel O., Meremonte M., Erdik M., Safak E., Mueller C., Overturf D., and Frankel A. (2000). Earthquake damage, site response and building response in Avcılar, west of Istanbul, *Turkey, J Hous Sci Appl*, *24*, 85–96.

Curlander, J. and McDonough, R. N. (1991). Synthetic Aperture Radar: Systems and Signal Processing. Wiley, New York.

Dalgıç, S. (2004). Factors affecting the greater damage in the Avcılar area of Istanbul during the 17 August 1999 Izmit earthquake, *Bulletin of Engineering Geology and the Environment*, *63(3),* 221-232.

Dang, V.K., Doubre, C., Weber, C., Gourmelen, N., and Masson, F. (2014). Recent land subsidence caused by the rapid urban development in the Hanoi region (Vietnam) using ALOS InSAR data. *Nat. Hazards Earth Syst. Sci.*, *14*, 657.

De Michele M, Raucoules, D., Rolandone, F., Briole, P., Salichon J., Lemoine A., Salichon, J., and Aochi, H. (2011). Spatio-temporal evolution of surface creep in the Parkfield region of the San Andreas Fault (1993–2004) from synthetic aperture radar, *Earth Planetary Science Letters*, *308*, 1–2, 141–150

De Michele, M., Ergintav, S., Aochi, H., Raucoules, D. (2017). An L-band interferometric synthetic aperture radar study on the Ganos section of the north Anatolian fault zone between 2007 and 2011: Evidence for along strike segmentation and creep in a shallow fault patch. *PloS one*, 12(9), e0185422.

Dee, D. P., Uppala, S. M., Simmons, A. J., Berrisford, P., Poli, P., Kobayashi, S., ... and Bechtold, P. (2011). The ERA-Interim reanalysis: Configuration and performance of the data assimilation system. Quarterly Journal of the royal meteorological society, *137(656),* 553-597.

Del Soldato, M., Farolfi, G., Rosi, A., Raspini, F., and Casagli, N. (2018). Subsidence Evolution of the Firenze–Prato–Pistoia Plain (Central Italy) Combining PSI and GNSS Data. *Remote Sensing, 10*, 1146.

Deniz, R., Aksoy, A. Yalin, D., Seeger, H., and Hirsch O. (1993). Determination of crustal movement in Turkey by terrestrial geodetic methods, *Journal of Geodynamics*, *18(1-4),* 13–22.

Diao, F., Walter T., Solaro G., Wang R., Bonano M., Manzo M., Ergintav S., Zheng Y., Xiong X., and Lanari R. (2006). Fault locking near Istanbul: Indication of earthquake potential from InSAR and GPS observations, *Geophys. J. Int.*, *205(1),* 490–498.

Diao, F., Walter, T.R., Minati, F., Wang, R., Costantini, M., Ergintav, S., Xiong, X., and Prats-Iraola, P. (2016). Secondary Fault Activity of the North Anatolian Fault near Avcilar, Southwest of Istanbul: Evidence from SAR Interferometry Observations. *Remote Sens*., *8*, 846.

Dogan U., Oz D., and Ergintav S. (2012). Kinematics of landslide estimated by repeated GPS measurements in the Avcilar region of Istanbul, Turkey, *Stud. Geophys Geodyn.*, *57*, 217–232.

Duman, T.Y. (2004). İstanbul Metropolü Batısındaki (Küçükçekmece- Silivri-Çatalca Yöresi) Kentsel Gelişme Alanlarının Yerbilim Verileri. Maden Tetkik ve Arama Genel Müdürlügü(MTA) Özel Yayın Serisi – 3, Ankara.

Duman, T.Y., Can, T., Gokceoglu, C., and Nefeslioglu, H.A. (2005-a). Landslide susceptibility mapping of Cekmece area (Istanbul, Turkey) by conditional probability, *Hydrology and Earth System Sciences Discussions*, *2(1),* 155-208.

Duman, T.Y., Can, T., Ulusay, R., Keçer, M., Emre, Ö., Ateş, S. anf Gedik, I. A. (2005-b). Geohazard reconnaissance study based on geoscientific information for development needs of the western region of Istanbul (Turkey). *Environ. Geol., 4*, 871–888.

Einfalt, T., and Keskin, F. (2009). Analysis of the Istanbul Flood 2009, BALWOIS 2010 *Scientific Conference on Water Observation and Information System for Decision Support*. Ohrid, Republic of Macedonia.

Eisenlohr, Th. (1995). Die Thermalwässer der ArmutluHalbinsel (NW-Türkei) und deren Beziehung zu Geologie und aktiver Tektonik, (Doktoral Dissertation). ETH-Zürich, 11340.

Elachi, C. (1988). Spaceborne radar remote sensing: applications and techniques. New York, IEEE Press, 1988, 285.

Emre, O., Duman, T.Y., Ozalp, S., Elmaci, H., Olgun, S., and Saroglu, F., (2013). Active Fault Map of Turkey with and Explanatory Text, Ankara, Turkey, Special Publication Series-30. General Directorate of Mineral Research and Exploration, Ankara.

Eren, K. (1984). Strain analysis along the North Anatolian fault by using geodetic surveys, *Bulletin Géodésique*, *58 (2),* 137–149.

Ergin, M., Özalaybey, S., Aktar, M., and Yalcin, M.N. (2004) Site amplification at Avcılar, Istanbul. *Tectonophysics*, *391(1),* 335-346.

Ergintav, S., Demirbag, E., Ediger, V., Saatcilar, R., Inan, S., Cankurtaranlar, A., Dikbas, A. and Bas, M., (2001). Structural framework of onshore and offshore Avcilar, Istanbul under the influence of the North Anatolian Fault. *Geophysical Journal International*, *185 (1),* 93-105.

Ergintav, S., McClusky, S., Hearn, E., Reilinger, R., Cakmak, R., Herring, T., Ozener, H., Lenk, O., and Tari, E., (2009). Seven years of postseismic deformation following the 1999, M= 7.4 and M= 7.2, Izmit, Düzce, Turkey earthquake sequence. *Journal of Geophysical Research: Solid Earth*, 114(B7).

Ergintav, S., Reilinger, R., Çakmak, R., Floyd, M., Cakir, Z., Dogan, U., King, R., McClusky, S., and Özener, H., (2014). Istanbul's earthquake hot spots: Geodetic constraints on strain accumulation along faults in the Marmara seismic gap, *Geophysical Research Letters*, *41(16),* 5783–5788.

European Bank for Reconstruction and Development, (2018). Environmental and Social Impact Assessment for the Eurasia Tunnel Project Istanbul, Turkey. Volume 1. Sept. 2011. ERM Group. Retrieved 15 Oct., 2018, from http://www.ebrd.com/english/pages/project/eia/42163nts.pdf.

Evinemi, I. E., Adepelumi, A. A., and Adebayo, O. (2016). Canal structure subsidence investigation using ground penetrating radar and geotechnical techniques, *International Journal of Geo-Engineering, 7(1),* 9.

Eyidogan, H., (2006). Analysis of Micro-Seismicity of Istanbul Greater City Area and Active Faults. *In Proceedings of the International Workshop on "Comparative studies of the North Anatolian Fault (northwest Turkey) and the San Andreas Fault (southern California)"*. ITU, Istanbul, Turkey, Abstract book, 54.

Evseev, A., Asanov, V., Lomakin, I., and Tsayukov, A. (2018). Experimental and theoretical studies of undermined strata deformation during room and pillar mining. *In Geomechanics and Geodynamics of Rock Masses*; CRC Press: Boca Raton, FL, USA, 2, 985–990.

Ezquerro, P., Herrera, G., Marchamalo, M., Tomás, R., Béjar-Pizarro, M., and Martínez, R. A. (2014). quasi-elastic aquifer deformational behavior: Madrid aquifer case study. *J. Hydrol., 519*, 1192–1204.

Farr, T., Rosen, P., Caro, E., Crippen, R., Duren, R., Hensley, S., and Alsdorf, D. (2007). The shuttle radar topography mission. *Reviews of Geophysics*, *45(2).*

Fattahi, H., and Amelung F., (2016). InSAR observations of strain accumulation and fault creep along the Chaman Fault system, Pakistan and Afghanistan, *Geophysical Research Letters*, *43*, 8399–8406.

Fergason, K. C., Rucker, M. L., and Panda, B. B. (2015). Methods for monitoring land subsidence and earth fissures in the Western USA. *Proceedings of the International Association of Hydrological Sciences*, *372*, 361-366.

Ferretti, A., Prati, C., and Rocca, F. (2000). Nonlinear subsidence rate estimation using Permanent Scatterers in Differential SAR Interferometry, *IEEE Trans. Geosci. Remote Sens., 38*, 2202-2212.

Ferretti, A., Prati, C., and Rocca, F. (2001). Permanent scatterers in SAR interferometry, *IEEE Transactions on Geoscience and Remote Sensing*, *39*, 8–20.

Ferretti, A., Novali, F., Bürgmann, R., Hilley, G., and Prati, C. (2004). InSAR permanent scatterer analysis reveals ups and downs in San Francisco Bay area. Eos, *Transactions American Geophysical Union*, *85(34),* 317-324,

Ferretti, A., Colombo, D., Fumagalli, A., Novali, F., and Rucci, A. (2015) InSAR data for monitoring land subsidence: time to think big. *In Proceedings of the International Association of Hydrological Sciences, 372,* 331-334.

Fialko, Y. (2006), Interseismic strain accumulation and the earthquake potential on the southern San Andreas Fault system. *Nature*, *441(7096),* 968.

Fielding, E.J., Blom, R.G., and Goldstein, R.M. (1998). Rapid subsidence over oil fields measured by SAR interferometry. *Geophys. Res. Lett., 25*, 3215–3218.

Focareta, M., Marcuccio, S., Votto, C. and Ullo, S. L. (2015). Combination of Landsat 8 and Sentinel 1 data for the characterization of a site of interest. A Case Study: the Royal Palace of Caserta. *In 1rst International Conference on Metrology for Archaeology*, Benevento, Italy. 22 October, 2015.

Foreman-Mackey, D., Hogg, D. W., Lang, D., and Goodman, J. (2013). EMCEE: The MCMC hammer, *Publications of the Astronomical Society of the Pacific*, *125(925),* 306–312.

Froese, C.R., and Mei, S. (2008), Mapping and monitoring coal mine subsidence using LiDAR and InSAR. *In Proceedings of the GeoEdmonton2008*, Edmonton, AB, Canada, 21–24 September 2008,1127–1133.

Gabriel, A. K., Goldstein, R. M. and Zebker, H. A. (1989). Mapping small elevation changes over large areas: differential radar interferometry. *Journal of Geophysical Research: Solid Earth*, *94(B7),* 9183-9191.

Galloway, D. L., Hudnut, K. W., Ingebritsen, S. E., Phillips, S. P., Peltzer, G., Rogez, F. and Rosen, P. A. (1998). Detection of aquifer system compaction and land subsidence using interferometric synthetic aperture radar, Antelope Valley, Mojave Desert, California. *Water Resources Research*, *34(10),* 2573-2585.

Galve, J.P., Pérez-Peña, J.V., Azañón, J.M., Closson, D., Caló, F., Reyes-Carmona, C., Jabaloy, A., Ruano, P., Mateos, R.M., Notti, D., Herrera, G., Béjar-Pizarro, M., Monserrat, O. and Bally, P. (2017). Evaluation of the SBAS InSAR Service of the European Space Agency's Geohazard Exploitation Platform (GEP), *Remote Sens., 9*, 1291.

Ge, L., Ng, AH., Li, X., Abidin, H.Z. and Gumilar, I. (2014). Land subsidence characteristics of Bandung Basin as revealed by ENVISAT ASAR and ALOS PALSAR interferometry. *Remote sensing of Environment*, *154*, 46-60.

Gok, E. and Polat, O. (2012). An assessment of the seismicity of the Bursa region from a temporary seismic network. *Pure and Applied Geophysics*, *169(4),* 659-675.

Goodman, J., and Weare J. (2010). Ensemble samplers with affine invariance, *Communications in Applied Mathematics and Computational Science*, *5*, 65–80.

Gourmelen, N., Amelung, F., Casu, F., Manzo, M., and Lanari, R. (2007) Mining-related ground deformation in Crescent Valley, Nevada: Implications for sparse GPS networks. *Geophys. Res. Lett., 34*.

Hanssen, R.F. (2001). *Radar interferometry: data interpretation and error analysis,* Vol. 2. Springer Science & Business Media, 2001.

Harris, R. A. (2017), Large earthquakes and creeping faults, *Reviews of Geophysics*, *55*, 169–198.

Hearn, E.H., McClusky, S., Ergintav S., and Reilinger, R.E. (2009). Izmit earthquake postseismic deformation and dynamics of the North Anatolian Fault Zone, *Journal of Geophysical Research*, *114*, B08405.

Helgert, T., and Heidbach, O. (2010). Slip-rate variability and distributed deformation in the Marmara Sea fault system. *Nature Geoscience*, *3*, 132-136.

Herring, T.A., King, R.W., Floyd, M.A., McClusky, S.C. (2015). Introduction to GAMIT/GLOBK, Release 10.6, Massachusetts Institute of Technology, Cambridge.

Hetland, E. A., Simons, M., and Dunham, E. M. (2010). Post-seismic and interseismic fault creep I: Model description. *Geophysical Journal International*, *181(1),* 81-98.

Higgins, S.A., Overeem, I., Steckler, M.S., Syvitski, J.P., Seeber, L., and Akhter, S.H. (2014). InSAR measurements of compaction and subsidence in the Ganges-Brahmaputra Delta, Bangladesh. *J. Geophys. Res. Earth Surf.*, *119*, 1768–1781.

Hiscock, K. M., and Bense, V.F. (2009). Hydrogeology: principles and practice. John Wiley & Sons.

Hoffmann, J., Zebker, H., Galloway, D., and Amelung, F. (2001). Seasonal subsidence and rebound in Las Vegas Valley, Nevada, observed by synthetic aperture radar interferometry. *Water Resour. Res.*, *37*, 1551–1566.

Hooper, A., Segall, P., and Zebker, H. (2007). Persistent scatterer interferometric synthetic aperture radar for crustal deformation analysis, with application to Volcán Alcedo, Galápagos, *J. Geophys. Res., 112*, B07407.

Hooper, D., Coughlan, J., and Mullen, M. R. (2008-a). Structural Equation Modelling: Guidelines for Determining Model Fit. *The Electronic Journal of Business Research Methods*, *6*, 53-60.

Hooper, A. (2008-b). A Multi-temporal InSAR method incorporating both persistent scatterer and small baseline approaches, *Geophys. Res. Lett.*, *35*, L16.

Hooper, A., Bekaert, D., Spaans, K., and Arıkan M. (2011). Recent advances in SAR interferometry time series analysis for measuring crustal deformation, *Tectonophysics*, 514, 1-13.

Hu, X., Oommen, T., Lu, Z., Wang, T., and Kim, J.W. (2017). Consolidation settlement of Salt Lake County tailings impoundment revealed by time-series InSAR observations from multiple radar satellites. *Remote Sens. Environ*, *199-209*.

Hubert-Ferrari, A., Barka, A., Jacques, E., Nalbant, S.S., Meyer, B., Armijo, R., Tapponnier, P., and King G.J.P. (2000). Seismic hazard in the Marmara Sea region following the 17 August 1999 Izmit earthquake, *Nature*, *404*, 269-273.

Hussain, E., Wright, T. J., Walters, R. J., Bekaert, D., Hooper, A., and Houseman G. A. (2016). Geodetic observations of postseismic creep in the decade after the 1999 Izmit earthquake, Turkey: Implications for a shallow slip deficit, *Geophysical Research Letters, Solid Earth*, *121*, 2980–3001.

Hussain, E., Wright, T. J., Walters, R. J., Bekaert, D. P., Lloyd, R., and Hooper, A. (2018). Constant strain accumulation rate between major earthquakes on the North Anatolian Fault. *Nature Communications*, *9*.

Imbach, T. (1997). Deep groundwater circulation in the tectonically active area of Bursa, Northwest Anatolia, Turkey. *Geothermics*, *26(2),* 251-278.

Intrieri, E., Gigli, G., Nocentini, M., Lombardi, L., Mugnai, F., Fidolini, F. and Casagli, N. (2015). Sinkhole monitoring and early warning: An experimental and successful GB-InSAR application, *Geomorphology*, *241*, 304–314,

Ireland, R.L., Poland, J.F., and Riley, F.S. (1984). Land Subsidence in the San Joaquin Valley, California, as of 1980; US Geological Survey Professional, US Government Printing Office: Washington, DC, USA, 93.

Jolivet, R., Lasserre, C., Doin, M.-P., Guillaso, S., Peltzer, G., Dailu, R., and Sun, J. (2012) Shallow creep on the Haiyuan fault (Gansu, China), revealed by SAR interferometry, *Journal of Geophysical Research, 117 (B6).*

Jolivet, R., Lasserre, C., Doin, M. P., Peltzer, G., Avouac, J. P., Sun, J., and Dailu, R. (2013). Spatio-temporal evolution of aseismic slip along the Haiyuan fault, China: Implications for fault frictional properties, *Earth Planetary Science Letters, 377–378*, 23–33.

Jolivet, R., Simons, M., Agram, P. S., Duputel, Z., and Shen, Z.-K. (2015a). Aseismic slip and seismogenic coupling along the central San Andreas Fault, *Geophysical Research Letters*, *42*.

Jolivet, R., Candela, T., Lasserre, C., Renard, F., Klinger, Y., and Doin, M. P. (2015b). The burst-like behavior of aseismic slip on a rough fault: The creeping section of the Haiyuan Fault, China, *Bulletin of the Seismological Society of America,* 105(1), 480–488.

Jouanne, F., Audemard, F. A., Beck, C., Van Welden, A., Ollarves, R., and Reinoza, C. (2011). Present-day deformation along the El Pilar Fault in eastern Venezuela: Evidence of creep along a major transform boundary, *Journal of Geodynamics, 51(5),* 398–410.

Joyce, K. E., Belliss, S. E., Samsonov, S. V., McNeill, S. J., and Glassey, P. J. (2009). A review of the status of satellite remote sensing and image processing techniques for mapping natural hazards and disasters. *Progress in Physical Geography, 33(2),* 183-207.

Kaduri, M., Gratier, J., Renard, F., Cakir, Z., and Lasserre, C. (2017). The implications of fault zone transformation on aseismic creep: example of the North Anatolian Fault, Turkey. *Journal of Geophysical Research,* 4208-4236.

Kaduri, M., Gratier, J.-P., Lasserre, C., Çakir, Z., and Renard, F. (2018) Quantifying the Partition Between Seismic and Aseismic Deformation Along Creeping and Locked Sections of the North Anatolian Fault, Turkey. *Pure and Applied Geophysics.* 1-29

Kampes, B. M. (2005). Displacement Parameter Estimation Using Permanent Scatterer Interferometry, (Doctoral Dissertation), Delft Univ. of Technol., Delft, Netherlands.

Kampes, B., and Stefania, U. (1999) Doris: The Delft Object-Oriented Radar Interferometric Software. *In Proceedings of the 2nd International Symposium on Operationalization of Remote Sensing*, Enschede, The Netherlands, 16–20 August 1999.

Kaneko, Y., Fialko, Y., Sandwell, D. T., Tong, X., and Furuya, M. (2013). Interseismic deformation and creep along the central section of the North Anatolian fault (Turkey): InSAR observations and implications for rate-and-state friction properties, *Journal of Geophysical Research, 118*, 316–331.

Khakim, M. Y. N., Tsuji, T., and Matsuoka, T. (2014). Lithology-controlled subsidence and seasonal aquifer response in the Bandung basin, Indonesia, observed by synthetic aperture radar interferometry. *International Journal of Applied Earth Observation and Geoinformation*, *32*, 199-207,

Khoshmanesh, M., and Shirzaei, M. (2018). Multiscale Dynamics of Aseismic Slip on Central San Andreas Fault. *Geophysical Research Letters, 45*.

Kilic, H., Ozener, P.T., Yildirim M., Ozaydin, K., and Adatepe, S. (2005). Evaluation of Kucukcekmece region with respect to soil amplification. *In Proceedings of the International Conference on Soil Mechanics and Geotechnical Engineering*, Osaka, Japan, 12-16 September 2005.

Kim, S.W., Wdowinski, S., Dixon, T.H., Amelung, F., Kim, J.W., and Won, J.S. (2010). Measurements and predictions of subsidence induced by soil

consolidation using persistent scatterer InSAR and a hyperbolic model. *Geophys. Res. Lett.*, *37*.

Kim, S.W., Wdowinski, S., Dixon, T.H., Amelung, F., Won J.S., and Kim, J.W. (2008). InSAR-based mapping of the surface subsidence in Mokpo City, Korea, using JERS-1 and ENVISAT SAR data, *Earth Planets Space*, *60*, 453-461.

King, R. W., and Bock Y. (2004). Documentation of the MIT GPS Analysis Software: GAMIT, Mass. Inst. of Technol., Cambridge, Mass.

Klein, E., Duputel, Z., Masson, F., Yavasoglu, H., and Agram, P. (2017). Aseismic slip and seismogenic coupling in the Marmara Sea: What can we learn from onland geodesy?. *Geophysical Research Letters*, 44(7), 3100-3108.

Koeri, (2000). The earthquake activities of the Marmara Region between 1990 and 2000, Bogazici Univ Kandilli Obs. Earth. Res. Inst.

Komuscu, A.I., and Celik, S. (2013). Analysis of the Marmara flood in Turkey, 7-1-September 2009: an assessment from hydrometerological perspective. *Nat. Hazards*, *66*, 781-808.

Konca, A.O., LePrince, S., Avouac, J-P., and Helmberger, D.V. (2010). Rupture process of 1999, Mw 7.1 Düzce earthquake from joint analysis of SPOT, GPS, InSAR, strong-motion and teleseismic data: A supershear rupture with variable rupture velocity, *Bulletin of the Seismological Society of America, 100(1),* 267-287.

Kutoglu, H. S., Kemaldere, H., Deguchi, T., and Berber, M. (2014). Discovering a pull-apart basin using InSAR in Bursa, Turkey. *Natural Hazards*, *71(1),* 871-880.

Lanari, R., Mora, O., Manunta, M., Mallorquí, J.J., Berardino, P., and Sansosti. E. (2004). A Small Baseline DIFSAR Approach for Investigating Deformations on Full Resolution SAR Interferograms. *IEEE Trasnactions on geoscience and remote sensing*, *42 (7),* 1377-1386.

Lienkaemper, J. J., Galehouse, J. S., and Simpson, R. W. (2001). Long-term monitoring of creep rate along the Hayward fault and evidence for a lasting creep response to 1989 Loma Prieta earthquake, *Geophysical Research Letters*, *28*, 2269–2272.

Liu, Y., and Lapusta, N. (2008). Transition of mode II cracks from sub-Rayleigh to intersonic speeds in the presence of favorable heterogeneity, *Journal of the Mechanics and Physics of Solids*, *56*, 25-50.

Liu, R., Zou, R., Li, J., Zhang, C., Zhao, B., and Zhang, Y. (2018). Vertical Displacements Driven by Groundwater Storage Changes in the North China Plain Detected by GPS Observations. *Remote Sensing*, *10(2),* 259.

Liu, G., Jia, H., Nie, Y., Li, T., Zhang, R., Yu, B., and Li, Z. (2014). Detecting subsidence in coastal areas by ultrashort-baseline TCPInSAR on the time series of high-resolution TerraSAR-X images. *IEEE Trans. Geosci. Remote Sens.*, *52*, 1911–1923.

López-Quiroz, P., Doin, M. P., Tupin, F., Briole, P., and Nicolas, J. M. (2009). Time series analysis of Mexico City subsidence constrained by radar interferometry. *Journal of Applied Geophysics*, *69(1),* 1-15.

Luo, Q., Perissin, D., Zhang, Y. and Jia, Y. (2014). L- and X-band multi-temporal InSAR analysis of Tianjin subsidence, *Remote Sens.*, *6*, 7933–7951,

Marone, C. (1998). Laboratory-derived friction laws and their application to seismic faulting, *Annual Review of Earth and Planetary Sciences*, *26(1),* 643–696.

Massonnet, D., Holzer, T., and Vadon, H. (1997). Land subsidence caused by the East Mesa geothermal field, California, observed using SAR interferometry. *Geophys. Res. Lett.*, *24*, 901–904.

Massonnet, D., Feigl, K., Rossi M. and Adrangna F. (1994). Radar Interferometric mapping of deformation in the year after The Landers Earthquake, *Nature*, *369(6477),* 227-230.

Massonnet, D., and Feigl, K. L. (1998). Radar interferometry and its application to changes in the Earth's surface. *Reviews of geophysics*, *36(4),* 441-500.

Massonnet, D. and Rabaute, T. (1993). Radar interferometry: limits and potential. *IEEE Transactions on Geoscience and Remote Sensing*, *31(2),* 455-464.

Maurer, J., and Johnson, K. (2014). Fault coupling and potential for earthquakes on the creeping section of the central San Andreas fault, *Journal of Geophysical Research, Solid Earth, 119*, 4414–4428.

Meade, B. J., Klinger, Y., and Hetland, E. A. (2013). Inference of multiple earthquake-cycle relaxation timescales from irregular geodetic sampling of interseismic deformation. *Bulletin of the Seismological Society of America*, *103(5),* 2824-2835.

Meremonte, M., Ozel O., Cranswick E., Erdik M., Safak E., Overturf D., Frankel A., and Holzer T. (1999). Damage and site response in Avcılar, west of Istanbul, Eds. Aykut B., The 1999 Izmit and Duzce Earthquake. Preliminary Result 1999, 265–267.

Michel, R., and Avouac, J. P. (2002). Deformation due to the 17 August 1999 Izmit, Turkey, earthquake measured from SPOT images, *Journal of Geophysical Research, 107(B4),* 2062.

Motagh, M., Hoffmann, J., Kampes, B., Baes, M., and Zschau, J. (2007). Strain accumulation across the Gazikoy-Saros segment of the North Anatolian Fault inferred from Persistent Scatterer Interferometry and GPS measurements. *Earth and Planetary Science Letters*, *255(3-4),* 432-444.

Motagh, M., Shamshiri, R., Haghshenas Haghighi, M., Wetzel, H.U., Akbari, B., Nahavandchi, H., Roessner, S. and Arabi, S. (2017). Quantifying groundwater exploitation induced subsidence in the Rafsanjan plain, southeastern Iran, using InSAR time-series and in situ measurements. *Eng. Geol., 218*, 134–151.

Moore, D. E., and Rymer, M. J. (2007). Talc-bearing serpentinite and the creeping section of the San Andreas fault, *Nature*, *448*, 795–797.

Moore, D. E., and Lockner, D. A. (2013). Chemical controls on fault behavior: Weakening of serpentinite sheared against quartz-bearing rocks and its significance for fault creep in the San Andreas system, *Journal of Geophysical Research Solid Earth*, *118*, 1–13.

Nishimura, T., Matsuzawa, T., and Obara, K. (2013). Detection of short-term slow slip events along the Nankai Trough, southwest Japan, using GNSS data. *Journal of Geophysical Research: Solid Earth*, *118(6),* 3113-3125.

Ozener, H., Dogru, A., and Turgut, B. (2012). Quantifying aseismic creep on the Ismetpasa segment of the North Anatolian Fault Zone (Turkey) by 6 years of GPS observations, *Journal of Geodynamics*, *67(7),* 72–77.

Okada, A. (1953). Land deformation of the neighbourhood of Muroto Point after the Nankaido great earthquake in 1946. *Bull. Earthq. Res. Inst. Univ*. Tokyo, 31, 169-177.

Okay, A.I., Satır, M., Tuysuz, O., Akyuz, S., and Chen, F. (2001). The tectonics of the Strandja Massif: late Variscan and mid-Mesozoic deformation and metamorphism in the north Aegean. *Int. J. Earth Sci.*, *90*, 217–233.

Okuda, T. (1950). On the mode of the vertical land deformation accompanying the great Nankaido earthquake 1946. *Bull. Geogr. Surv. Inst*, 2(1), 37-59.

Ozel, O., Cranswick, E., Meremonte, M., Erdik, M., and Safak, E. (2002). Site effects in Avcilar, west of Istanbul, Turkey, from strong and weak motion data. *Bulletin of the Seismological Society of America*, *92(1),* 499-508.

Ozgul, N., Üner, K., Akmeşe, İ., Bilgin, İ., Kokuz, R., Özcan, İ. and Tekin, M. (2005). İstanbul il alanının genel jeoloji özellikleri. İstanbul Büyükşehir Belediyesi Deprem ve Zemin İnceleme Müdürlüğü, 2005, Istanbul, Turkey, 79.

Ozcan, O., and Musaoglu, N. (2010). Vulnerability analysis of floods in urban areas using remote sensing and GIS, In Proceedings of the 30th EARSeL *Symposium: Remote Sensing for Science, Education and Culture*, Paris, France, May 2010, 31.

Ozmen, B. (2000). Damage investigation of 17 August 1999 Izmit Earthquake, Turkish Earthquake Foundation Press, Istanbul, Turkey, 2000, 140.

Pacheco-Martínez, J., Cabral-Cano, E., Wdowinski, S., Hernández-Marín, M., Ortiz-Lozano, J. Á., and Zermeño-de-León, M. E. (2015). Application of insar and gravimetry for land subsidence hazard zoning in aguascalientes, mexico. *Remote Sensing*, *7(12),* 17035-17050.

Parsons, T. (2004). Recalculated probability of M7 earthquakes beneath the Sea of Marmara, Turkey, *Journal of Geophysical Research*, *109*, B05304.

Perissin, D., and Ferretti, A. (2007). Urban-target recognition by means of repeated spaceborne SAR images. *IEEE Transactions on Geoscience and Remote Sensing*, *45(12),* 4043-4058.

Plant, G.W., and Covil, C.S., (1998). Hughes Site Preparation for the New Hong Kong International Airport, Thomas Telford, 1998.

Poland, J.F. (1984). Guidebook to Studies of Land Subsidence Due to Ground-Water Withdrawal; UNESCO: Paris, France.

Pousse-Beltram, L., Pathier, E., Jouanne, F., Vassallo, R., Reinoza, C., Audemard, F., Doin, M.P., and Volat, M. (2016). Spatial and temporal variations in creep rate along the El Pilar fault at the Caribbean-South American plate boundary (Venezuela), from InSAR, *Journal of Geophysical Research, Solid Earth,* 121.

Radiguet, M., Cotton, F., Vergnolle, M., Campillo, M., Walpersdorf, A., Cotte, N., and Kostoglodov, V. (2012). Slow slip events and strain accumulation in the Guerrero gap, Mexico. *Journal of Geophysical Research: Solid Earth*,117(B4).

Reid, H. F. (1910). The mechanics of the earthquake: the California earthquake of 18 April, 1906, Report of the State Earthquake Investigation Commission, no. 2, Washington: Carnegie Institution, USA.

Reilinger, R., McClusky, S., Vernant, P., Lawrence, S., Ergintav, S., Cakmak, R., ... and Karam, G. (2006). GPS constraints on continental deformation in the Africa-Arabia- Eurasia continental collision zone and implications for the dynamics of plate interactions, *J. Geophys. Res.*, *111*, V05411.

Rosen, P.A., Hensley, S., Joughin, I.R., Li, F.K., Madsen, S.N., Rodriguez, E. and Goldstein, R.M. (2000). Synthetic aperture radar interferometry Proc, *IEEE*, *88*, 333–382.

Rosenau, M., Corbi, F., and Dominguez, S. (2017). Analogue earthquakes and seismic cycles: experimental modelling across timescales. *Solid Earth*, *8(3),* 597-635.

Rousset, B., Jolivet, R., Simons, M., Lasserre, C., Riel, B., Milillo, P., Çakir, Z., and Renard F. (2016). An aseismic slip transient on the North Anatolian Fault, *Geophysical Research Letters, 43(7),* 3254–3262.

Rucker, M. L., Panda, B. B., Meyers, R. A. and Lommler, J. C. (2013). Using InSAR to detect subsidence at brine wells, sinkhole sites, and mines. *Carbonates and Evaporites*, *28(1-2),* 141-147.

Ruiz-Constán, A., Ruiz-Armenteros A.M., Lamas-Fernández, F., Martos-Rosillo, S., Delgado, J.M., Bekaert, D.P.S., Sousa, J.J., Gil, A.J., Caro, C.M., Hanssen. R.F. and Galindo-Zaldívar, J. (2016). Multi-temporal InSAR evidence of ground subsidence induced by groundwater withdrawal: the Montellano aquifer (SW Spain). *Environmental Earth Sciences, 75(3),* 1–16.

Ryder, I., Parsons, B., Wright, T., and Funning, G. (2007). Post-seismic motion following the 1997 Manyi (Tibet) earthquake: InSAR observations and modeling, *Geophysical. J. Int.*, *169*, 1009-1027.

Rykhus, R. P. and Lu, Z. (2008). InSAR detects possible thaw settlement in the Alaskan Arctic Coastal Plain. *Canadian Journal of Remote Sensing*, *34(2),* 100-112.

Sandwell, D., Mellors, R., Tong, X., Wei, M., and Wessel, P. (2011-a). Open radar interferometry software for mapping surface deformation, *Eos Trans. AGU*, *92(28)*, 234

Sandwell, D., Mellors, R., Tong, X., and Wessel, P. (2011-b). GMTSAR: An InSAR processing system based on Generic Mapping Tools, technical report, Scripps Inst. of Oceanogr., Univ. of Calif., San Diego, La Jolla. 12.

Sato, H.P., Abe, K., and Ootaki, O. (2003). GPS-measured land subsidence in Ojiya city, Niigata prefecture, *Japan. Eng. Geol., 67*, 379–390.

Sato, H. P., Abe, K. and Ootaki, O. (2003). GPS-measured land subsidence in Ojiya city, Niigata prefecture, Japan. *Engineering Geology, 67(3-4),* 379-390.

Savage, J., and W. Prescott (1978), Asthenosphere readjustment and the earthquake cycle, *Journal of Geophysical Research: Solid Earth*, *83 (B7),* 3369-3376.

Savage, J.C., and Burford, R.O. (1973). Geodetic determination of relative plate motion in central California, *J. Geophys. Res.*, *78*, 832-845.

Savage, J. C., and Lisowski, M. (1993). Inferred depth of creep on the Hayward fault, central California, *Journal of Geophysical Research, 98*, 787–793.

Savage, J. (1983). A dislocation model of strain accumulation and release at a subduction zone, *J. geophys. Res*, *88 (6),* 4984-4996.

Selim, H. H., and Tüysüz, O. (2013). The Bursa–Gönen Depression, NW Turkey: a complex basin developed on the North Anatolian Fault. *Geological Magazine*, *150(5),* 801-821.

Selim, H. H., Tüysüz, O., Karakaş, A., and Taş, K. Ö. (2013). Morphotectonic evidence from the southern branch of the North Anatolian Fault (NAF) and basins of the south Marmara sub-region, NW Turkey. *Quaternary international*, *292*, 176-192.

Sen S. (1994). Cekmece Golleri Arasındaki Bolgesinin Jeolojisi ve Sedimenter Ozellikleri: Ist. Univ. Fen Bilimleri Enstitusu, Istanbul, 1994, 66p (Unpublished MSc Thesis).

Sen S. (2007). A fault zone cause of large amplification and damage in Avcılar (west of Istanbul) during 1999 Izmit earthquake, Nat. Hazards 2007, 43, 351□363.

Şen, Ş., Koral, H., and Önalan, M. (1996). Sedimentary and tectonic evidence for the relationship between the Istranca Massif, the Paleozoic of Istanbul and overlying Tertiary sequence, 2. In International Symposium on the Petroleum Geology and Petroleum Potential of the Black Sea Area (pp. 22-24), 22–24 September 1996, Sile, Istanbul, Turkey, 237–244.

Serbetci Z. (2018). Examination of Agro-Tourism Potential: Bursa Plain Plain, *Journal of International Social Research*,11(56).

Samieie-Esfahany, S., Hanssen, R., van Thienen-Visser, K. and Muntendam-Bos, A. (2009). On the effect of horizontal deformation on InSAR

subsidence estimates, *In Proceedings of Fringe 2009 Workshop*, Frascati, Italy, 30 November – 4 December 2009, Vol. 30.

Schmidt, D. A., Burgmann, R., Nadeau, R. M., and d'Alessio M. A. (2005). Distribution of aseismic slip-rate on the Hayward fault inferred from seismic and geodetic data, *Journal of Geophysical Research*, *110*, B08406

Schmittbuhl, J., Karabulut, H., Lengliné, O., and Bouchon M. (2016-a). Long-lasting seismic repeaters in the central basin of the main Marmara fault, *Geophysical Research Letters*, *43*, 9527–9534.

Schmittbuhl, J., Karabulut, H., Lengliné, O., and Bouchon, M. (2016-b). Seismicity distribution and locking depth along the Main Marmara Fault, Turkey. *Geochemistry, Geophysics, Geosystems*, 17(3), 954-965.

Solari, L., Ciampalini, A., Raspini, F., Bianchini, S., and Moretti, S. (2016). PSInSAR analysis in the Pisa Urban Area (Italy): a case study of subsidence related to stratigraphical factors and urbanization. *Remote Sensing*, *8(2),* 120.

Straub, C., H.-G. Kahle, and C. Schindler (1997), GPS and geologic estimates of the tectonic activity in the Marmara Sea region, NW Anatolia, *Journal of Geophysical Research: Solid Earth (1978-2012), 102 (B12),* 27,587-27,601.

Stein, R. S., Barka, A., and Dieterich, J. H. (1997). Progressive failure on the North Anatolian fault since 1939 by earthquake stress triggering, *Geophysical Journal International*, *128*, 594–604.

Steinbrugge, K.V., Zacher, E.G., Tocher, D., Whitten, C.A., and Clair, C.N. (1960). Creep on the San Andreas fault, *Bulletin of the Seismological Society of America*, *50*, 396 – 404.

Sudhaus, H., and Jónsson, S. (2011). Source model for the 1997 Zirkuh earthquake (MW=7.2) in Iran derived from JERS and ERS InSAR observations, *Geophysical. J. Int.*, *185*, 676-692.

Taylor, C.J., and Alley, W.M. (2002). Ground-Water-Level Monitoring and the Importance of Long-Term Water-Level Data (No. 1217-2002); US Geological Survey: Reston, VA, USA, 2002.

Temtime, T., Biggs, J., Lewi, E., Hamling, I., Wright, T., and Ayele, A. (2018) Spatial and temporal patterns of deformation at the Tendaho geothermal prospect, Ethiopia. *Journal of Volcanology and Geothermal Research*, 357, 56-67.

Tezcan, S.S., Kaya, E., Bal, E., and Ozdemir, Z. (2002). Seismic amplification at Avcilar, Istanbul, Eng. Struct., 2002, 24, 661–667.

Thatcher, W. (1979). Systematic inversion of geodetic data in central California, *Journal of Geophysical Research*, *84*, 2283–2297.

Thatcher, W. (2009). How the continents deform: The evidence from tectonic geodesy. *Annual Review of Earth and Planetary Sciences*, *37*, 237-262.

Thomas, M.Y., Avouac, J.P., Champenois, J., Lee, J.C., and Kuo, L.C. (2014). Spatio-temporal evolution of seismic and aseismic slip on the Longitudinal Valley Fault, Taiwan, *Journal of Geophysical Research: Solid Earth*, 119.

TMMOB, Hurriyet Daily News, Retrieved on 28 November 2017 from http://www.hurriyetdailynews.com/six-square-kilometers-of-istanbuls-land-reclaimed-from-the-sea-117884.

Tomás, R., Herrera, G., Delgado, J., Lopez-Sanchez, J.M., Mallorqui, J.J., and Mulas, J. A. (2009). Ground subsidence study based on DInSAR data: Calibration of soil parameters and subsidence prediction in Murcia City (Spain). *Eng. Geol.*, *111*, 19–30.

Tomás, R., Herrera, G., Cooksley, G., and Mulas, J. (2011). Persistent scatterer interferometry subsidence data exploitation using spatial tools: The vega media of the Segura river basin case study. *J. Hydrol., 400*, 411–428.

Törnqvist, T. E., Wallace, D. J., Storms, J. E., Wallinga, J., Van Dam, R. L., Blaauw, M., Derksen, M.S., Cornelis, J.W, K., Meijneken C., and Snijders, E. M. (2008). Mississippi Delta subsidence primarily caused by compaction of Holocene strata. *Nature Geoscience*, *1(3),* 173.

Trubienko, O., Fleitout, L., Garaud, J. D., and Vigny, C. (2013). Interpretation of interseismic deformations and the seismic cycle associated with large subduction earthquakes. *Tectonophysics*, 89, 126-141.

Turkish Statistical Institute, TUIK. Retrieved on 26 November 2018 from http://www.tuik.gov.tr/HbGetirHTML.do?id=27587.

Osmanoglu, B., Dixon, T.H., Wdowinski, S., Cabral-Cano, E. and Jiang, Y. (2011). Mexico city subsidence observed with persistent scatterer InSAR, *Int. J. Appl. Earth Observ. Geoinform., 13*, 1–12,

Ozalaybey, O., Ergin, M., Aktar, M., Tapirdamaz, C., Bicmen F., and Yoruk, A. (2002). The 1999 Izmit Earthquake Sequence in Turkey: Seismological and Tectonic Aspects, *Bulletin of the Seismological Society of America*, *92*, 1, 337-386.

Van Asselen, S. (2011). The contribution of peat compaction to total basin subsidence: Implications for the provision of accomodation space in organic-rich deltas. *Basin Res.*, *23*, 239–255.

Van Leeuwen, K., and Sjerps R., (2016). Istanbul: the challenges of integrated water resources management in Europe's megacity. *Environ Dev. Sustain.*, *18*, 1-17.

Walter, T.R., Manzo, M., Manconi, A., Solaro, G., Lanari, R., Motagh, M., Woith, H., Parolai, S., Shirazei, M., Zschau, J., Baris, S., and Ansal, A. (2010). Satellite monitoring of hazards: A focus on Istanbul, Turkey. *Eos, Trans. Am. Geophys. Union, 91*, 313–324.

Wang, L., Wang, R., Roth, F., Enescu, B., Hainzl, S., and Ergintav, S. (2009-a). Afterslip and viscoelastic relaxation following the 1999 M7.4 Izmit earthquake from GPS measurements, *Geophysical Journal International*, *178*, 1220–1237.

Wang, H., Wright, T.J., and Biggs, J. (2009-b). Interseismic slip rate of the northwestern Xianshuihe fault from InSAR data, *Geophys. Res. Lett.*, *36*, L03302.

Wang, X.Y., Sun, L., and Liu, C.L. (2013). Present situation of land subsidence and its mechanism in China. Global View of Engineering Geology and the Environment. *In Proceedings of the International Symposium and 9th Asian Regional Conference of IAEG (AREG2013)*, Beijing, China, 24–25 September 2013, 475–480.

Weertman, J., and J. R. Weertman (1964), Elementary Dislocation Theory, Macmillan, NewYork.

Wei, M., Sandwell, D., and Fialko, Y. (2009). A silent M4.8 event of October 3-6, 2006, on the Superstition Hills Fault, Southern California, *Journal of Geophysical Research, 114*, B07402.

Wessel, P., Smith, W. H., Scharroo, R., Luis, J., and Wobbe, F. (2013). Generic Mapping Tools: Improved version released, *EOS Trans. AGU*, *94*, 409-410.

Wikipedia, The Free Encyclopedia, Bursa, The view of Bursa Plain from the hills of Mount Uludag, Available Online, Retrieved on 26 November 2018, from https://tr.wikipedia.org/wiki/Bursa.

Wright, P., and Stow, R. (1999). Detecting mining subsidence from space. *Int. J. Remote Sens.*, *20*, 1183–1188.

Wright, T. (2002). Remote monitoring of the earthquake cycle using satellite radar interferometry, Philosophical transactions of the Royal Society of London, Series A: *Mathematical Physical and Engineering Sciences*, *360*, 2873-2888.

Wright, T. J., Parsons, B. E., and Zhoung L. (2004). Toward mapping surface deformation in three dimensions using InSAR, *Geophys. Res. Lett., 31*, L01607.

Xu, B., Feng, G., Li, Z., Wang, Q., Wang, C., and Xie, R. (2016). Coastal subsidence monitoring associated with land reclamation using the point target based SBAS-INSAR method: A case study of Shenzhen, China., *Remote Sensing, 8(8),* p.652,

Zebker, H. A. (1986). Goldstein, R. M. Topographic mapping from interferometric synthetic aperture radar observations. *Journal of Geophysical Research: Solid Earth*, *91(B5),* 4993-4999.

Zebker H.A., Rosen P.A., Goldstein R.M., Gabriel A., and Werner C.L. (1994). On the derivation of coseismic displacement fields using differential radar interferometry—the Landers earthquake. *J. Geophys. Res. 99,* 19617–34.

Zeitoun, D. G., and Wakshal, E. (2013). The Subsidence Phenomenon Throughout the World in Land subsidence analysis in urban areas: the Bangkok

metropolitan area case study; Springer Science & Business Media, London, England, 9-23

Zhang, K., Ge, L., Li, X., and Ng, A.M. (2013). Monitoring ground surface deformation over the North China Plain using coherent ALOS PALSAR differential Interferograms, *J. Geod.*, *87*, 253–265.

APPENDICES

- **APPENDIX A:** Supplementary documents of GPS horizontal vel. (Chapter 4.2).

- **APPENDIX B:** Supplementary documents of atmospheric phase removal (Chapter 4).

- **APPENDIX C:** Supplementary materials of uncertainties on horizontal and vertical velocities obtained from InSAR data inversion (Chapter 4.4.2).

- **APPENDIX D:** Supplementary materials of the probability distributions obtained from Monte Carlo Markov Chain exploration of the model parameters (Chapter 4.5).

APPENDIX A: Components of GPS horizontal velocities.

Table A1 : Components of horizontal velocities (V_E, V_N) relative to the Eurasian fixed reference frame for the period 2014-2016, one-sigma uncertainties (σ_{-E}, σ_{-N}) and correlation coefficient (ρ_{-EN}). The flag in the second column 'F' distinguishes survey (s) and continuous (c) sites.

SITE	F	Longitude (deg.E)	Latitude (deg.N)	V_E	V_N	σ_{-E}	σ_{-N}	ρ_{-EN}
				mm/yr				
KR30	s	30.43646	40.69154	-13.41	-2.12	1.38	1.68	-0.040
KR29	s	30.40741	40.70456	-12.01	2.10	2.01	2.45	-0.015
KR25	s	30.39755	40.71614	-5.73	-10.99	2.16	2.96	0.006
KR22	s	30.38343	40.79281	-4.11	-4.72	1.40	1.70	-0.013
KR26	s	30.36171	40.70220	-12.52	-0.03	1.91	2.29	-0.005
KR23	s	30.36040	40.72286	-10.99	-2.90	2.18	2.15	0.021
KR31	s	30.36036	40.67031	-13.48	-0.49	1.49	1.83	0.004
KR28	s	30.35320	40.69616	-12.77	0.99	1.46	1.76	-0.000
KR24	s	30.32734	40.71603	-12.28	-0.89	1.72	2.09	0.000
KR32	s	30.32520	40.61163	-18.16	-5.41	2.05	2.18	-0.069
KR27	s	30.32509	40.69855	-11.38	-9.30	1.82	2.66	0.013
SMAS	s	30.13402	40.68972	-15.36	-2.40	2.49	3.42	-0.003
SISL	s	30.13027	40.74533	-8.85	-2.85	1.53	1.89	-0.028
KR11	s	30.04048	40.78280	-6.04	-6.06	2.39	2.94	0.059
KR16	s	29.99286	40.70874	-14.30	-1.07	1.50	1.81	-0.032
KR12	s	29.98820	40.73070	-5.63	-2.40	1.74	2.13	-0.018
KR19	s	29.98775	40.62831	-16.79	-6.68	1.82	2.79	-0.042
KR18	s	29.96542	40.67467	-13.97	1.24	1.29	1.50	-0.082
IZMT	c	29.95093	40.80198	-5.19	-0.93	0.73	0.76	-0.020
KR14	s	29.94658	40.72038	-15.64	-2.46	2.59	3.05	0.078
KR13	s	29.93895	40.72426	-4.10	-2.12	1.99	2.24	-0.014
KR10	s	29.93512	40.80328	-7.94	-2.03	2.28	2.13	-0.029
KR15	s	29.93050	40.70578	-15.90	0.18	2.02	2.74	-0.052
KR09	s	29.81917	40.67286	-15.42	-1.12	1.65	1.71	-0.011
KR08	s	29.80409	40.70503	-8.53	-3.90	1.74	2.05	-0.134
KR07	s	29.80093	40.71685	-13.08	-1.14	1.47	1.82	0.005
KR03	s	29.79821	40.72727	-8.73	-2.05	1.34	1.65	-0.022
KR01	s	29.79660	40.78389	-5.41	-1.18	1.63	1.98	0.004
KR06	s	29.79564	40.72295	-11.36	-2.24	2.68	2.94	0.062
KR04	s	29.79505	40.72645	-6.96	-0.56	1.72	2.09	-0.015
KR02	s	29.79466	40.74347	-7.41	-6.60	1.27	1.51	-0.036
KR05	s	29.79145	40.72215	-8.21	-2.56	1.80	2.20	-0.073
TUBI	s	29.45068	40.78672	-4.47	-1.42	0.68	0.72	-0.023

APPENDIX B: Supplementary documents of atmospheric phase removal.
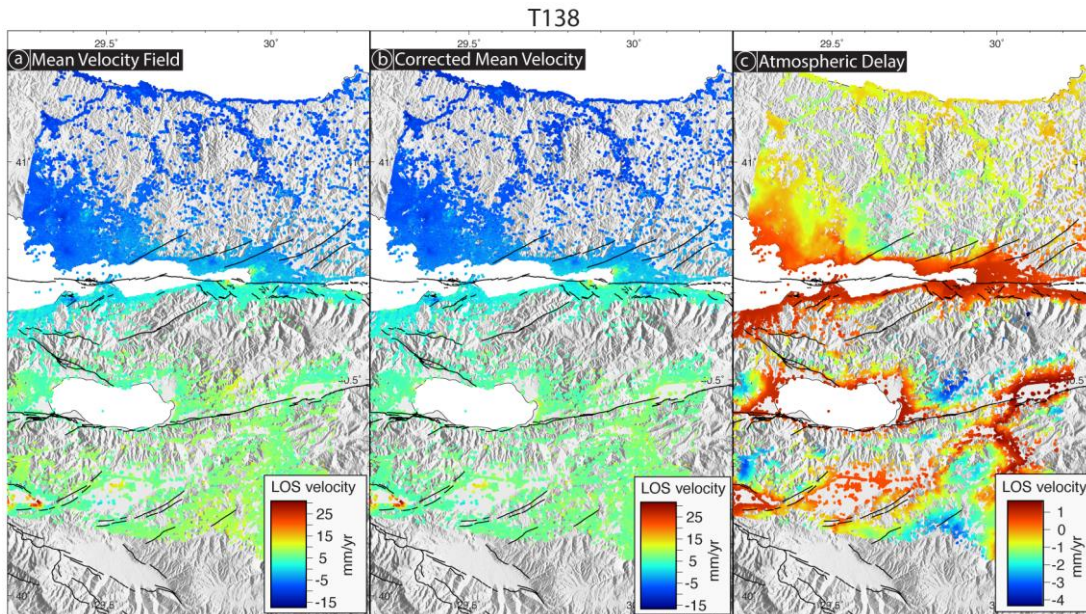
APPENDIX B1:

Figure B.1 : InSAR observations and atmospheric corrections. (**a**) Mean velocity field from Sentinel 1 A/B descending track T138, (**b**) corrected mean velocity using ERA-Interim model, (**c**) atmospheric delay map predicted from the ERA Interim model.
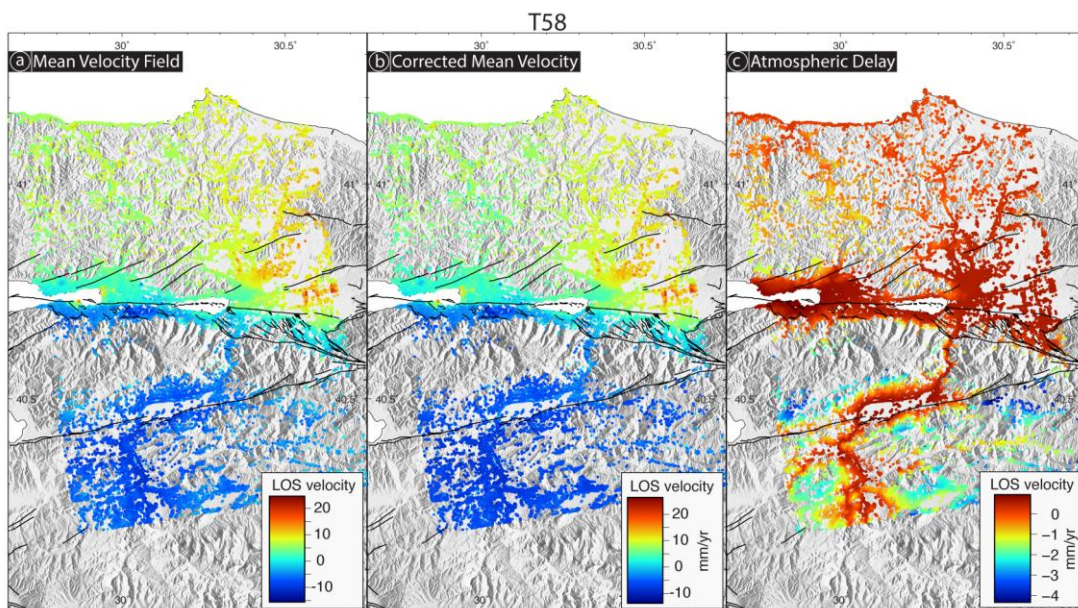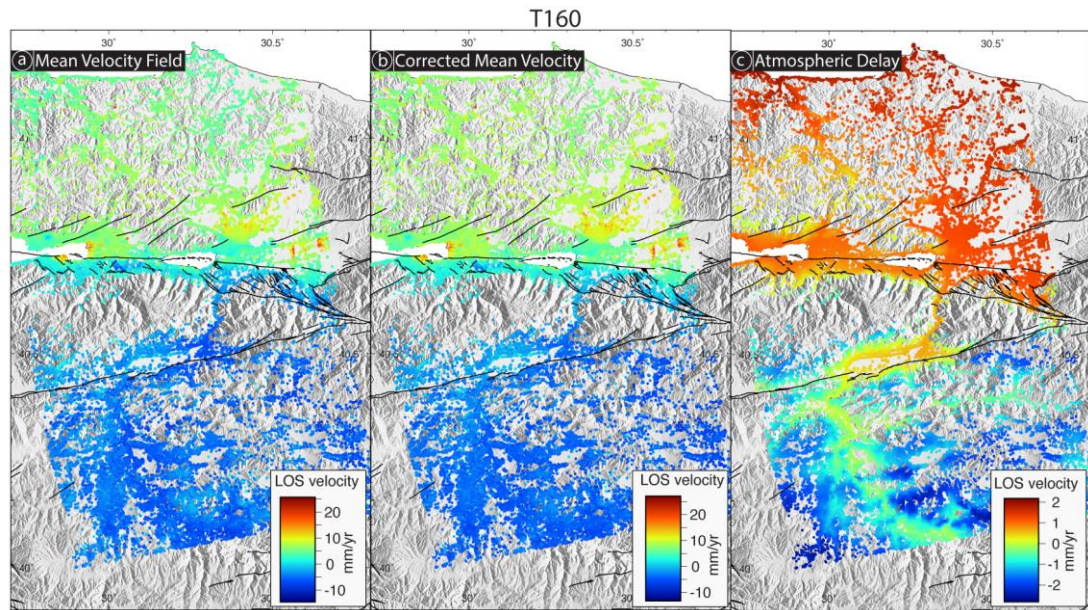
APPENDIX B2:

Figure B.2 : InSAR observations and atmospheric corrections. (**a**) Mean velocity field from Sentinel 1 A/B ascending track T58, (**b**) corrected mean velocity using ERA-Interim model, (**c**) atmospheric delay map predicted from the ERA Interim model.

Figure B.3 : InSAR observations and atmospheric corrections. (**a**) Mean velocity field from Sentinel 1 A/B ascending track T160, (**b**) corrected mean velocity using ERA-Interim model, (**c**) atmospheric delay map predicted from the ERA Interim model.
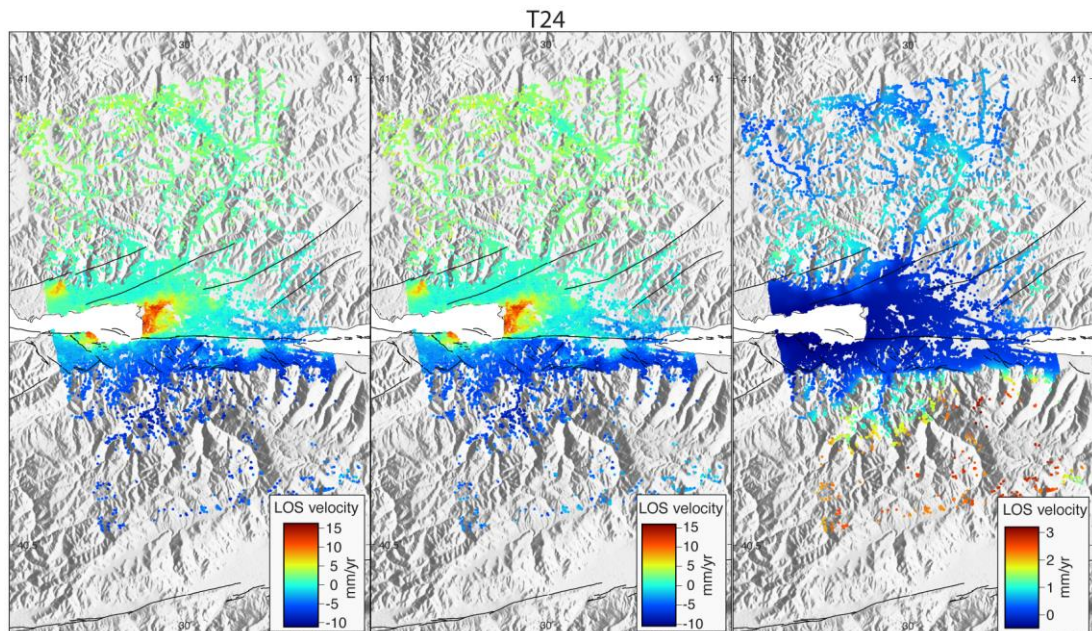
APPENDIX B4:

Figure B.4 : InSAR observations and atmospheric corrections. (**a**) Mean velocity field from TerraSAR-X ascending track T24, (**b**) corrected mean velocity using ERA-Interim model, (**c**) atmospheric delay map predicted from the ERA Interim model.
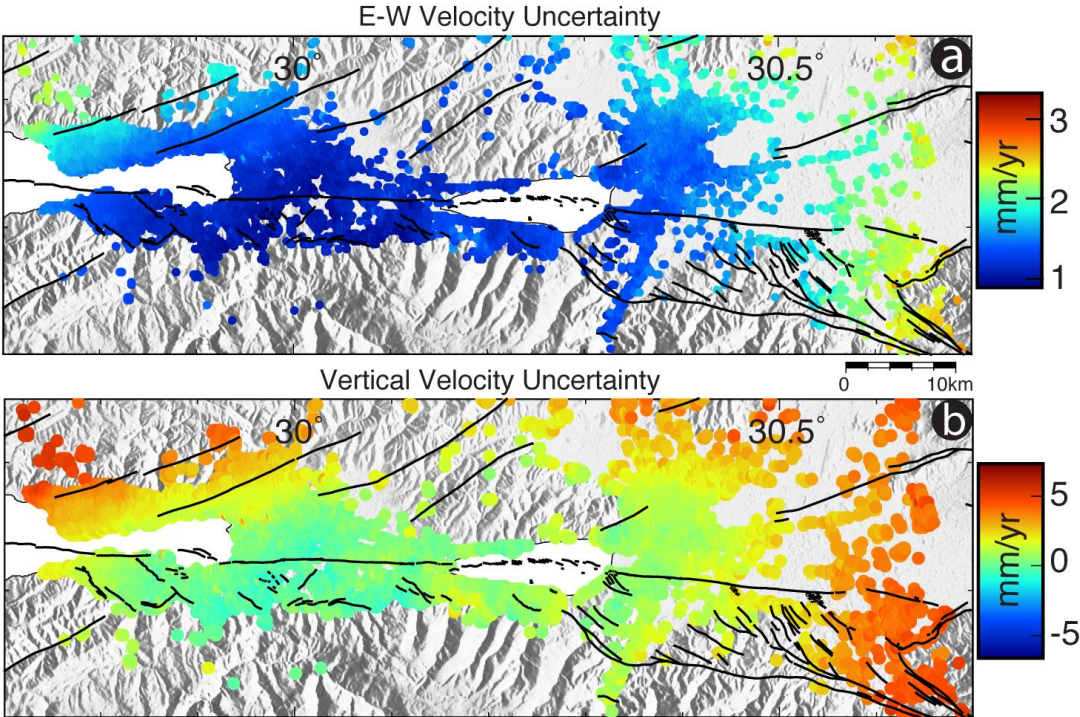
APPENDIX C1:

Figure B.5 : Uncertainties on horizontal (**a**) and vertical (**b**) velocities obtained from InSAR data inversion, following Wright et al. (2004) procedure.
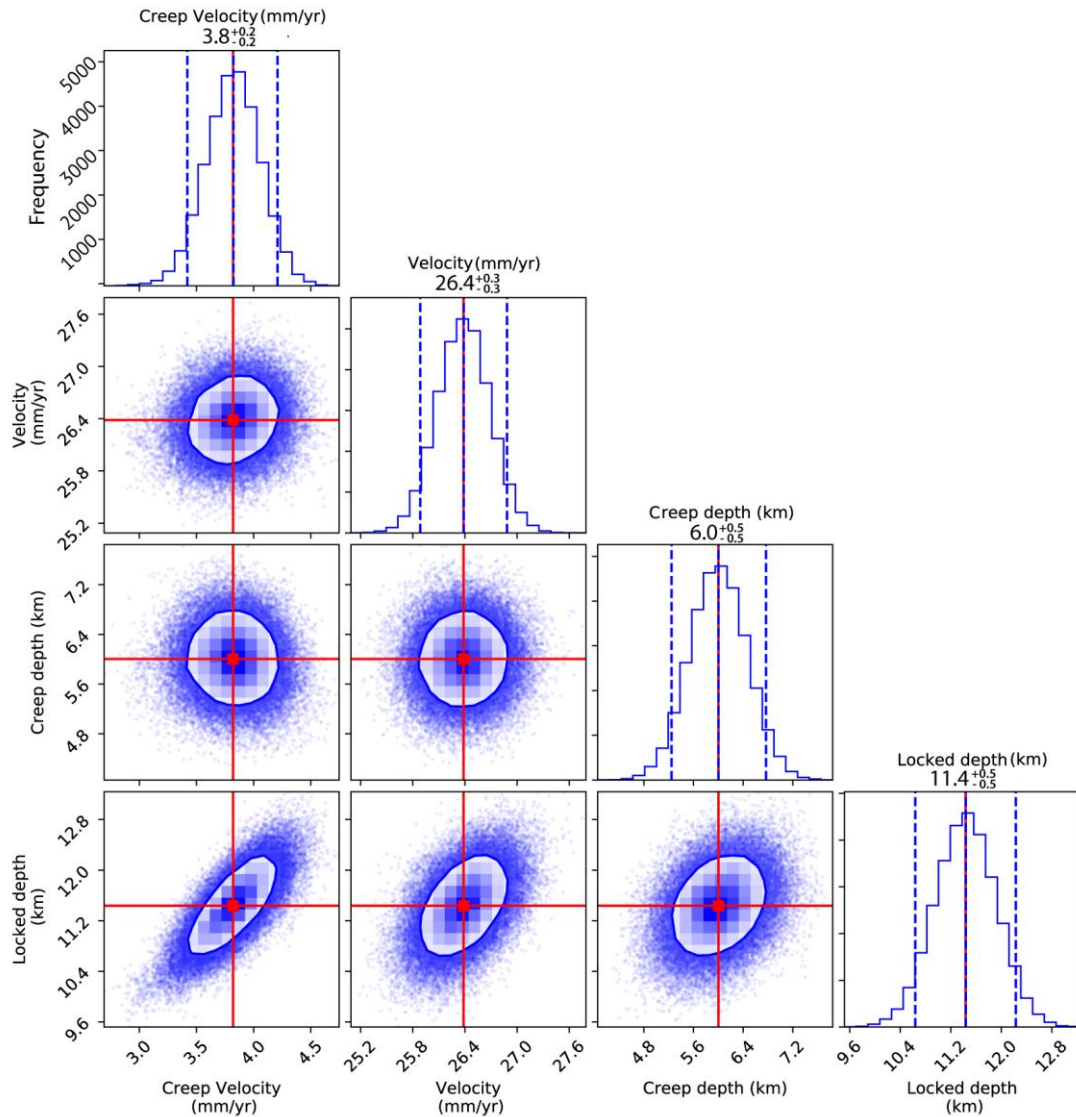
APPENDIX D1:

Figure D.1 : One-dimensional and two-dimensional sampled probability distributions obtained from Monte Carlo Markov Chain exploration of the model parameters assuming a priori uniform distribution for all model parameters but locking depth D_1 (Gaussian distribution), for profile A-A'. The diagonal plots display the one-dimensional marginal distribution for each parameter independently in the histograms. The panels with clouds of points display the marginal two-dimensional distributions. The red solid lines indicate the mean value for each model parameter. Blue dashed lines mark the 95% confidence interval of the probability density functions. The values above each histogram indicate the mean value.
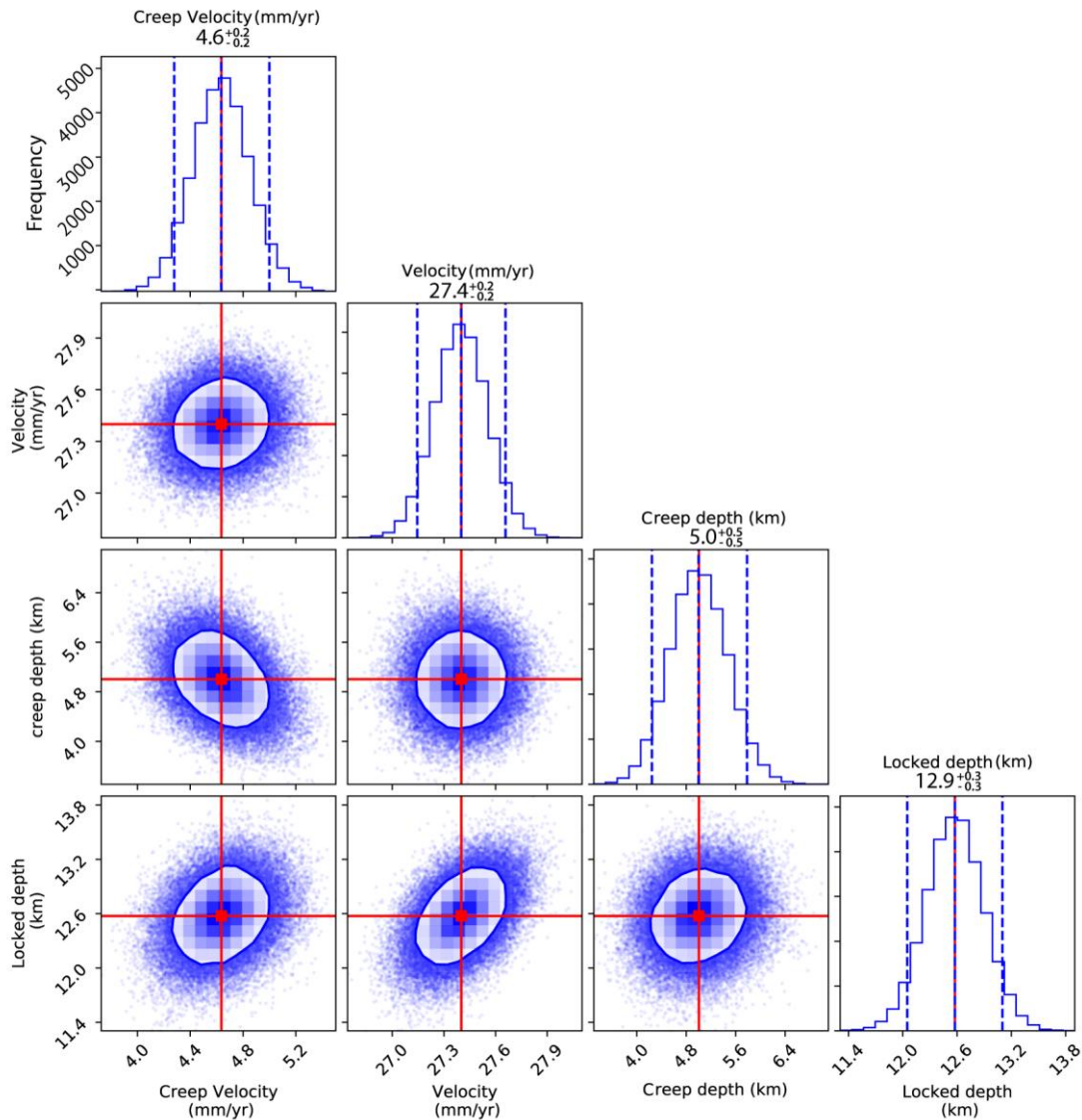
Figure D.2 : One-dimensional and two-dimensional sampled probability distributions obtained from Monte Carlo Markov Chain exploration of the model parameters assuming a priori uniform distribution for all model parameters but locking depth D_1 (Gaussian distribution), for profile C-C'. The diagonal plots display the one-dimensional marginal distribution for each parameter independently in the histograms. The panels with clouds of points display the marginal two-dimensional distributions. The red solid lines indicate the mean value for each model parameter. Blue dashed lines mark the 95% confidence interval of the probability density functions. The values above each histogram indicate the mean value.
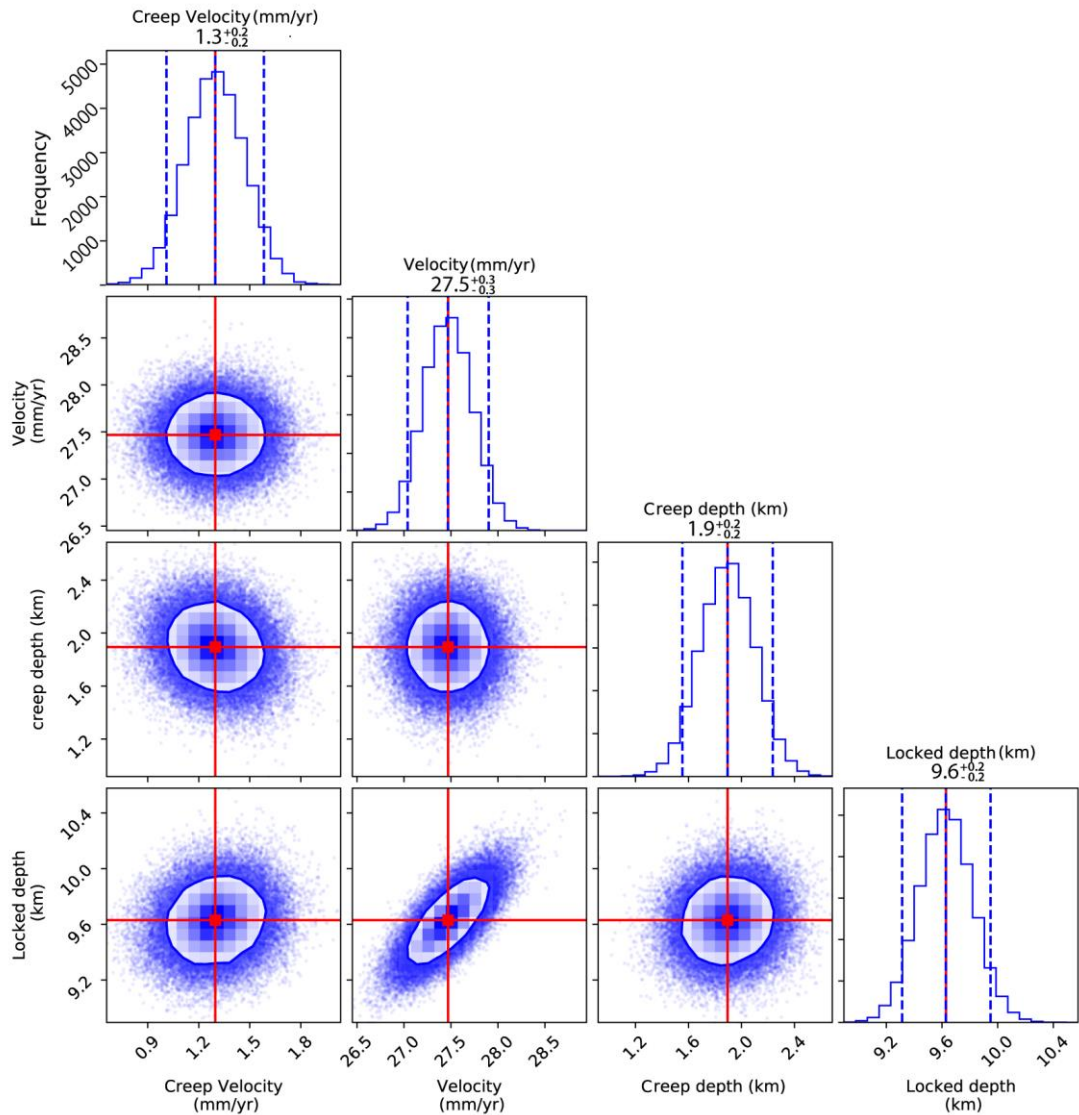
Figure D.4 : One-dimensional and two-dimensional sampled probability distributions obtained from Monte Carlo Markov Chain exploration of the model parameters assuming a priori uniform distribution for all model parameters but locking depth D_1 (Gaussian distribution), for profile D-D'. The diagonal plots display the one-dimensional marginal distribution for each parameter independently in the histograms. The panels with clouds of points display the marginal two-dimensional distributions. The red solid lines indicate the mean value for each model parameter. Blue dashed lines mark the 95% confidence interval of the probability density functions. The values above each histogram indicate the mean value.

CURRICULUM VITAE

Name Surname	**: Gökhan ASLAN**
Place and Date of Birth	**: TARSUS, 28/02/1988**
E-Mail	**: gokhan.aslan@univ-grenoble-alpes.fr**
	gokhanaslan3@gmail.com

EDUCATION:

- **B.Sc.** : 2010, Erciyes University, Faculty of Engineering, Department of Civil engineering
- **M.Sc.** : 2012, Istanbul Technical University, Earthquake Engineering and Disaster Management institute, Earthquake Engineering Program
- **Ph.D.** : 2019, Istanbul Technical University, Eurasia Institute of Earth Sciences, PhD in Geodynamics

    : 2019, Université Grenoble-Alpes, Institut des Sciences de la Terre (ISTerre), Grenoble, France, PhD in Seismic cycle and transient deformations (Cotutelle with Istanbul Technical University)

PROFESSIONAL EXPERIENCE AND REWARDS:

- *September 2011 – January 2013*: Research Assistant, Bulent Ecevit University, Department of Mining Engineering,
- *January 2013 – December 2013:* Engineer, Temelsu – Mott MacDonald, Uzbekistan
- *January 2016 – December 2016:* TUBITAK project 113Y102
- *January 2017 – May 2017: "Bourses de doctorat en co-tutelle"* provided by the French Embassy
- *June 2017 – December 2017:* CMIRA scholarship program provided by the Rhone-Alpes Region
- *January 2018 – May 2018: "Bourses de doctorat en co-tutelle"* provided by the French Embassy
- *May 2017 – December 2017: Norwegian Research Council, project HADES, grant no: 250661*
- *May 2017 – December 2017: University Grenoble Alpes IDEX project scholarship program*

- *January 2019 – May 2019: "Bourses de doctorat en co-tutelle"* provided by the French Embassy

PUBLICATIONS, PRESENTATIONS AND PATENTS ON THE THESIS:

Aslan, G., Cakır, Z., Ergintav, S., Lasserre, C., and Renard, F. (2018). Analysis of Secular Ground Motions in Istanbul from a Long-Term InSAR Time-Series (1992–2017). *Remote Sensing*, *10*, 408.

Aslan, G., Cakir, Z., Lasserre, C., and Renard, F. (2019). Investigating Subsidence in the Bursa Plain, Turkey, Using Ascending and Descending Sentinel-1 Satellite Data, *Remote Sensing*, *11*, 85.

Aslan G, Lasserre C, Cakir Z, Ergintav S., Cetin S., Dogan U., Bilham R., and Renard F. (2019). Shallow creep along the 1999 Izmit earthquake's rupture (Turkey) from high temporal resolution interferometric synthetic-aperture radar data (2011-2017). *Journal of Geophysical Research, Solid Earth*,